2011-9

Novel Approaches to the Analysis of Localised Stress Concentrations in Deformed Elastomers

John McNamara
Technological University Dublin

Novel Approaches to the Analysis of Localised Stress Concentrations in Deformed Elastomers

John Mc Namara

PhD

Supervisors: Dr. Steve Jerrams

Dr. Thomas Alshuth

School of Manufacturing and Design Engineering

Dublin Institute of Technology

September 2011

Abstract

The research described here is concerned with improving finite element analysis (FEA) of rubber components subjected to dynamic loading, particularly in respect of accurate modelling of stress softening using standard software codes and phenomenological material models. The research required the design and implementation of a user subroutine capable of inclusion in standard highly nonlinear codes. Experimental methods were employed to corroborate the FEA simulations and so validate the subroutine. This was also achieved using 3D image correlation photogrammetry (ICP) and other novel experimental procedures. From this experimentation and modelling, the results for different rubber specimens and load cases were presented.

The primary aim of the research was to provide a novel method for modelling stress softening for localised stress concentration at discontinuities in rubber components and to implement optimised stress softening subroutines for rubber into commercial software codes. As a consequence other novel research is presented in respect of:

i) A semi empirical formula for elastomer stress softening.

ii) Recommendations for improving ICP techniques applied to rubber.

iii) A determination of the likelihood of large flaws causing premature failures in rubber specimens.

Keywords: stress softening, elastomer, fatigue, stress concentration.

I certify that this thesis which I now submit for examination for the award of PhD, is entirely my own work and has not been taken from the work of others save and to the extent that such work has been cited and acknowledged within the text of my work.

This thesis was prepared according to the regulations for postgraduate study by research of the Dublin Institute of Technology and has not been submitted in whole or in part for an award in any other Institute or University.

The Institute has permission to keep, to lend or to copy this thesis in whole or in part, on condition that any such use of the material of the thesis be duly acknowledged.

Signature_____Date_____

Candidate

Acknowledgements

A large number of people have assisted and supported me throughout this research to who I am grateful. First and foremost, I would like to express my sincere gratitude to my supervisor Dr Steve Jerrams, who I am deeply indebted to, not only for his initial confidence in my engineering ability, but for his guidance, supervision and patience over the years. I'd like to extend my gratitude to Prof. Robert Schuster, for giving me the opportunity to work in DIK; it was a privilege and an invaluable learning experience. I also offer sincere thanks to Dr Thomas Alshuth for his introduction to the world of elastomers, and his dedication to the progression of research in the field. I would also like to thank John Lawlor and the School of Manufacturing and Design Engineering at DIT.

I would like to thank all my friends and colleagues both at DIT and DIK, who helped along the way. In particular, I must thank Dr Frank Abraham, whose groundbreaking work I have had the opportunity to build upon and Peter Erren, for his technical assistance and friendship, along with Dr Stephen Ronan, Dr Jens Meier and Felipe Hüls for their creative ideas on FEA. Finally, it gives me great pleasure to thank my parents, family and friends; without their encouragement and support this dissertation would not have reached completion. Above all, I wish to express my eternal gratitude to my wife, Katriona, for sticking with me through all the good times and bad and for her patient love and support.

Abbreviations

3D	Three Dimensional
ACM	Acrylic Rubber
ASTM	American Standard for Testing of Materials
BS	British Standards
CCD	Charged Couple Device
CL	Chemiluminescence
CT	Computed Tomography
DIK	Deutsches Institut für Kautschuktechnologie
DIN	Deutsches Institut für Normung
DMA	Dynamic Mechanical Analysis
DTMA	Dynamic Thermal Mechanical Analysis
EPDM	Ethylene-Propylene-Diene Polymer
FE	Finite Element
FEA	Finite Element Analysis
ICP	Image Correlation Photogrammetry
ISO	International Organization for Standardization
JASO	Japanese Automotive Standards Organisation
MTS	Material Testing System
NBR	Acrylonitrile-Butadiene Rubber
NR	Natural Rubber
RBE2	Rigid Body Element Type 2
RSA	Rheometrics Solids Analyser
SAE	Society of Automotive Engineers
SEN	Single Edge Notched
SLS	Standard Linear Solid
TEM	Transmission Electron Microscope
UV	Ultraviolet
WLF	Williams-Landel-Ferry
XLD	Crosslink Density

Nomenclature

C_{ij}	Mooney-Rivlin Coefficient
E	Young's modulus
E’	Elastic Storage modulus
E’’	Elastic Loss modulus
E*	Elastic Complex modulus
G’	Dynamic storage modulus in shear
G’’	Dynamic loss modulus in shear
I_1	1^{st} Strain Invariant
I_2	2^{nd} Strain Invariant
Tan δ	Loss factor
ε	Strain
σ	Stress
τ	Relaxation time
η	Viscosity
F	Force
K_{tu}	Notch sensitivity factor
$K_{t\theta}$	Notch sensitivity angle
phr	Parts per hundred rubber
t_{90}	90% of time to complete curing
T_g	Glass transition temperature
λ	stretch or strain ratio
W	Strain energy density

Table of Contents

List of Figures

List of Tables

Chapter 1 Introduction

1.1 Motivation for the Research

The establishment of professional organisations and standards bodies, such as the Japanese Automotive Standards Organisation (JASO) and the Society of Automotive Engineers (SAE) in the USA, led to an improved exchange of ideas and policy, resulting in the development of minimum standards for almost all aspects of the design and manufacture of powered vehicles (e.g. cars, heavy goods vehicles, trains and aircraft). With the development of these standards, greater performance, reliability and durability have become expected from the components that comprise the vehicles. Even so, the design and manufacture of elastomeric components remains a major challenge to design engineers. The complexities of designing elastomeric components and sometimes the limitations of nonlinear finite element analysis (FEA) packages can often lead to components being over engineered or inadequate for the operations they are required to fulfil. Firstly, this means that components sizes, weights and costs are greater than is necessary. This also means that expenditure on energy during manufacture is higher than required and when the parts finally fail or reach the end of their service lives, larger quantities of rubber need to be recycled, incinerated or invariably dumped into the environment. Secondly, premature failure of rubber parts in vehicles and machines can compromise safety and performance or at least lead to costly repair or overhaul.

A greater understanding of the deformation of elastomers at stress concentrations will lead to improved FEA modelling and consequently improved component design and hence safer more reliable vehicles with a need for less rubber material

to be replaced and discarded, creating obvious benefits to the environment and the economies of manufacturing nations.

The inevitable change in the properties of rubber with time is rarely modelled by FEA software and when it is, this modelling in invariably incorrect. Viscoelastic (time dependent) phenomena in rubber-like materials are modelled inaccurately for the following reasons:

i). Once loaded and with each successive load, a rubber component will have variable properties throughout its structure dependent on the local levels of repeated loading and service conditions.

ii). Viscoelastic phenomena can be both physically and chemically activated and the effect on physical properties can be either additive or counteracting.

iii). The phenomena will be influenced not only by the magnitude of the load application but also by:

a) frequency, b) rate and c) load case.

The research described here attempts to improve FEA of rubber components subjected to dynamic loading and particularly to accurately model stress softening. The improvement was to be achieved using standard software codes and phenomenological material models. Hence an aspect of the research required the design and implementation of a user subroutine capable of inclusion in standard highly nonlinear codes to allow accurate simulation of stress softening effects for rubber components or test specimens. Experimental methods were to be employed to corroborate the FEA simulations and so validate the subroutine allowing its implementation. It was further proposed to use 3D image

correlation photogrammetry (ICP), employing the commercially available system ARAMIS **[1]**, in conjunction with physical testing.

The dissertation goes on to describe other novel experimental procedures to conduct measurements of localised deformations and strains using the ICP system for specimens of different geometries. A comparison of experimental values derived from ICP and those from FEA was required to validate the FEA simulation of stress softening effects, prior to presenting the results for different rubber specimens and load cases.

1.2 Dynamic Properties at Discontinuities

1.2.1 The Influence of Discontinuities on Fatigue Life

Some novel research has been carried out on the influence of "flaw size" on the initiation of cracks and of crack growth and the resultant influence on fatigue life in elastomeric specimens **[2]**. Outcomes showed that failure can occur not only from edge flaws but also from heterogeneities resulting from the material constituents and the manufacturing process. Independent of the flaw shapes, the rubber compound used, its condition (either in the glassy or rubbery phase) or even in the case of ozone cracking etc, it was previously asserted that flaws that grow to cause failure usually emanate from a critical original size of 40 ± 20 μm. **[3]**. The research presented here includes a consideration of the presence of larger flaws that were previously unobserved and are shown to be the sources of failures in cyclic loading of rubber components.

1.3 Aim and Objectives

The primary aim of the research was to provide a novel method for modelling stress softening for localised stress concentrations at discontinuities in rubber components. This method would need to be robust and capable of use in industry. This aim gave rise to the following objectives:

- To understand and model localised stress-strain in rubber at stress raisers under static and dynamic load.
- To develop tools that precisely measure localised strains resulting from known general strain states in elastomeric test-pieces and rubber components.
- To investigate the relationship between flaw size of cracks, holes, inclusions and other discontinuities and local stress and strain in the vicinity of discontinuities.
- To introduce and refine methods of including stress softening in FEA simulations using standard software and material models to allow analysis of rubber components in real world conditions.
- To create FEA simulations of local stresses, strains and energies for elastomers that stress soften markedly and those that do not.
- To verify material models by comparing finite element simulations with actual physical behaviour recorded by 3D optical measurements.
- To implement optimised stress softening subroutines for rubber into commercial software codes.

1.3.1 Secondary Aims

Two secondary aims were also prompted by the research. The following issues required addressing:

i) It was determined that an investigation into heat-build up in cycled specimens was required to ensure that excessive temperature rise did not adversely affect changes in specimen structure and physical properties. Changes in properties attributable to chemical influence need to be understood (see Section 3.5).

ii) A simple equation for describing stress softening in un-notched dumbbell samples would be offered to allow ready comparison of tests for different compounds and load amplitudes (see Section 3.6).

An example of an elastomeric component in everyday use, a drive shaft boot, is illustrated in Figure 1.1. It gives an indication of the various complex loading modes (i.e. compression, torsion, tension) that the component is subjected to repeatedly and at high frequencies in general service. Also it should be recognised that as the flanks of the boot contact one another, rubber to rubber friction will occur.

It is evident that for a component like the drive shaft boot, experiencing non uniform, cyclic, complex loading, made from a material having properties that continually change with this loading, standard hyperelastic FEA is inadequate.

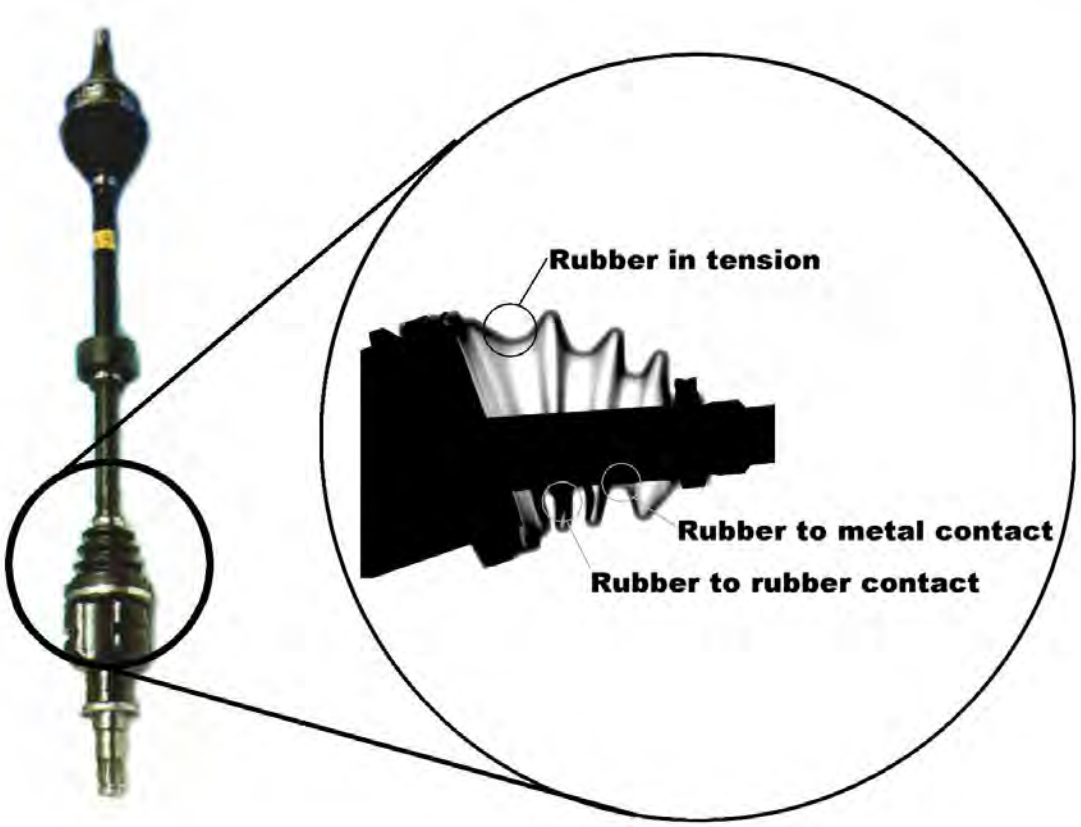

Figure 1.1: An X-ray image of a deformed rubber drive shaft boot

1.4 Dissertation Structure

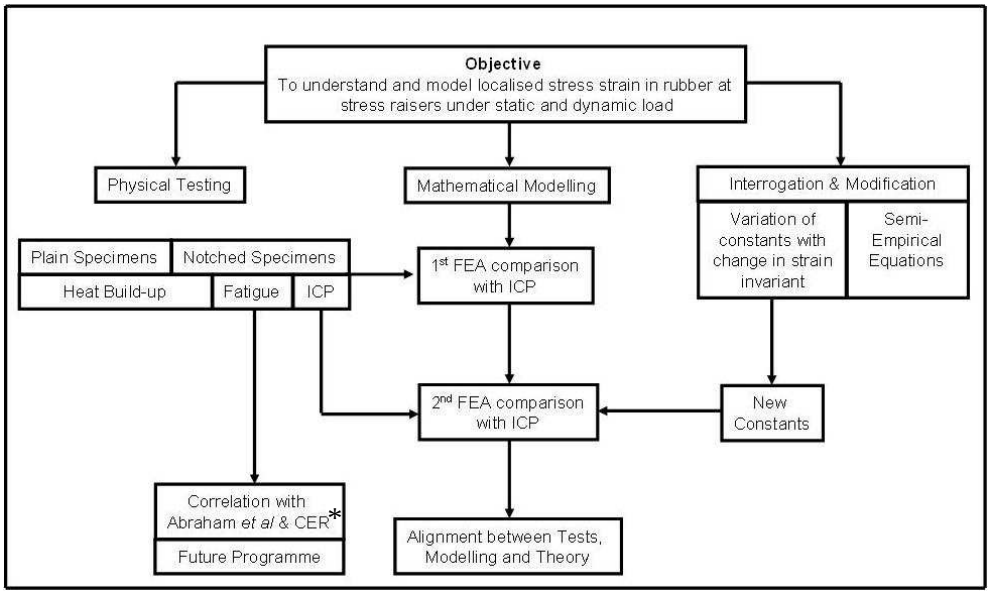

Figure 1.2: Overview of testing and analysis carried out to achieve the research objectives *[25]

Figure 1.2 shows schematically the physical testing, analysis and simulation necessary to realise the primary aim of the research.

1.5 The Dissertation Structure

Chapter One opened with an overview of the motivation for the research and the challenges that face mechanical and design engineers when working with elastomers and rubber like materials for use in engineering applications it goes on to state an aims and objectives. Chapter Two is the literature review, where the basic physical properties of rubber are outlined. Also, the standard and novel testing methods used in this particular research, in respect of the investigation of notch sensitivity of elastomers and the effects on fatigue life, are introduced.

Chapter Three gives a detailed description of the various test specimens, equipment, simulation and verification techniques used in the research. Chapter Four contains the results of the fatigue tests on both plain and notched dumbbells as well as comparisons of finite element simulations, which included photogrammetric measurements of the specimens used in the basic experiments. Chapter Five details a novel approach to the accurate modelling of elastomer behaviour to include stress softening and the verification of the technique using image correlation photogrammetry (ICP). Chapter Six contains a brief discussion of the results and their implications. Chapter Seven details the conclusions that are drawn form the research and Chapter Eight provides an outlook and discussion of how further research can be carried out to build upon the investigations described in this work.

Chapter 2 Literature Review

This research was conducted in order to improve how FEA currently models high strains and stress softening in elastomers. Consequently, the limitations of FEA and how improvements might be made must be considered. As a result, an understanding of the failings of the current material models was required from comparing simulations with data provided by measurement techniques not previously applied extensively to elastomers. Thereafter, it was possible using subroutines to improve how standard FEA code modelled stress softening. This wide ranging research required a broad literature review which encompassed the following areas:

- A description of the physical behaviour of rubber, particularly when it is subjected to repeated loading.
- A brief summary of current techniques to model hyperelasticity and viscoelasticity.
- The influence of notch sensitivity on elastomers.
- Measurement and analysis techniques used in the research, including FEA and 3D photogrammetry.

2.1 Physical Behaviour of Rubber

Though in limited use beforehand, over the passage of the last century, elastomers have been widely introduced and applied to a broad range of engineering and technical applications. Today, they are ubiquitous and the function of current technology without them is unimaginable. As the applications have proven to be more and more demanding, chemists, physicists and engineers have adapted and developed new generations of more versatile

materials suitable for ever more demanding applications and operating environments. This section gives an insight into the basic properties of elastomers that makes them so useful in engineering applications and indispensable in modern society.

2.1.1 Hyperelasticity

Elastomers are valuable materials in the field of engineering as they are capable of being subjected to large reversible strains under complex loading conditions without suffering significant permanent deformation or failure. They also have high coefficients of surface friction for rubber to rubber contact (or indeed when moving in contact with other surfaces) and an ability to dissipate energy. The characteristic of being capable of high reversible deformations is known as hyperelasticity. Figure 2.1 shows a stress strain curve for a carbon filled natural rubber subjected to a uniaxial deformation between -30% and +100% strain; this pointedly illustrates the properties of hyperelasticity, which makes elastomers so unique and useful from an engineering perspective.

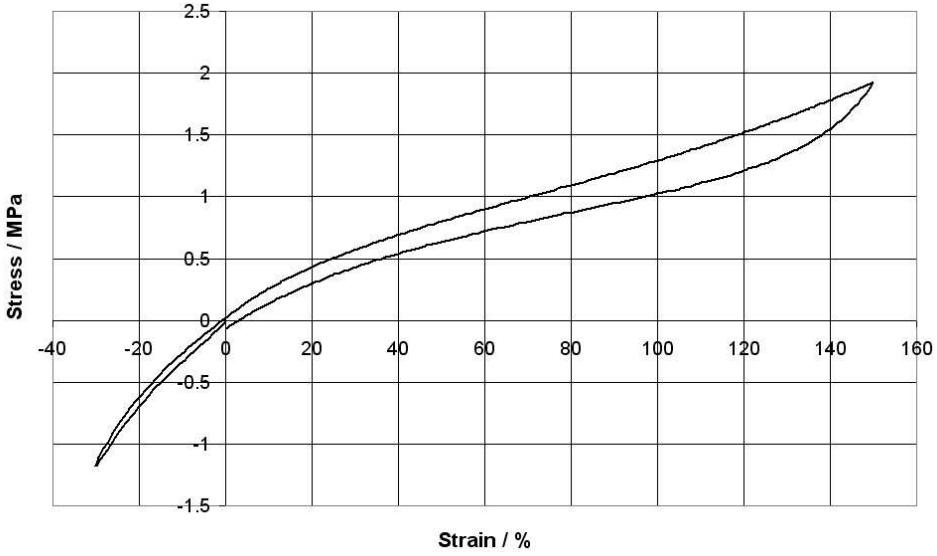

Figure 2.1: A typical stress strain curve for a filled rubber

Figure 2.1 was obtained from tests carried out during the research on dumbbell specimens in compression and tension to provide experimental data for fitting material models to as described later in Section 4.1.4. For the last seventy years researchers have studied the behaviour of elastomers and how to appropriately describe and explain hyperelastic behaviour under deformation. Numerous scientific theories have been formulated as a result (refer to Section 2.2). Phenomenological methods involved the study of rubber specimens under different conditions of homogenous strain **[4]** and use the assumption that the material behaves isotropically and that the polymer chain molecules are initially in a randomly orientated state. Then from experimentation, elastic strain energy functions were derived allowing stresses and strains to be obtained from FEA.

2.1.2 Viscoelasticity

Viscoelasticity is defined as the time dependent behaviour of a material. Due to the viscoelastic and hyperelastic nature of rubber it is inevitable that elastomeric components and specimens are sensitive to the application of different modes of loading, frequencies, strain rates and temperatures. When a specimen / component is subjected to continued loading under the same magnitude of force amplitude, the deformation and physical state of the rubber will change even though the magnitude and orientation of the load does not. The level of these changes will vary depending on the material and environmental and service conditions. Under service conditions, elastomeric components will be affected by the following viscoelastic phenomena:

creep – strain increases with the application of constant force,

stress relaxation – stress reduces with time when a component is subjected to constant strain,

set – the component will not recover its initial shape when an applied load has been removed.

stress softening (Mullins' effect) – the component softens with each successive loading, (described in greater detail in Section 2.1.3 and a central topic in this research)

Payne effect – amplitude dependence of the dynamic properties of filled elastomers, (described in greater detail in Section 2.1.4)

adhesion – a thermally activated stick-slip process that causes local bonding between rubber and rigid contact surfaces.

All elastomers display varying degrees of viscoelastic behaviour when subjected to cyclic loading for finite periods of time. Viscoelastic phenomena are present at all levels of deformation and across all temperature ranges and will occur for all deformation modes and types of loading. When these influences are considered in their totality, it is apparent that the modelling of each individual elastomeric component can be considered to be a unique problem due to each possessing a different loading history and experiencing different environmental conditions. Hence the phenomena must be carefully considered when materials are selected for specific applications and when material properties are being determined experimentally and defined prior to subsequent inclusion in simulations.

2.1.3 Stress Softening - Mullins Effect

All elastomers, both filled and unfilled, experience a phenomenon know as stress softening when subjected to cyclic loading. Stress softening is the dissipation of energy as a result of hysteresis effects as an elastomer is repeatedly subjected to cyclic loading **[5]**. It is manifested as a reduction in elastic modulus of the

material which takes place throughout the lifetime of a component. Carbon black and other fillers like silica are added to rubber in order to improve physical properties such as stiffness and abrasion resistance. Their addition is also necessary for economic reasons. Strain-induced stress softening in filled rubbers results from a breakdown of cross-links and a gradual detachment of the reinforcing fillers from the long chain molecules. This effect is known as the Mullins Effect in recognition of the research that he carried out into the phenomenon. One publication in particular **[5]** described many different stress-softening effects.

Figure 2.2 shows a typical Mullins effect, as characterised though the repeated loading of a dumbbell specimen. This specimen type is particularly advantageous as it can be cycled in both compression and tension **[6]**. The Figure illustrates the result for a carbon filled natural rubber dumbbell specimen, which was cycled 5 times in compression and tension between limits of a minimum of -30% in compression (compression ratio λ = -0.7) and to 100% in tension (stretch ratio λ=2) where λ is determined by adding one to the value of 'engineering strain'. It can be clearly seen that with each cycle the load required to cycle the dumbbell specimen between the same strain limits was reducing. From Figure 2.2 it is also evident that most of the stress softening occurs in the first cycle and that for the following four cycles the stress softening effects are greatly reduced. This phenomenon can be more or less pronounced depending on the base rubber material and the additives that make up the compound. Figure 2.2 comes from experimental data obtained during the course of the research to evaluate the amount of hysteresis and stress softening that occurs during cyclic loading in

compression and tension. The data was also used for fitting material models in the course of FEA simulations being carried out as described in Section 4.1.4.

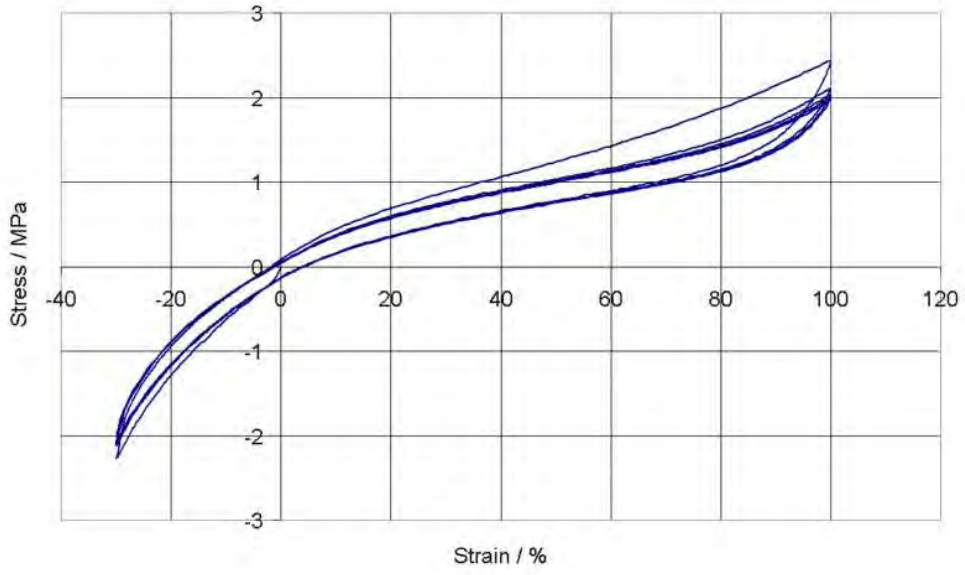

Figure 2.2: Stress Strain plot for a natural rubber carbon filled dumbbell specimen cycled five times from compression to tension

As stated, stress-softening effects can be explained by the breakdown of the filler structure within the elastomer and will result from interactions between the surfaces of the filler particles and the rubber as well as the breakdown of filler aggregates within the matrix. Figure 2.3 shows, to the left, a graphic of carbon black agglomerates with polymer chains and to the right, a Transmission Electron Microscope (TEM) micro-graph of a carbon black network obtained for an unstrained filled rubber sample. The mechanism of stress softening in filled elastomers is as follows: Under deformation, in the form of molecular slippage, an alignment of the polymer chains occurs with an increase in length which prevents rupture and so an increase in strength results. The effect of this is to uniformly distribute the applied stress and bring about a reinforcement of the compound. Also this process leads to a softening of the whole network at small strains.

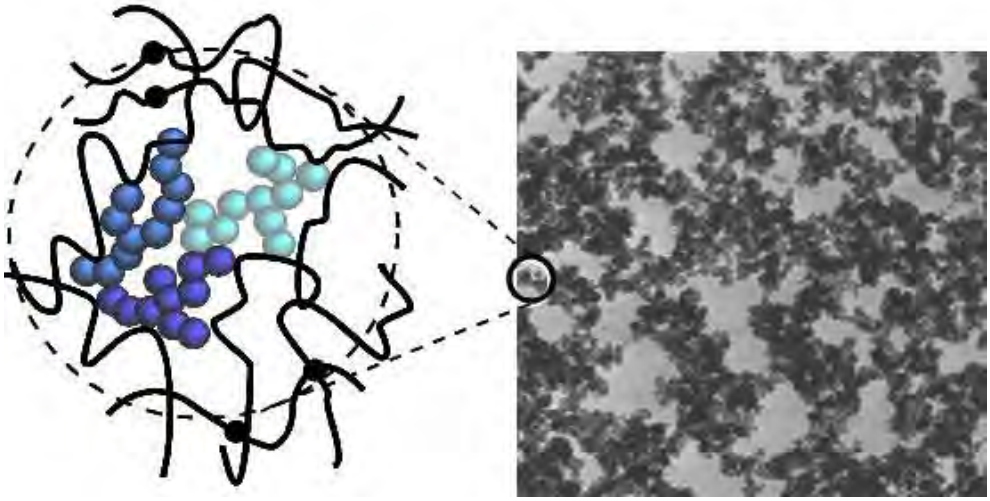

Figure 2.3: A TEM micro-graph of carbon black network obtained from an ultra thin cut of a filled rubber sample [7].

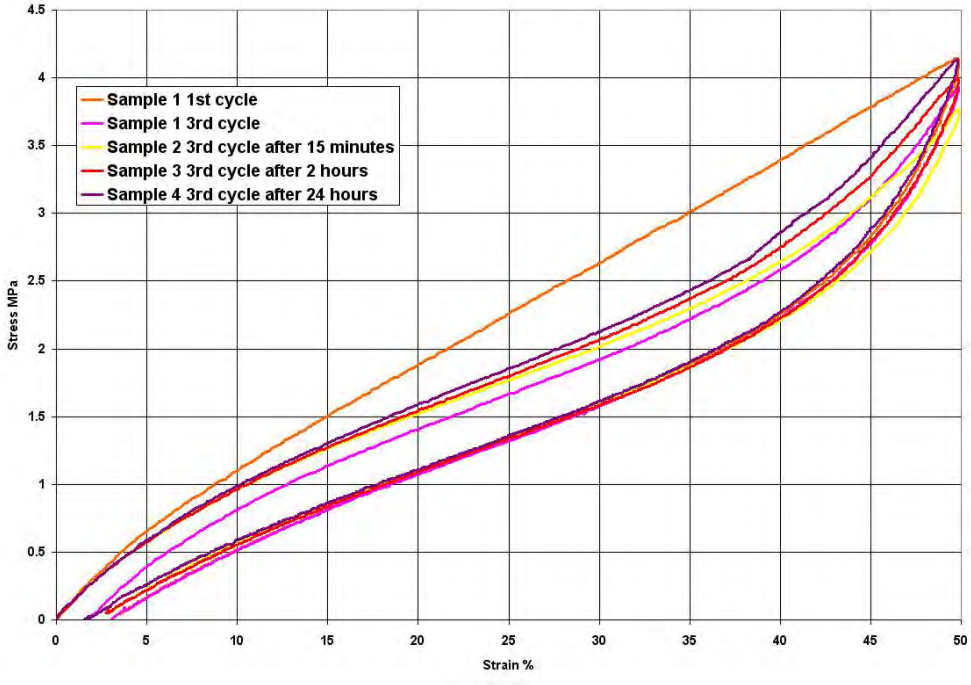

Figure 2.4: Recovery of S2 NBR samples with time after a 50% deformation.

An elastomer specimen or component that has been softened by previous loading will recover towards its initial physical properties if left unloaded for a period of time. However recovery is slow at room temperatures and more rapid at higher

temperatures. Figure 2.4 graphically illustrates this phenomenon through a short series of experiments carried out on acrylonitrile butadiene rubber (NBR) to examine the rate of recovery of the material after a tensile stress-strain deformation. Four S2 samples were cut from a 2mm plate and subjected to a deformation of 50% on a Zwick tensile testing machine (type 1445.17 fitted with a 5 kN load cell).

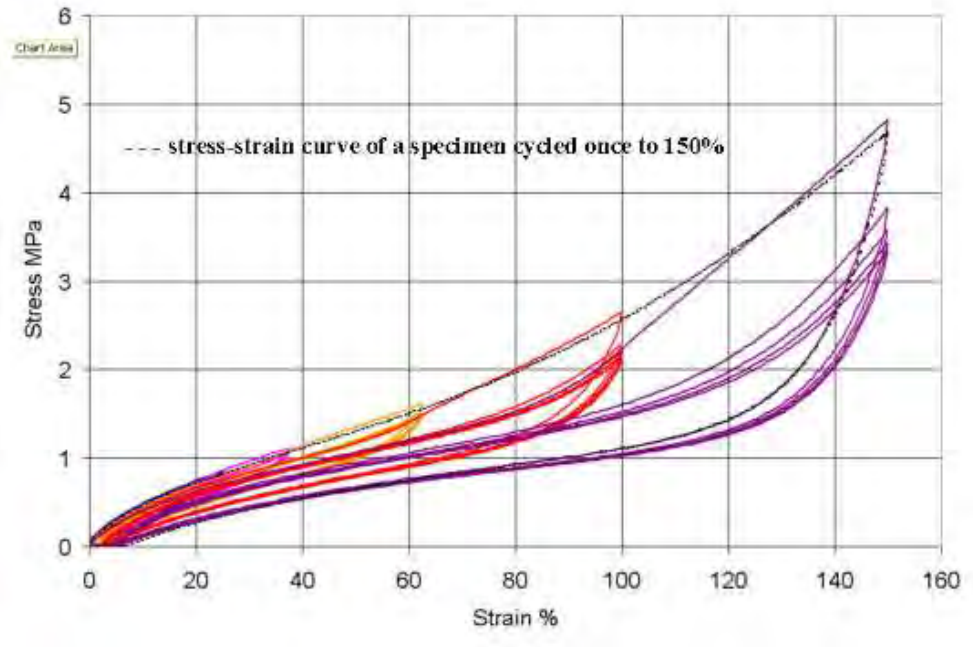

Figure 2.5: Stress induced softening of a carbon black-filled rubber

The first sample was taken as the reference sample and cycled three times and the hysteresis curves were recorded. Three more samples were taken and cycled twice each. After a dwell of 15 minutes, the first of these three samples was subjected to its third cycle. After a period of 2 hours, the second of the three samples was subjected to its third cycle and after 24 hours the last sample was subjected to its third cycle. It can be seen that with the passage of time there is a reduction in the maximum stress achieved during the application of the third cycle, which is most pronounced from two hours after the initial stress strain

cycling onwards. Figure 2.5 shows a series of tensile stress-strain tests of a dumbbell specimen, repeatedly cycled to higher strains. The curves are shown against a stress-strain curve of a specimen cycled once to 150% strain ($\lambda = 2.5$). Considerable softening was only present at elongations less than the previous cycle and at higher elongations the stress-strain curve was relatively unaffected by previous cycles.

2.1.4 Payne Effect

Experiments carried out by A. R. Payne **[8] [9]** on the amplitude dependence of the dynamic properties of carbon black natural rubber showed that the elastic modulus of the rubber was high at very low load amplitudes, but that when the dynamic strain amplitude increased, the modulus of the rubber decreased considerably (Figure 2.6 a diagrammatic representation of Payne's original).

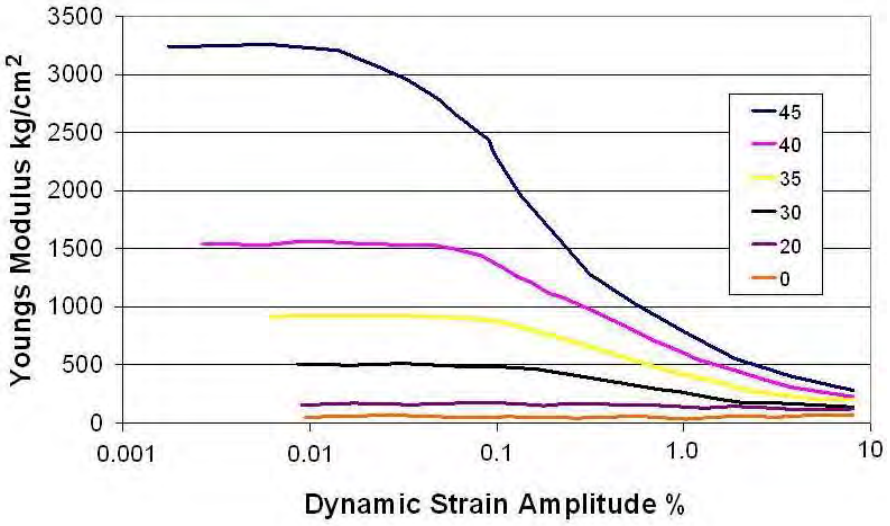

Figure 2.6: Dependence of complex elastic modulus E* on the dynamic strain amplitude for a natural rubber containing various loadings of % carbon black [9].

At high strain amplitudes, the modulus reduces so much that it approaches that of the unfilled rubber. This reduction in modulus is directly proportional to the

amount of filler in the rubber. Although the modulus is decreased with increasing strain amplitude, the loss factor, tan δ, increases until a filler specific maximum is reached, as shown in Figure 2.7, a diagrammatic representation of the effect (taken from his original). This phenomenon has become known as the Payne effect.

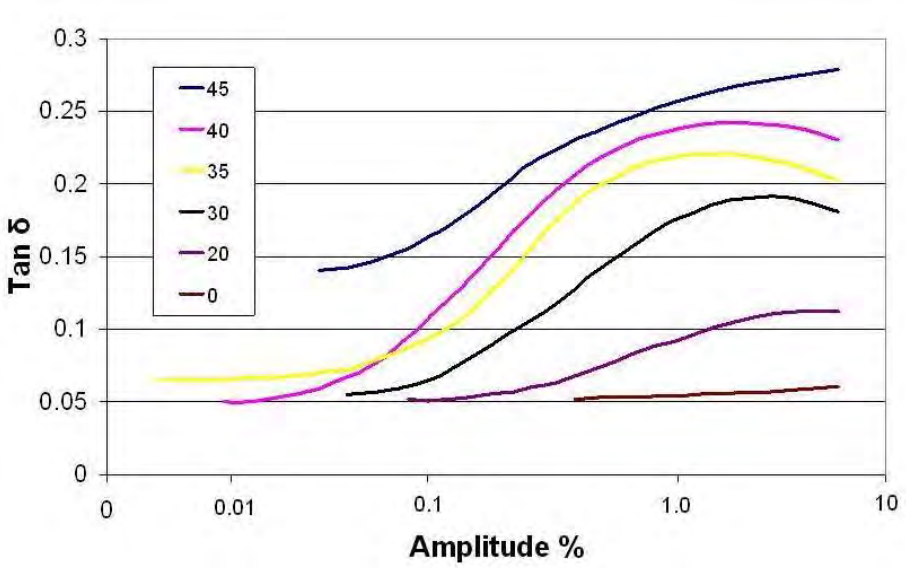

Figure 2.7: Influence of different levels of carbon black filler % on the loss factor tan δ under different dynamic strain amplitudes [9].

The Payne effect is most pronounced for active fillers such as carbon black and silica. These fillers have a higher influence due to their microstructure and crystalline form. Other fillers that do not possess these qualities have little or no effect on the dynamic amplitude / elastic modulus relationship.

Payne proposed an explanation for the varied behaviour at different dynamic amplitudes and attributed it to filler - filler interaction. Other characteristics at different strain amplitudes, which are independent of the strain, are accounted for in three different ways. Firstly through the modulus of the unfilled rubber, secondly there are the hydrodynamic effects of the hard solid filler in the softer rubber matrix and thirdly there are some strong links between the filler and the polymer matrix depending on the filler activity.

2.1.5 Gough-Joule effects

Of equal importance and related to the mechanical properties of elastomers are the thermoelastic properties. The initial and fundamental studies of thermoelastic properties were made by Gough and Joule in the 1800's, to whom two major observations are attributed **[10]**:

- When rubber is held in a stretched state under constant load and is heated it begins to contract (this behaviour is reversible).
- Rubber gives out heat (also reversibly) when stretched.

These observations are key to understanding the behaviour of rubber under deformation.

2.2 FEA of Rubber-Like Materials

To date, FEA code applied to elastomers has been predominantly based on hyperelastic modelling which uses phenomenological models. Hence, semi-empirical formulae (strain energy density functions) have formed the basis of constitutive equations for the physical behaviour of rubber, where material constants were derived from physical testing and subsequently input to FEA. These equations tend to be of two types; those based on strain invariants, typified by the James Green, Simpson formula **[11]**, or those based on stretch ratios of which the Ogden formula **[12]** is the most universally accepted and applied.

Hence, strain energy density (W) can be expressed in two ways. The Mooney Rivlin equation 2-1 is the most widely used example of the first type of function **[13] [14].** It defines W as a polynomial function of strain invariants (I). Higher order polynomials have a greater ability to accurately describe the behaviour of elastomeric materials.

$$W = C_{10}(I_1-3)+C_{01}(I_2-3)+C_{11}(I_1-3)(I_2-3) \qquad \text{Eqn. 2-1}$$

Alternatively, the Ogden model (2-2) is expressed in terms of the principal stretch ratios (λ) (determined by adding one to the value of 'engineering strain' as shown in equation (2-3)):

$$W = \sum_{n=1}^{N} \frac{\mu_n}{\alpha_n}(\lambda_1^{\alpha_n} + \lambda_2^{\alpha_n} + \lambda_3^{\alpha_n} - 3) \qquad \text{Eqn. 2-2}$$

$$\lambda = 1+\varepsilon \qquad \text{Eqn. 2-3}$$

Where the terms α_n can have any positive or negative value and the μ_n terms can be either positive or negative as long as the product of α and μ terms is positive.

2.3 Localised Strain and Notch Sensitivity

Practically all engineering materials will fail under numerous repetitions of a load that would be less than that required to produce an immediate catastrophic failure. This phenomenon is known as fatigue.

In the literature published to date on fatigue in engineering materials, only a minute portion of the research pertains to elastomers by comparison with a significant body of work devoted to metal and polymer fatigue failures. Consequently, the effect of geometry on the fracture process in elastomers is not very well understood **[15]**. Additionally, most of the specimens used to study fatigue and crack propagation are typically planar and taken from thin elastomer sheet. Also, to aid the study of crack propagation, small incisions are often made to induce crack growth from a known point. This is done in order to reduce the

amount of scatter in the results as cracks normally emanate from flaws in the sample. The problem with this approach is that although predefined cracks in specimens reduce the amount of experimental scatter (and hence the large number of samples required to get a precise understanding of the fatigue life of a specimen) the information obtained from the experiments tends to be merely specimen specific and is unlikely to relate to the behaviour of actual components in realistic service conditions **[16]**.

In contrast, for linear elastic engineering materials, extensive research has been carried out and documented, wherein various formulae and material charts for stress concentration factors have been extensively compiled **[17] [18]**.

The predominant work on nonlinear materials and the application of classical notch sensitivity theory is focused on polymeric materials under both static and dynamic fatigue conditions **[19]**. A counter-intuitive finding worthy of note from the work of both Balazs and Peabhakaran et al **[20] [21]**, was that when applying conventional notch sensitivity criteria to polymeric materials, negative values of notch sensitivity were encountered. Balazs termed this behaviour anomalous. This implied that the presence of a notch actually strengthened the specimens under fatigue. Several theories were postulated in order to explain this phenomenon, but not proven. Strain crystallisation for example in the high strain region of a crack tip may impede the propagation of the crack causing it to change direction and slow crack growth.

Novel research was carried out by Abraham et al **[22] [23],** which investigated the effect of minimum flaw size on the fatigue life of non strain-crystallising elastomer

specimens. It shed light on the initiation of cracks that lead to crack propagation under fatigue conditions and this will be discussed in greater detail in Chapter Four.

Part of this research programme investigated the application of linear classical notch sensitivity theory to elastomers and the effect of induced stress concentration on the fatigue life of elastomers. The data in respect of the number of cycles to failure of the material is presented in the form of S-N (Wöhler) curves, where the maximum engineering stress is plotted against the number of cycles to failure.

2.4 Physical Testing Techniques Used in the Research

The measurement techniques used in this work focused on two main methods of testing. The first was quasi-static uniaxial (both tensile and compression) loading and equi-biaxial tests carried out on a Zwick tensile testing machine (type 1445.17) fitted with a 2.5kN load cell.

The second type of testing conducted were dynamic fatigue to failure tests which were carried out using two different MTS servo hydraulic elastomer testing models with TestStar^{TM} control software systems **[24]** allowing the dynamic properties of the rubber samples to be recorded throughout the fatigue to failure test procedure. These two MTS systems have been used extensively previously by Abraham et al **[25]** for the investigation of the effects of different loading modes on fatigue life of non strain-crystallising elastomers and Le Gal et al **[26]** used them when investigating friction between elastomers and different rough surfaces.

The purpose of the quasi-static tests was to characterise the basic physical properties of each material observed under different deformation modes and to

provide material specific data for fitting material models for FEA simulations that were to be carried out as part of the research programme.

The dynamic fatigue to failure tests were conducted to compile S/N (Wöhler) curves for each of the materials studied in order to improve the lifetime predictions for practical applications in industry. To improve the understanding of how elastomer components behave under fatigue conditions, further fatigue measurements were made on modified specimens to look at the influence of stress raisers on fatigue life.

To provide a greater understanding of the behaviour of the elastomers under testing conditions, two optical measuring techniques were employed. The first, image correlation photogrammetry (ICP), was used to measure three dimensional geometric deformations of elastomer specimens in both quasi-static and dynamic tests. Further, ICP was used to verify the validity of FEA simulations incorporating stress softening subroutines derived from experimental data. The use of this system for the measurement of high deformations in elastomers provided a relatively new and novel application for the technology. Previously the system was used for the measurement of linear elastic materials **[27]** and for providing measurement of materials used in biomedical applications **[28]**.

The second optical test method used was short-wave thermography, employing a commercially available infra red camera system manufactured by Jenoptik known as VarioTHERM **[29]**. This was used as a control measure to investigate the thermal build up in the elastomer specimens during dynamic fatigue to failure tests. The control measure was necessary to ensure that the test conditions used (such as load amplitude and frequency) were not inducing elevated temperatures in the specimens, as this would have an undesirable influence on the material

properties and consequently have a possible adverse effect on the fatigue life prediction of the elastomer specimens which would not be related to notch sensitivity or localised stress softening **[30]**.

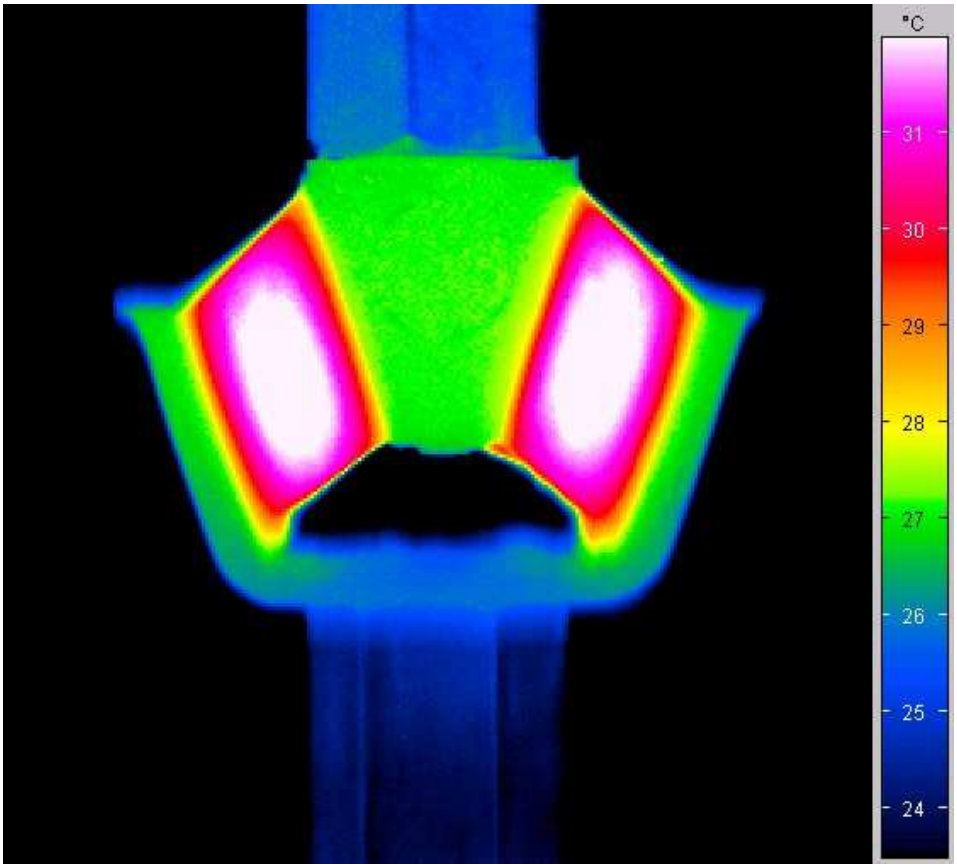

Figure 2.8: Thermal build-up in a rubber bearing

An example of thermal build-up in an automotive component is shown in Figure 2.8, where a rubber mounting was subjected to a deformation of 6mm at a frequency of 3Hz. This component was cycled under normal operating conditions where only a modest temperature increase was measured. However under more extreme loading conditions, larger temperature increases can occur which can have detrimental effects on elastomer components and test specimens, as is considered in Section 3.5. Figure 2.8 was captured by the author in a study of heat build-up in a commercial component as part of a project with an industrial partner at DIK.

Chapter 3 Procedures, Methodologies and Design

This Chapter describes the different test samples, methodologies and techniques used throughout the research.

3.1 Physical Test Samples Used in the Programme

Some test samples conformed to ISO standards, such as the S2 uni-axial test specimens, while others (e.g. notched dumbbell specimen used in the fatigue to failure experiments) had to be modified to include stress raisers or discontinuities that would not normally be present in typical components.

3.1.1 S2 Uniaxial Test Specimen

Uniaxial Tests were carried out using S2 samples, also known as dog-bone specimens **[31]**. The S2 sample is a standard test-piece used in uniaxial tests to characterise elastomer materials loaded in one plane. It can be used for multi-cycle hysterisis tests, carried out to various strain levels, at various rates and also to determine the failure stress and maximum strain of elastomers. The data from these tests can be employed in the fitting procedures for FEA material model determination to provide realistic constants for elastomer constitutive equations. The S2 specimen has an overall length of 75mm and gauge length, width and thickness of 20mm, 4mm and 2mm respectively and is illustrated in Figure 3.1. Two reflective points are applied to the specimen which allow the extensometer on the Zwick tensile testing machine, described in Section 2.4, to optically measure the integral strain (percentage strain applied to the gauge length) of the specimen.

Figure 3.1: S2 sample as used for tensile stress strain measurements

3.1.2 Dumbbell Samples

Figure 3.2 shows a model of a dumbbell test specimen that was used for uniaxial fatigue to failure measurements and also for uniaxial stress-strain measurements, both in tension and compression. The major and minor diameters of the test-piece were nominally 25 and 15 mm respectively and the fillet radius was 5 mm. The gauge length of the specimen was 25 mm. The geometry of this type of specimen allows it to be subjected to a compression of up to 30%. This test-piece was used by Abraham et al **[32]** for their investigations into fatigue properties of non strain-crystallising elastomers and is effective because it allows a consistent extension and compression (strain or load controlled cyclic deformation) to be applied to the gauge length of the sample **[6] [33]**.

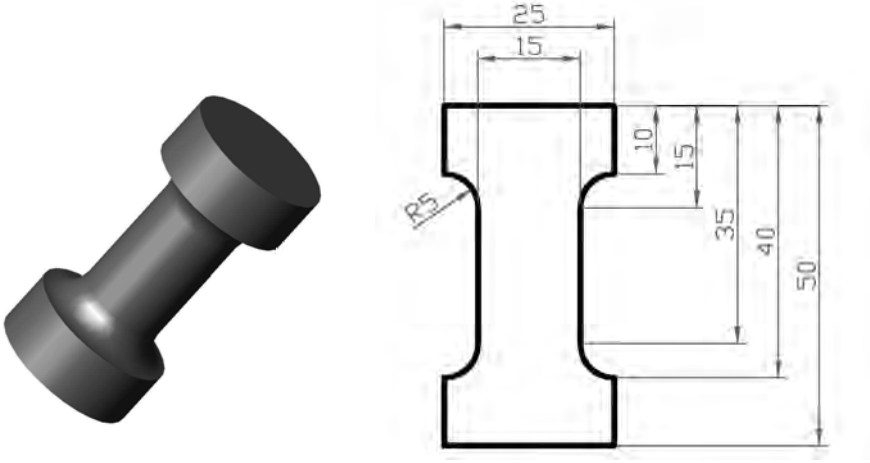

Figure 3.2: A dumbbell test specimen used in the uniaxial tension and compression stress-strain experiments.

3.1.3 Notched Dumbbells

Variations in the design of this specimen were introduced in order to investigate the influence on fatigue life of different stress raisers. The samples are known as notched dumbbells and are illustrated in Figure 3.3.

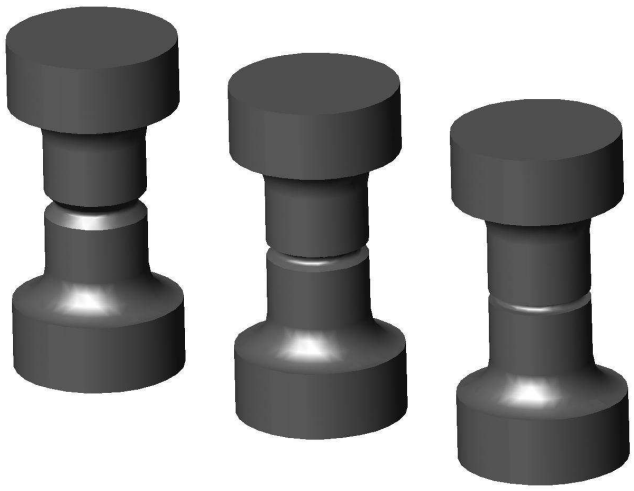

Figure 3.3: Three notched dumbbells with varied notch severity.

A Major Diameter (mm)	B Minor Diameter (mm)	C Angle Of Notch	D Fillet Radius (mm)
15	12	90°	0.75
15	12	90°	0.375
15	12	45°	0.75
15	12	45°	0.375
15	12	0°	0.75
15	12	0°	0.375
15	9	0°	0.75
15	9	0°	0.375

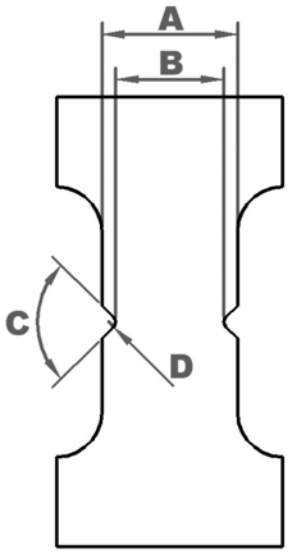

Table 3-1: Variation of Specimen dimensions of notched dumbbells

The minor diameter B was 0.8 times the major diameter A. The fillet radius D had two values related to diameter A thus:

D = 0.05A

D = 0.025A

The overall dimensions remained the same except that samples were moulded with a Vee notch around the circumference at the longitudinal centre of the gauge length of the sample. The samples had different levels of notch severity introduced by means of variation in angle and fillet radius at the tip of the notch, as shown above in Table 3.1.

3.1.4 Equi-Biaxial Tests

The bi-axial measurements were carried out on a stretch frame test rig which was mounted on the same Zwick tensile testing machine as the tests on the uniaxial S2 samples.

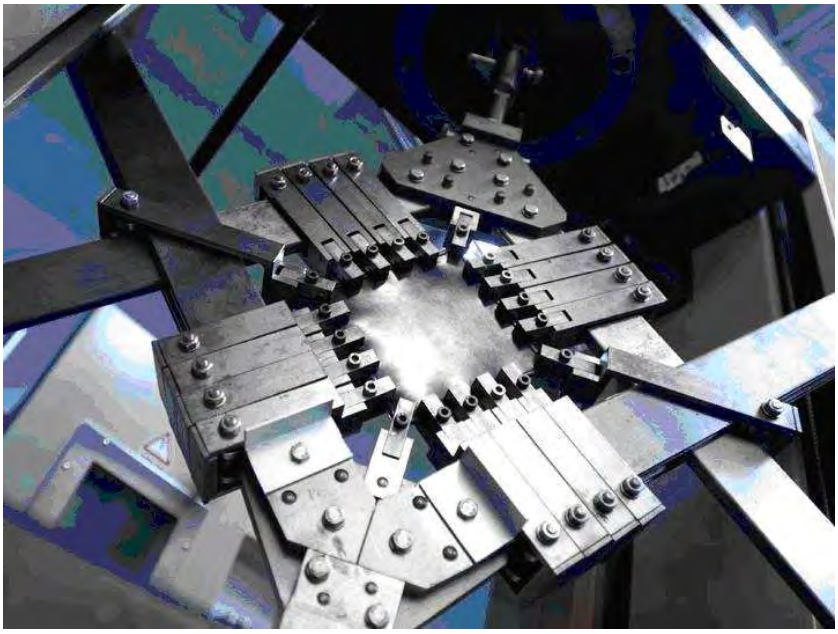

Figure 3.4: Equi-biaxial specimen clamped in a stretch frame rig.

The specimens' dimensions were 116 x 116mm square including a 4.5mm rib bordering the specimens. Each specimen had a uniform thickness of 2mm in the

gauge area. Figure 3.4 shows a specimen clamped in the stretch frame rig being subjected to an increasing integral equi-biaxial strain. This specimen and test method has some limitations in that the gauge area of the specimen is relatively small, within the clamping mechanism there are friction and inertia losses and very large stress concentrations occur at the clamps, which can lead to unanticipated early specimen failure outside the area of interest.

3.1.5 Single Edge Notched (SEN)

The SEN specimen (as illustrated in Figure 3.5) is normally used to measure dynamic crack propagation in elastomers. The specimens measured 65mm in length, 15mm in width and were 2mm thick. The cuts or notches were made using a razor cut while the sample was secured in a holder to ensure a perpendicular cut in the middle of the specimen. As can be seen in Figure 3.5, the specimen has a rib on both ends to allow clamping of the specimen during loading.

Figure 3.5: SEN specimen with ribs to aid clamping

3.1.6 Modified Single Edge Notched (SEN)

The modified SEN specimen measured 65mm in length with a width of 30mm. A 6mm diameter axially central hole was punched in each specimen. The specimens were prepared using the same mould as the SEN specimens and so also had a rib at each end to assist clamping.

3.1.7 Modified SEN with 90° Vee Notch

A variation of the SEN specimen possessed a 90° Vee notch of 5mm (unstrained) depth and a fillet radius at the root of 0.3mm replacing the cuts previously described. The fillet radius at the vee tip was introduced in order to study how the sharpness of a crack tip affected the maximum local strains.

3.1.8 Pure Shear (Planar)

The planar specimens (an approximation of pure shear specimens) measured 20mm in length, 200mm in width and had a thickness of 2mm.

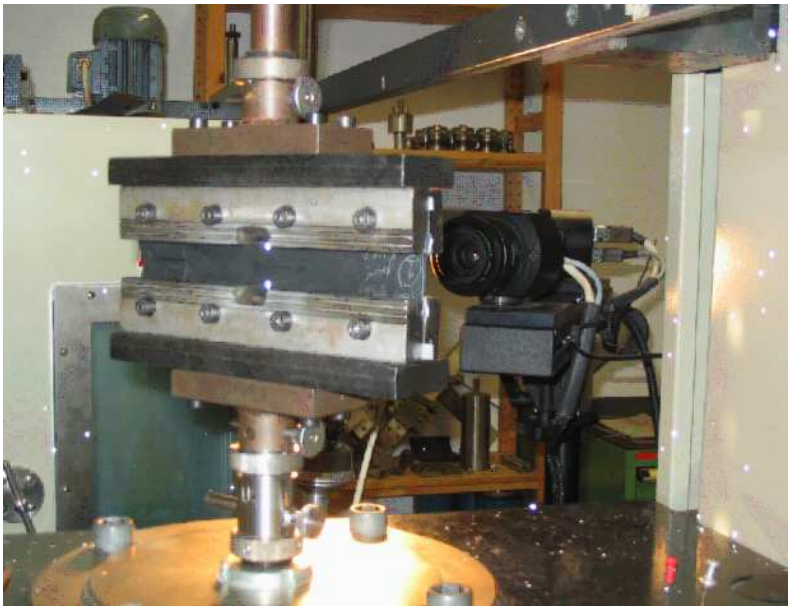

Figure 3.6: ICP system and experimental set up with a planar specimen clamped at 0% integral strain.

An example of the pure shear specimen can be seen above in Figure 3.6 mounted in the Zwick tensile testing machine, where a measurement is about to be made using the ARAMIS ICP system. The test is not strictly speaking a pure shear test as under load the free sides of the specimen can neck inwards as the restrained sides are pulled in tension. This would not be the case in a pure shear test (which would require tensile loads in three mutually perpendicular planes) but is considered to be a close approximation of that deformation mode.

3.1.9 Double Shear Sandwich

The double shear sandwich is a modified shear test, which was devised at the Deutsches Institut für Kautschuktechnologie (DIK). Two 10mm diameter discs of 2mm thickness are glued to fixtures, which are then clamped on the MTS elastomer testing system and loaded in shear as shown in Figure 3.7.

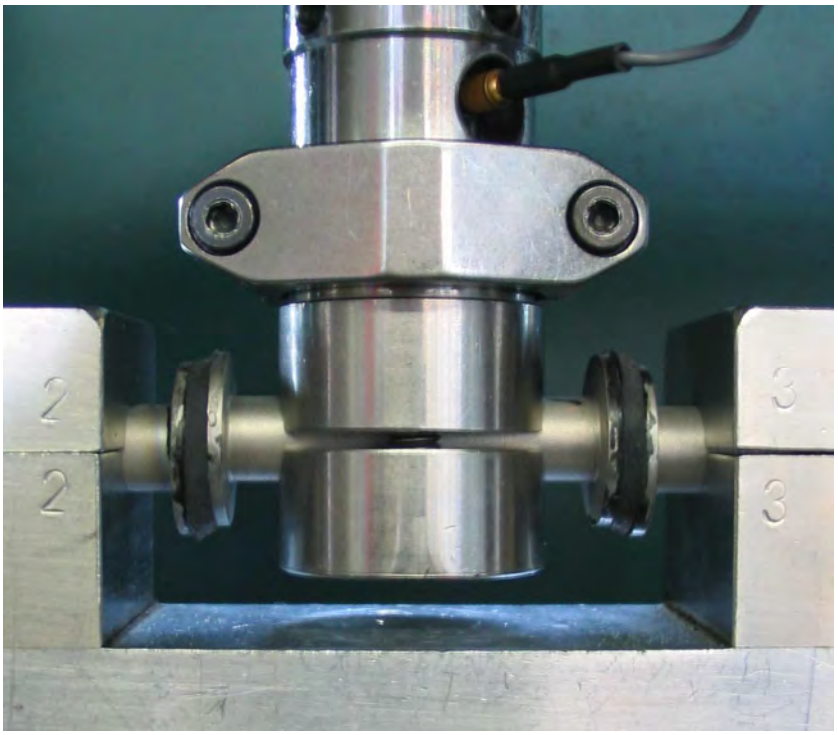

Figure 3.7: Double shear sandwich test specimen under deformation on the MTS elastomer testing system.

3.2 Materials and Equipment

Throughout this research programme several materials were used. These were rubber compounds used for commercial purposes and also model materials. It is important to understand the difference between model and commercial materials. Due to the commercially sensitive nature of the ingredients of the latter materials, the chemical composition was confidential and not released by the industrial partners on the project. For this reason, DIK had two model materials included in the project for which the chemical composition was precisely known. These materials are not typically used in commercial or dynamic applications but are used at DIK to illustrate how different mixing procedures and fillers can affect the mechanical properties of elastomeric material. Table 3.2 provides a summary of the materials used in the research.

Material	**N1 M** (NR)	**E1 M** (EPDM)	**NB P** (NBR)	**N1 P** (NR)	**N2 P** (NR)	**N3 P** (NR)
Designation of Material	Model Material	Model Material	Commercial Material	Commercial Material	Commercial Material	Commercial Material
Hardness Shore A	53	59	78	62	64	39
G* (Pa) at 23ºC	2.64E+06	3.38E+06	1.21E+07	5.39E+06	7.02E+06	1.46E+06
Carbon Content	30 phr	50 phr		60 phr		40 phr

Table 3-2: Summary of materials used in the research.

The mixing of the materials took place on industrial scale mixers so that the filler dispersion in the materials was the same as for materials used in actual components. The NBR was a silica filled system and was used in sealing applications, while the commercial natural rubber (NR) materials were used in vibration absorption applications. The model materials used were carbon filled

NR and a carbon filled Ethylene-Propylene-Diene Monomer (EPDM) material. The ingredients for the two model materials are listed in **tables 3-3 and 3-4**.

Component	Pphr	Function
EPDM Keltan 7631 A	140	Polymer
Carbon Black N550	50	Reinforcing filler
Zinc Oxide (ZnO)	4	Activator
Stearic acid	2	Plasticiser
Sulphur	0.7	Curing Agent
TBBS	1	Accelerator
TBzTD	3.5	Accelerator

Table 3-3: The chemical composition of the filled EPDM (Ethylene-Propylene-Diene Monomer) E1M Model Mixture.

Component	Pphr	Function
NR (CV 60)	100	Polymer
Carbon Black N-774	30	Reinforcing filler
IPPD	2	Antioxidant Anti-Aging
TMQ	1	Antioxidant Anti aging
Antilux 500	2	Light Protection Anti-Aging
ZnO RS	5	Activator
Stearic Acid	2	Anti aging
CZ (CBS)	2	Accelerator
Sulphur	1.5	Curing Agent
Thiuram (TMTD)	0.2	Accelerator

Table 3-4: The chemical composition of the carbon filled NR (Natural Rubber) N1M Model Mixture.

The vulcanisation or cure times for each material were determined on a Monsanto Rheometer which yielded data in the form of a vulkameter curve (see Figure 3.8). The machine was set at the material appropriate temperature, typically anything from 150-160°C; it then measured the increase in torque required to displace the material with time as the vulcanisation process took place. The results were plotted on a graph of torque versus time as shown in

Figure 3.7. From the graph, t_{95}, or the time to reach 95% of the maximum torque, is taken as the vulcanisation time for a 2mm thick sample. For samples of greater thickness than this, an increase in the time period was required.

The vulcanisation temperatures for each material varied depending on the industrial application. The NBR material was vulcanised at 160°C, whereas the NR materials were vulcanised at a temperature of 150°C. The reason for this was that the industrial application required rubber to metal vulcanisation. This necessitated the application of a bonding agent to the metal parts. This agent would degrade if the temperature exceeded 150° and the component would be rendered defective.

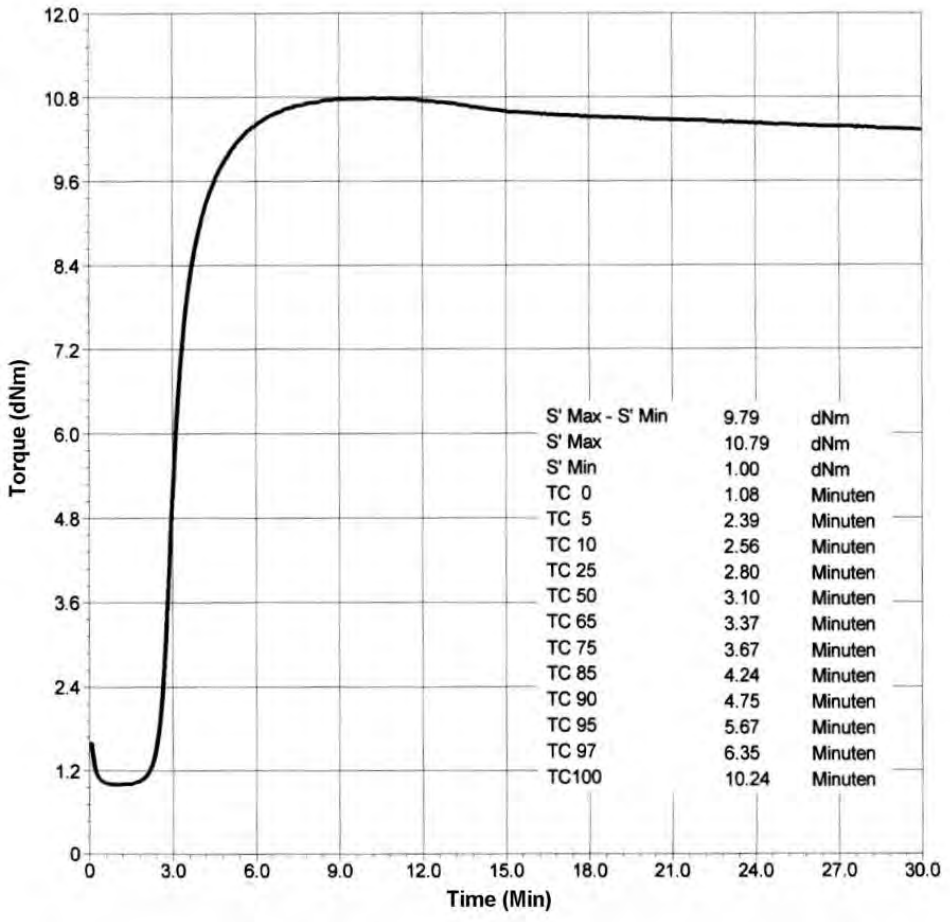

Figure 3.8: Vulkameter curve for the N1 M material.

The EPDM and the NR model materials were vulcanised at 150°C. The vulcanisates for all materials were made using compression moulds in a heated hydraulic press under a pressure of 200 bar and at the appropriate temperature for each material.

The various samples were prepared at intervals of several weeks or months due to the test schedules and the time required for the preparation procedures, especially for the dumbbell samples. In the meantime, the materials were stored in a freezer at -20°C and only removed and thawed out for sample preparation. Each time, a fresh curve was generated on the Monsanto Rheometer, to ensure that the cure time had not changed due to scorch or degradation of the material.

3.3 Test Parameters

Meeting the research aim and objectives necessitated a comprehensive test programme which encompassed static, quasi-static and dynamic tests. The tests were carried out in order to characterise the elastomeric materials in relation to each other, but also to provide experimental data to which material models could be fitted for the purpose of nonlinear FEA. This would enable accurate simulation of the behaviour of specific elastomers deformed under laboratory conditions. The following tests were conducted:

- Shore A hardness
- Uniaxial S2
- Uniaxial dumbbell
- Cylindrical compression
- Variations of pure shear or modified planar
- Equi-biaxial
- Double shear sandwich

A range of extension rates were chosen for the series of tests and initial dynamic uniaxial tests are described here.

S2 samples were cut from a 2mm sheet and placed in the Zwick tensile testing machine and cycled five times to 100% strain at three different feed rates: 5mm/min, 50mm/min and 500mm/min. The first cycles are shown in Figure 3.9. From the graph it can be seen that the maximum stress achieved during the test is dependent on the strain rate and this characteristic has been observed by others **[34]**. Less simultaneous stress relaxation can take place at higher feed rates, hence the 500mm/min tests can be assumed to approximate to a quasistatic test.

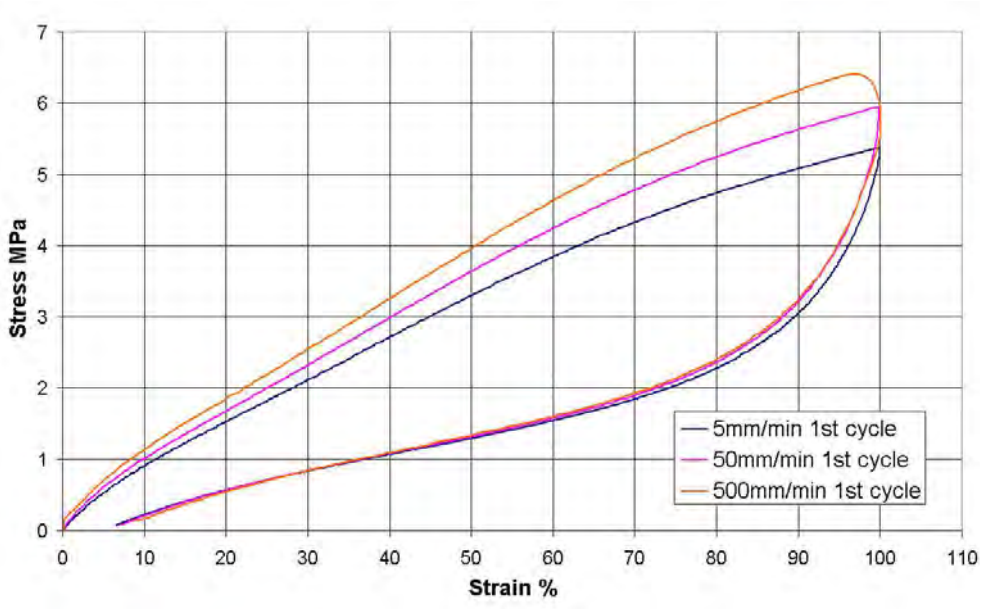

Figure 3.9: NBR S2 specimens strained to 100% at varied feed rates.

However a limitation of using this feed rate is evident. When running at the rate of 500mm/min (the recommended speed for uniaxial tests according to ISO standards), as the crosshead approaches the maximum strain point it inevitably begins to slow down resulting in a drop in the stress before the maximum strain point is reached. This behaviour occurs at the lower speeds but has no significant influence on the results. Consequently, for all the quasi-static tests

carried out over the scope of this project it was decided to use feeds per minute equivalent to 100% of the initial length of the specimen between the clamps. For example S2 specimen with a gauge length of 50mm would be tested at a feed rate of 50mm/min and so on. Hence the rate of simultaneous stress relaxation would be proportionally the same for all samples. Feed rates for all the characterisation tests are detailed in Section 3.4 which describes basic testing.

3.4 Basic Testing

Generally, basic testing in the elastomer industry is carried out for quality control purposes to ensure that products are produced in a consistent manner with consistent material properties. The ISO tensile test for example, where an S2 specimen is stretched to failure, can be used to determine how well carbon black is dispersed, or to examine the cure state. Deficiencies in both of these properties may be manifested in a lowering of tensile strength. The data obtained from the tests can also be used by engineers to define properties that are required for particular applications. As the standard ISO tests are for quality control purposes, specimens are normally only cycled once to failure. The first cycle however, as shown in Figure 2.4, is not representative of typical material behaviour and so is of little use for fitting in FEA code due to the large amount of hysteresis and stress softening which will occur over the first three cycles (and beyond, to a lesser extent). For this work, in order to obtain useful data, the specimens were cycled five times and the fifth loading cycle was taken to be representative of the material behaviour after conditioning and hence used for fitting in FEA code to allow more accurate simulation of elastomeric component behaviour. This is accepted practise in industry.

Shore A Hardness Testing

This test can be very useful as it allows elastomers to be compared in relation to each other in a quick and repeatable manner. Shore A hardness is measured using a Durometer, where an indentor is pressed into the material and the depth of the indentation is measured under specific conditions **[35]**. This gives an indication of the hardness of the material, determined from the depth of the penetration of the indentor, which is inverse to the hardness of the material and is dependent on the modulus of elasticity and the viscoelastic properties of the material. In the case of the materials investigated here, the Shore A hardness of each sample was measured at room temperature and on a stand mounted digital Shore meter with a timer, which allowed the hardness to be determined consistently throughout the series of tests. In each test, a reading of hardness was taken after a three second constant force application of a standard indentor to a 6mm thick specimen (taken in each instance from a previously prepared plate of the material). The final value obtained was an average of five tests taken on different parts of the plate but at least 12mm from the edge of the specimen in all tests. This procedure complies with test standard ISO 7619:1997,

Calculating FEA Coefficients from Shore A Hardness.

Several approximate “rules of thumb” methods have been developed empirically to obtain Mooney-Rivlin coefficients. These techniques are very useful in that they can eliminate expensive testing and curve fitting to the experimentally obtained data. Experimentation carried out in support of this research project has shown that the application of these methods in modelling simple components

such as cylindrical bearings, is practically as good as using the generally accepted regression analysis techniques.

One such method is based on the assumption that two times the sum of the two Mooney-Rivlin material coefficients [$2(C_{10}+C_{01})$] equals the initial shear modulus (G) and the value of Young's modulus is approximately three times the shear modulus for an incompressible material **[36]**. The procedure is as follows:

1: Record a durometer reading H_A and determine a Young's modulus from it using:

$$E\ (MPa) = (15.75 + 2.15\ H_A) / (100 - H_A) \qquad \text{Eqn. 3-1}$$

and divide E by 6 to obtain C_{10} (MPa) *

Using this result $C_{01} = 0$ can be specified to obtain a neo-Hookean Mooney Rivlin single term material model.

2: Once the analyst has calculated a value for C_{10} and wants to include a non-zero value for C_{01} in order to use the more accurate two term Mooney-Rivlin material model the following can be used as an approximation:

Set $C_{01} = 0.25\ C_{10}$ and solve the following equation for C_{10}

$$6(C_{10}+C_{01}) = E, \text{ therefore, } 6(C_{10} + 0.25\ C_{10}) = E, \qquad \text{Eqn. 3-2}$$

and C_{10} = E / (6*1.25) (MPa) Eqn. 3-3

The assumption that C_{01}= 0.25 C_{10} MPa can be refined by using the following relationship: $0.25C_{10}$ can be used for a soft rubber but varying in value down to $0.1667C_{10}$ for a hard rubber.

* Alternative formulae for approximating E from hardness readings achieved using a durometer are given here.

A semi-empirical formula is offered by Gent **[36]**.

This relation has the form

$$E = \frac{0.0981(56 + 7.66S)}{0.137505(254 - 2.54S)} \quad \text{Eqn. 3-4}$$

where E is the Young's modulus in MPa and S is the Shore hardness. This relation gives a value of E = ∞ at S = 100 but departs from experimental data for S < 40.

Another relation that fits the experimental data slightly better is **[37]**

$$S = 100\ erf\left(3.186 \times 10^{-4} E^{1/2}\right) \quad \text{Eqn. 3-5}$$

where erf is the error function and E is in units of Pa.

Essentially Shore A and D are the most commonly used methods of the measuring the hardness of elastomers and polymers, but using different scales. 'A' is for soft materials and 'D' is used for harder materials. In addition to the difference in the scale there are differences in the indentor shape used in the Durometer.

A first order estimate of the relation between Shore D hardness and the elastic modulus for a conical indenter with a 15 degree cone is **[38]**

$$S_D = 100 - \frac{20(-78.188 + \sqrt{6113.36} + 7.81.88E)}{E} \qquad \text{Eqn. 3-6}$$

where S_D is the Shore-D hardness and E is in MPa.

Another linear relation between the Shore hardness and Young's modulus is applicable over a large range of Shore A and Shore D hardness. For shore D hardness and the elastic modulus for a conical indenter with a 15 degree cone is given by equation. 3-6 **[38]**.

$$\log E = 0.0235S - 0.6403; \quad S = S_A \quad for\ 20 < S_A < 80$$

$$S = S_D + 50 \quad for\ 30 < S_D < 85$$

where S_A is the Shore A hardness, S_D is the Shore D hardness, and E is the Young's modulus in MPa.

Uniaxial S2 Samples

The specimen dimensions were in compliance with ISO 37 for the determination of the tensile properties of elastomers. In accordance with the standard the tests are normally used to determine the stress produced at particular elongations, 100 or 300% for example, for quality control purposes. The ISO standard can also be used to measure the tensile strength and percentage elongation at break. The specimens are prepared as described in Section 3.1.1 and tested at the feed rate of 50mm/min for the reasons outlined in Section 3.3. Two series of tests were carried out on S2 specimens, multi-hysteresis tests where S2 specimens were cycled five times to incrementally higher strains. The second set of tests required individual samples to be cycled five times to a fixed maximum strains. This was

done so that a comparison could be made between the effects of damage in each cycle and between materials. The data was used for fitting in FEA as well as for comparison purposes.

Dumbbell Uniaxial Samples

The specimens, as described in Section 3.1.2, were used for both uniaxial compression / tension and fatigue to failure tests in order to compile Wöhler (S/N) curves for material performance. For the static uniaxial tests, a feed rate of 20mm/min (which equated to 100% of the specimen length between the clamps) was used. The fatigue to failure tests were carried out under load control at a frequency of 1Hz, as explained in Section 3.5. The results were also compared to S2 sample results to discern any noticeable difference and to determine if the specimens were suitable substitutes for those defined in the ISO standard test. Another advantage of the uniaxial tests (as shown in Figure 2.2) is that the specimens can be cycled easily in compression as well as in tension. The compression cycles can go to 30% with out any significant barrelling being evident. The feed rates were maintained at 100% of the material initial gauge length (in this case, the distance between the clamps) meaning that the dumbbell samples were deformed at a rate of 20mm/min. Another advantage of the dumbbell samples is that they allow fatigue to failure tests for use in compilation of S-N curves for the different elastomer materials. The feed rates for the fatigue to failure tests however were not determined by the amount of material between the clamps, but dictated by the maximum frequency the specimens could be cycled at without incurring significant heat build-up as described in Section 3.5. The strain was measured using an optical extensometer in the quasi-static stress-

strain tests. In the case of the fatigue tests, they were carried out under load control and the resultant displacement was determined from the displacement of the hydraulic actuator, as described in Section 3.6

Cylindrical Compression Samples

A series of compression tests were carried out on cylindrical samples that were prepared from 10mm plates, measuring 20mm in diameter, which were then cycled at 10mm/min to 30% compression. A comparison was made between the cylindrical compression tests in order to evaluate whether the compression cycles on the dumbbell specimen yielded results that were close to results from uniaxial compression tests. Hence, it was established that there was not significant influence from barrelling which may cause the prediction of higher stresses. The cylindrical tests took place under three different conditions: lubricated, bonded and layered. The lubricated sample tests were simply where the specimen was placed between the compression plates, which were lightly lubricated in order to eliminate friction between the plates and the specimen. This also helped to eliminate significant barrelling. For the bonded sample tests, the specimens were adhered to the compression plates so that the barrelling effect was maximised in order to evaluate a worst-case scenario for uniaxial compression. The layered sample test format was where 10mm cylinders were constructed from a series of discs cut from 2mm sheets laid on top of one another and placed between the compression plates. The strain in all cases was measured as the distance moved by the crosshead of the testing machine divided by the original thickness.

Pure Shear Samples

The pure shear technique (normally used for crack growth measurements) as described in Section 3.1.8) in the context of this work was solely used for the experimental verification of FEA simulations in combination with ICP where the specimens were cycled at a feed rate of 20mm/min. The specimens were modified by the introduction of holes or cuts in order to introduce stress concentrations, which would in turn induce large strain gradients when the specimen was deformed. The strain was measured using an optical extensometer.

Equi-Biaxial Samples

The equi-biaxial specimens as described in Section 3.1.4 (illustrated in Figure 3.4) were clamped in a stretch frame device. The initial vertical distance between the clamps was 150mm, so under cyclic loading the specimen was cycled at a feed rate of 150mm/min. The strain was measured using an optical extensometer.

Double Shear Sandwich Samples

The experiment using a double shear sandwich sample is a simplified variation of that described in ISO 1827, used to determine the modulus of the elastomeric materials in shear at a feed rate of 2mm/min.

Test Programme

Table 3-5 below gives a summary of the experiments that were carried out in order to characterise the range of materials in the research programme and the

maximum strains that were achieved to allow determination of the first strain invariant I_1 for subsequent use in FEA simulation and in determining an algorithm to model stress softening in successive stress cycles.

I_1	**Dumbbell** Tension	**S2** Tension	**Dumbbell** Compression	**Cylinder** Compression Lubricated	**Cylinder** Compression Glued	**Cylinder** Compression Layered	**Equi-Biaxial**	**Double Shear Sandwich**
3.046			**-11.5%**	**-11.5%**	**-11.5%**	**-11.5%**		**20.8%**
3.163	**25%**	**25%**	**-24.4%**	**-24.4%**	**-24.4%**	**-24.4%**	**12.8%**	**40.3%**
3.347	**37.6%**	**37.6%**	**-30%**	**-30%**	**-30%**	**-30%**	**19.5%**	**58.9%**
3.871	**62.5%**	**62.5%**		**-43.7%**	**-43.7%**	**-43.7%**	**33.3%**	**93.4%**
5	**100%**	**100%**					**54.4%**	
7.05	**150%**	**150%**					**86.7%**	

Table 3-5: Test Programme for material characterisation.

3.5 Investigation of Heat Build-Up

In order to determine the effect of load and frequency on the temperature increase in the samples during fatigue to failure tests, a short study was carried out. EPDM and NR dumbbells were clamped in the MTS elastomer system and cycled at different frequencies and under different loading conditions. The investigation was conducted using a technique known as short wave thermography. The measurement system used was a VarioTHERM^{TM} infrared system as supplied by Jenoptic GmbH **[29]** and the test set-up is depicted in Figure 3.10.

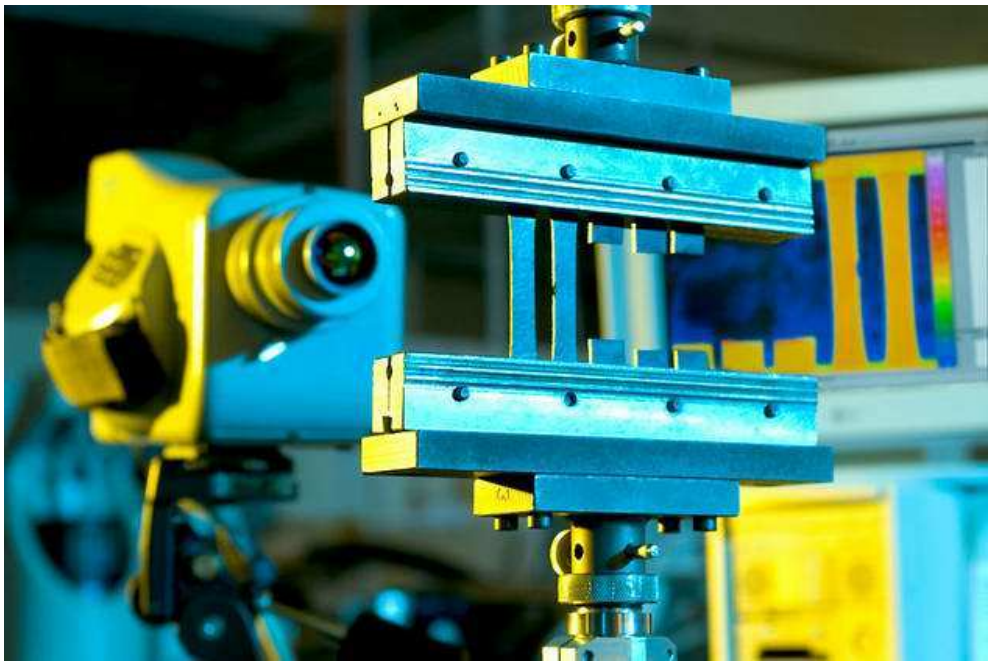

Figure 3.10: The shortwave thermography system set up to measure temperature rise at cracks in elastomer specimens under large deformations.

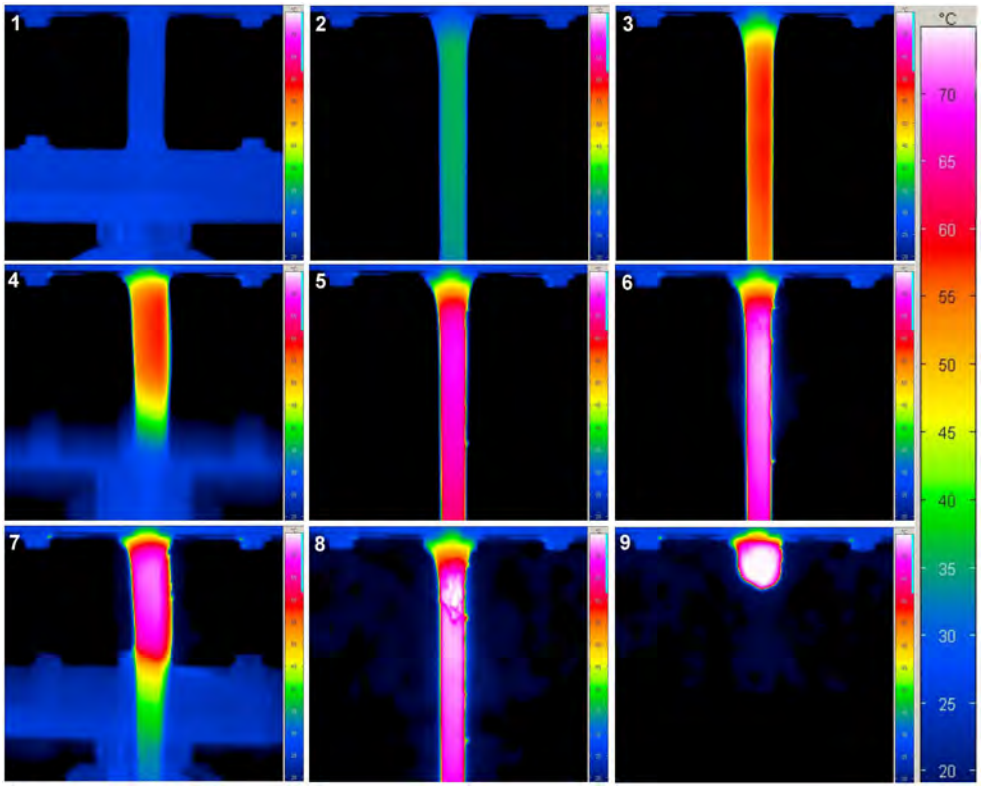

Figure 3.11: Thermal images of a dumbbell specimen being cycled to failure at 350N±300N (load control) at 1.5 Hz.

The temperature was measured by positioning the camera in front of the test specimen and a steel plate which had been cooled in a freezer to -5°C was placed in the background to provide good contrast for the images. Though the camera had the capacity to record images at a rate of 50 per second, it was used in these tests to record an image once every ten seconds. The system was not triggered by the MTS so the specimen was recorded in different positions each time. Using the evaluation software IRBIS Plus V2.2, **[39]** an area of interest could be specified for the entire range of images and from this area of interest it was possible to plot a graph of the minimum, average and maximum temperatures reached on the surface of the specimen versus time. This data was then exported in ASCII (*.asc) format to enable direct comparison with the data measured by the MTS. Figure 3.11 shows a selection of images taken by the system over intervals during a fatigue to failure test on a natural rubber dumbbell sample, under non-relaxing sinusoidal loading of 350N±300N at a frequency of 1.5 Hz until failure. Figure 3.12 shows the hysteresis data recorded by the MTS for the full duration of the experiment. It shows how the specimen's properties changed over the duration of the controlled load cycles and how the permanent set increased as the test progressed. Observations taken from the selection of the series of photographs, show that the temperature of the test specimen increased from room temperature to a maximum temperature of 77°C at close to the point of failure. Also it is apparent that there are temperature irregularities which occur during crack initiation prior to catastrophic failure. Considering the graph in Figure 3.13, obtained from the series of thermography images for the entire test, it was noted that the temperature of the specimen fluctuated within a temperature

range depending on whether the specimen was at the minimum load position (lower temperature) or at the maximum loading position (higher temperature).

A phenomenon termed "drag cooling**" [40]** was observed throughout the tests. During the experiments, the maximum temperature was observed to consistently occur in the uppermost region of the elastomer specimen. This was due to the fact that the specimen was fixed at the top and the lower part was clamped to the hydraulic actuator, so that the lower part of the test-piece was displaced throughout the test. Hence the surface of the specimen in this region was being cooled by a few degrees as a result of its movement through air while the upper portion of the specimen was stationary. This accounts for the temperature difference across the specimen.

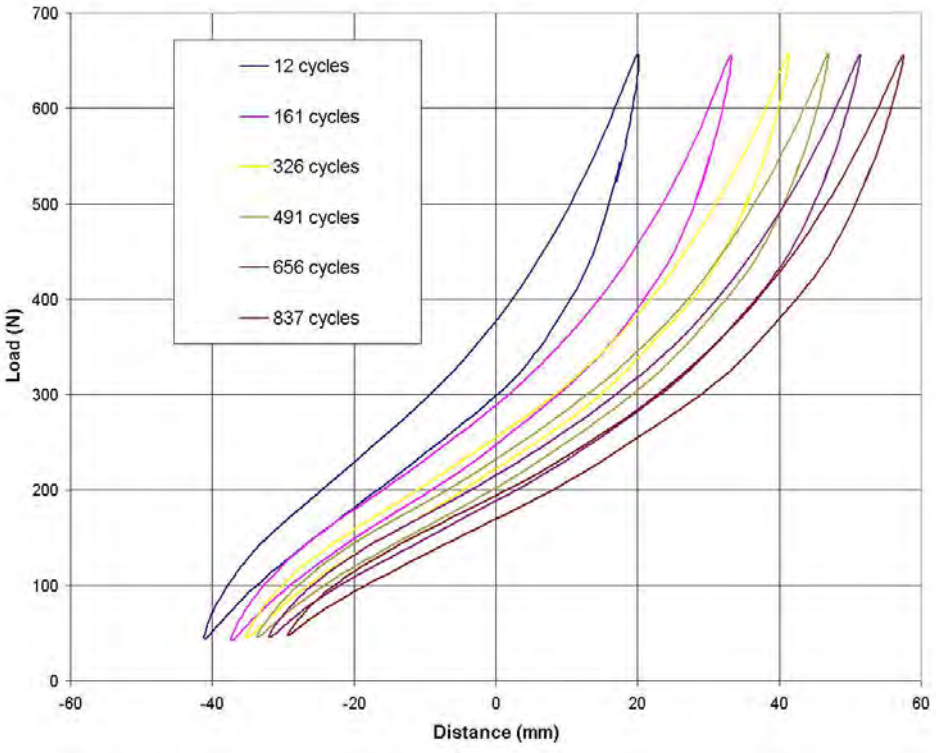

Figure 3.12: Hysteresis for the filled NR specimen during a fatigue to failure test.

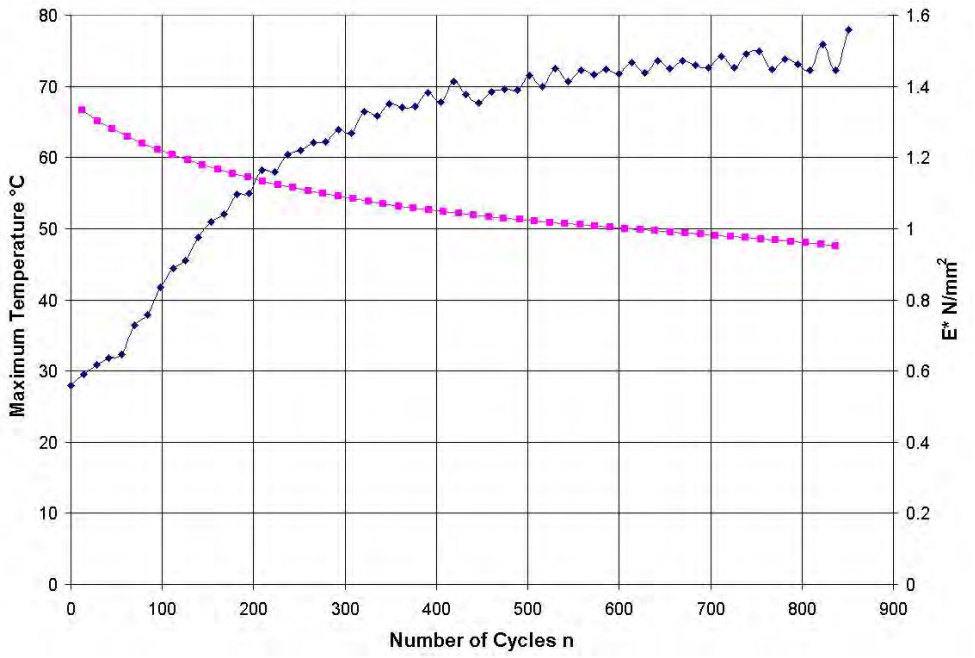

Figure 3.13: Graph of maximum temperature[1] and change in modulus[2] of NR dumbbell in tests to failure. [1]Measured by thermography, [2]Measured by the MTS.

For the frequency study, samples were cycled at 125N±125N at 0.25Hz, 1Hz, 2Hz and 3Hz. Subsequent tests were carried out at a frequency of 1Hz and the load was incrementally increased. The loading conditions were 100N±100N, 125N±125N, 150N±150N, 200N±200N and 250N±250N. Figure 3.13 shows temperature (°C) verses frequency (Hz) for NR and the EPDM materials. The maximum temperatures displayed on the graph represent the level at which the temperature stabilised during the test.

From Figure 3.14 it is interesting to note the differences between the EPDM and NR materials. At a frequency of 1Hz it can be seen that the NR material experienced higher temperature increases than the EPDM for the same loading conditions.

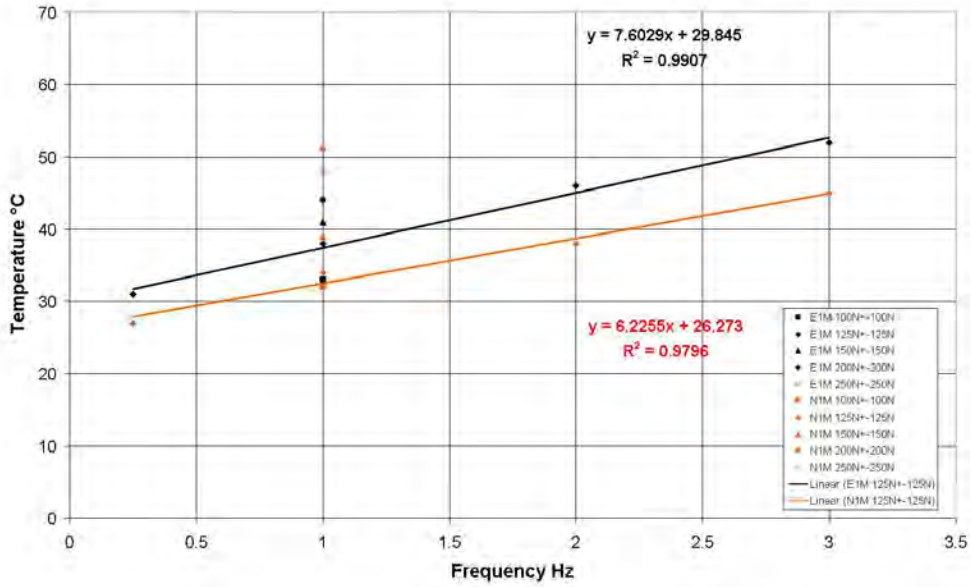

Figure 3.14: Graph of E1M and N1M materials showing variation of temperature versus frequency for the load range employed.

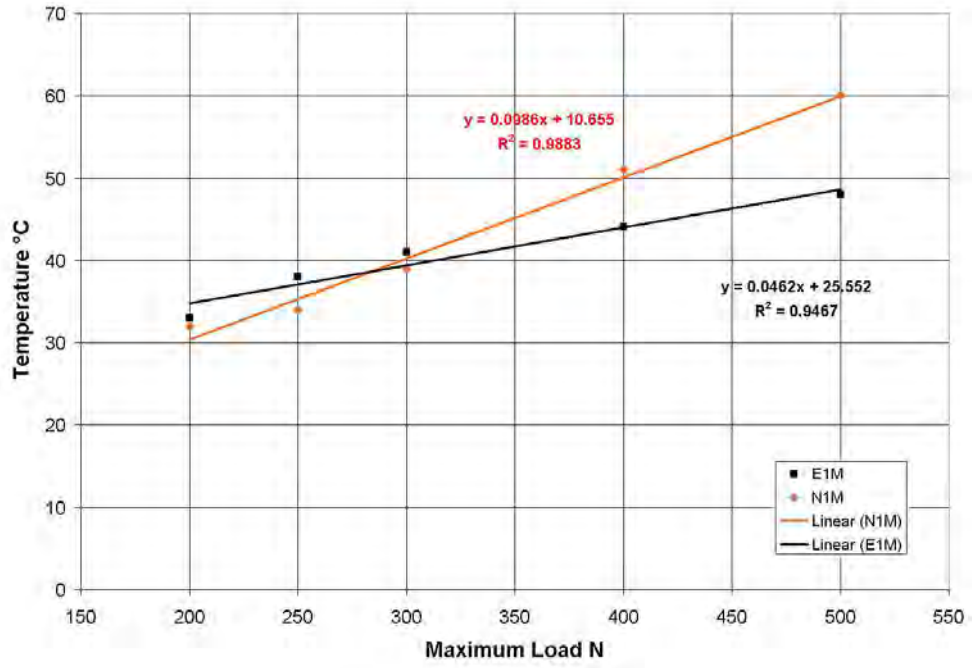

Figure 3.15: Graph of Temperature versus Maximum applied load at 1 Hz.

However as the frequency was increased, the EPDM material experienced temperature rises at a higher rate than those of the NR material. When Figure 3.15 is examined however, the influence of the maximum load on the

temperature reached during cyclic loading at 1Hz only can be seen. It is important to note that when the results for both materials are plotted there was a cross-over point for the behaviour of the two materials. At lower loads in the region of 200N to 300N, the NR material generated a lower surface temperature, but as the load increased, the maximum temperature reached increased at a higher rate than that of the EPDM. At loads of 300N and above the EPDM generates a much lower surface temperature and the rate of increase was lower than that of the NR material. The thermal behaviour of the two materials is thus complex in that it is not only load dependent, but also frequency dependent and EPDM's superior elevated temperature performance is substantiated.

From the study of the thermal effects of both varying load and frequency for both materials it was decided that the tests should be carried out at 1Hz to avoid excessive heat build-up. This frequency was chosen to bring about failure due to the physical induction and growth of cracks only, as opposed to internal friction which would cause large increases in temperature and consequently chemically motivated thermal breakdown of the elastomer specimen **[41]**. This frequency also gave a satisfactory compromise between keeping heat build-up in the specimen to a minimum and of keeping the duration of the fatigue to failure experiments within reasonable time limits. Obviously, while a fatigue to failure experiment conducted at 0.25Hz would have less heat build-up than one conducted at 1Hz, it would last considerably longer, making the accumulation of sufficient data unfeasible.

3.6 Dynamic Testing to Failure of Un-Notched Specimens

This work is predominately concerned with understanding and modelling localised stress softening. An insight into stress softening in rubber-like materials was initially obtained from a series of fatigue tests on the two model materials EPDM material E 1M and NR material N 1M, (refer to Chapter 5). The load ranges in Table 3-6 were used in these tests.

	Load Range	Load Amplitude	Load State
1	100 ± 100 N	200 N	0 N minimum load
2	125 ± 125 N	250 N	0 N minimum load
3	150 ± 150 N	300 N	0 N minimum load
4	200 ± 200 N	400 N	0 N minimum load
5	250 ± 250 N	500 N	0 N minimum load
6	300 ± 300 N	600 N	0 N minimum load
7	200 ± 150 N	300 N	50 N minimum load
8	250 ± 150 N	300 N	100 N minimum load
9	300 ± 250 N	500 N	50 N minimum load
10	350 ± 250 N	500 N	100 N minimum load

Table 3-6: Load Ranges used for fatigue to failure tests.

A typical curve showing modulus falling with repeated cycles is shown in Figure 5.1. A simple semi-empirical formula relating complex modulus to stress cycles for any point in the curve prior to the on-set of catastrophic failure was obtained from fitting a logarithmic curve to the stress data. A simple but feasible method of predicting stress softening during dynamic testing resulted. The complex modulus E* at any point in a test could be represented by equation 3-7

$$E^* = [A\ R^{-1} - B]\ \mathrm{Ln}\ (n) + E \qquad \text{Eqn. 3-7}$$

Where R is the load range (N).

n is the number of cycles at the point under consideration.

A, **B** and **E** are material constants. (E is the initial elastic modulus of the material).

	E1 M	**N1 M**
A (N^2/m^2 $x10^6$)	11.148	20.396
B (MPa)	-0.076	-0.1001
E (MPa)	1.48	1.24

Table 3-7: E and empirically derived constants for predicting complex modulus.

Fatigue tests were carried out on the MTS elastomer testing system described earlier. The tests were conducted at frequencies between 1 and 2 Hz as the frequency study in Figure 3.14 shows that the increase in frequency for relatively low loads did not result in a significant increase in temperature in the specimen during testing.

3.7 Fatigue Testing of Notched Specimens

The procedure for testing of the notched dumbbells was the same as for the plain dumbbell specimens, however frequencies not exceeding 1Hz were used to avoid the influences of thermal build-up on the experimental results. This was more likely to happen in these tests than others due to the smaller cross sectional areas of the notched specimens.

3.8 Low Cycle Dynamic Testing Employing Photogrammetry

3.8.1 Description and Working Principles

Photogrammetry is defined as the process of deriving contour and dimensional information about an object from photographs taken of the object. **[42]** This is

carried out by establishing the geometric relationship between the image and the object concurrent with image capture. Once this has been established, geometrical information on the object can be derived solely from the imagery.

To measure 3D deformation and strain, the object to be loaded during experimentation is viewed by a pair of high resolution (1280 x 1024, 12 bit) digital charged couple device (CCD) cameras, capable of capturing images at rates up to 20 Hz.

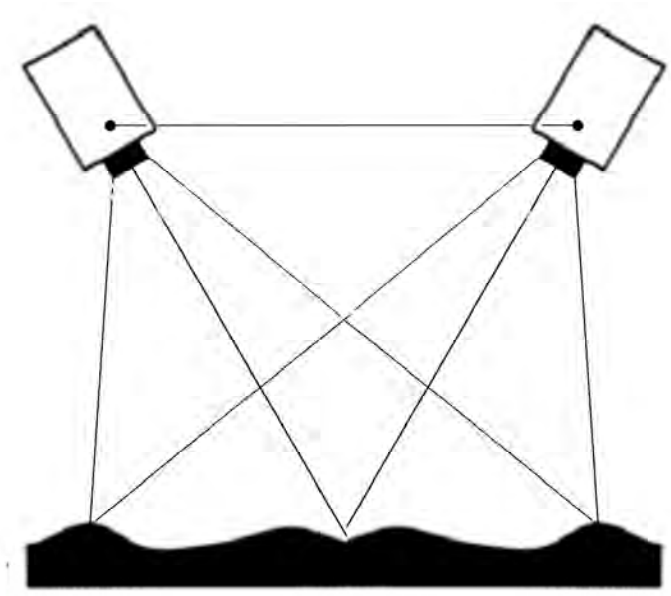

Figure 3.16: Schematic drawing of the optical arrangement for photogrammetry [1]

3D ICP technology is a unique combination of two-camera image correlation and photogrammetry. The photogrammetric set-up used in these experiments consists of the two cameras and a loading device linked to a computer. The loading device chosen to hold and apply a force to the specimen is dependent on the test machine used. The paths between the recording devices and the surface will form a triangle. A line between the cameras constitutes the base of the triangle. Figure 3.16 shows a schematic drawing of the optical arrangement.

3.8.2 Displacement Determination

Calculation of the object co-ordinates for each deformation state for each point P allows the determination of displacements. Here it is important that the point P with the co-ordinates (X; Y; Z) in the non-deformed state can be found in each deformed state with new co-ordinates of (Xt; Yt; Zt). This allows the displacement and strain to be calculated for the object point. The calculation of homologous image points of two deformation states recognised from two cameras can be achieved by a combination of three 2D displacement calculation processes. Here it is important that one image is denoted as the reference state. After determining all 2D displacements, the homologous image points can be easily calculated. With this information, the object co-ordinates for each state can be calculated by space intersection.

After the determination of the displacement, the strain distribution can be calculated using numerical methods. One way to calculate the surface strain is through the transformation of the 3D displacement distribution into a 2D displacement distribution. This permits the strain to be calculated from a linear deformation shown in two-dimensional space **[1].**

3.8.3 Illumination

The 3D image correlation system, based on photogrammetry, used ordinary light, rather than coherent laser light. Lighting was critical to minimise glare. Diffuse illumination can also be used to reduce glare as seen in Figure 3.17. In some high strain cases, only black or white speckles were applied to the specimen (without a matt base) and a high-angle axial illumination was used to prevent glare.

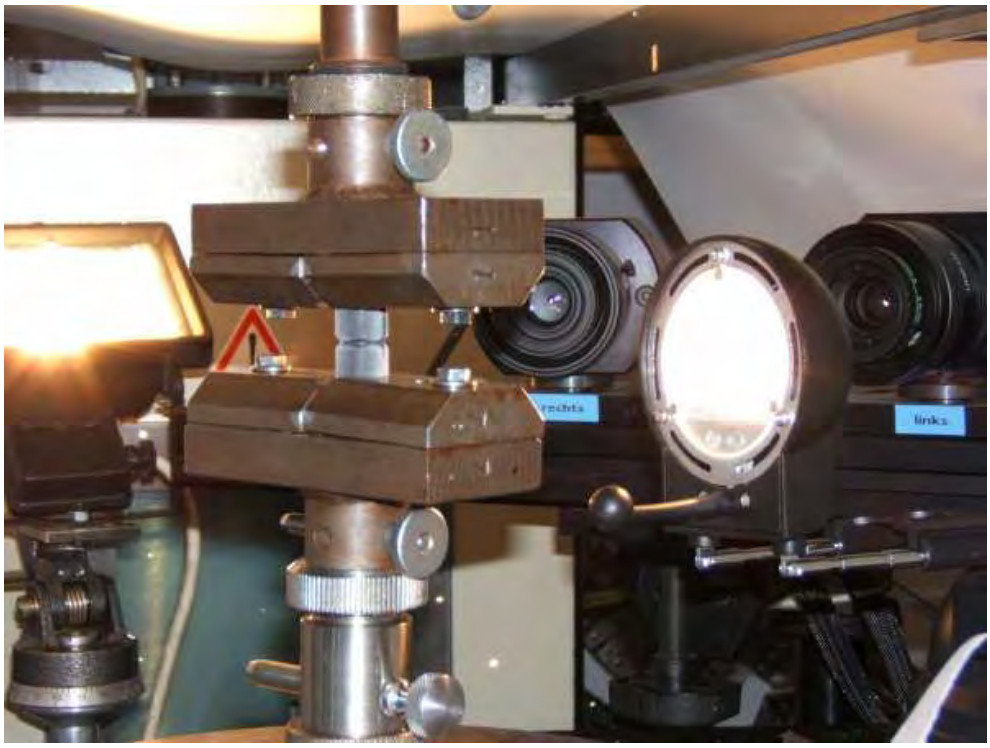

Figure 3.17: ICP experimental setup using illumination being diffused via a reflector onto the notched dumbbell.

3.8.4 Calibration

For system calibration, a special calibration object is needed that has small circular targets with accurately known diameters attached to the surface. During the calibration process, the calibration object must be recognised by the two cameras from several views as shown in Figure 3.18.

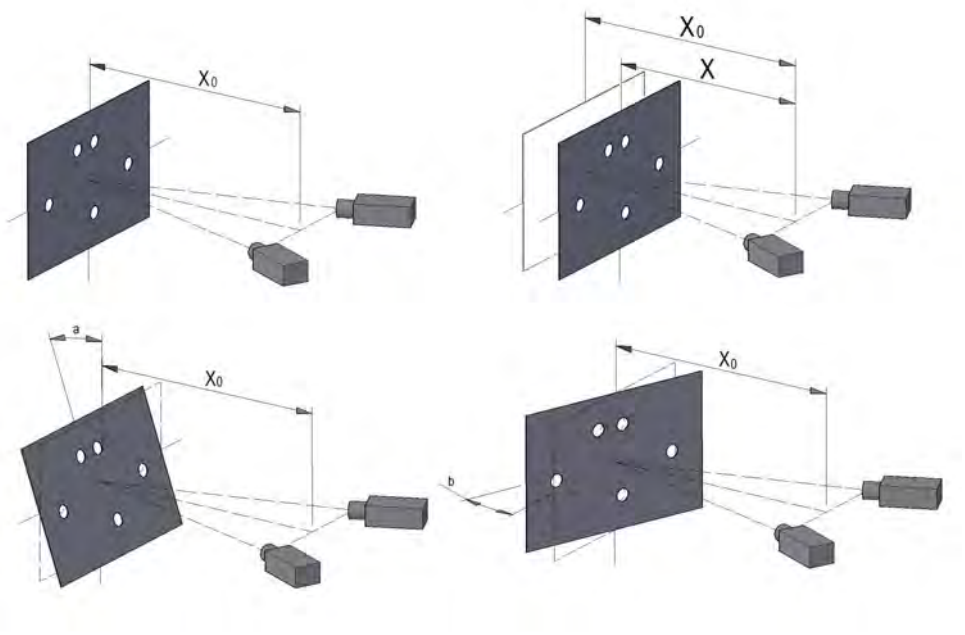

Figure 3.18: Calibration in progress with special calibration piece.

3.8.5 Sample Preparation

A random or regular fine pattern, with good contrast and which deforms along with the object, must be applied to the surface of the test object. The easily applied pattern consists of two layers. The first layer is white dye penetrate developer. This coating, applied using an aerosol, helps to eliminate glare or decrease reflectivity and is easily removed. This is followed by the application of a black spray paint sputtered with about 50% surface coverage as shown in Figure 3.19. A fine and uniform application of this spray allows for a very high local resolution. With the appropriate calculation methods, the resolution can be increased to within sub-pixel range. This method of specimen preparation and application was found to be superior to the use of a stamp to print a grid onto the surface of the specimen, as the aerosol allowed a finer pattern which in turn facilitated a higher resolution of strain measurement.

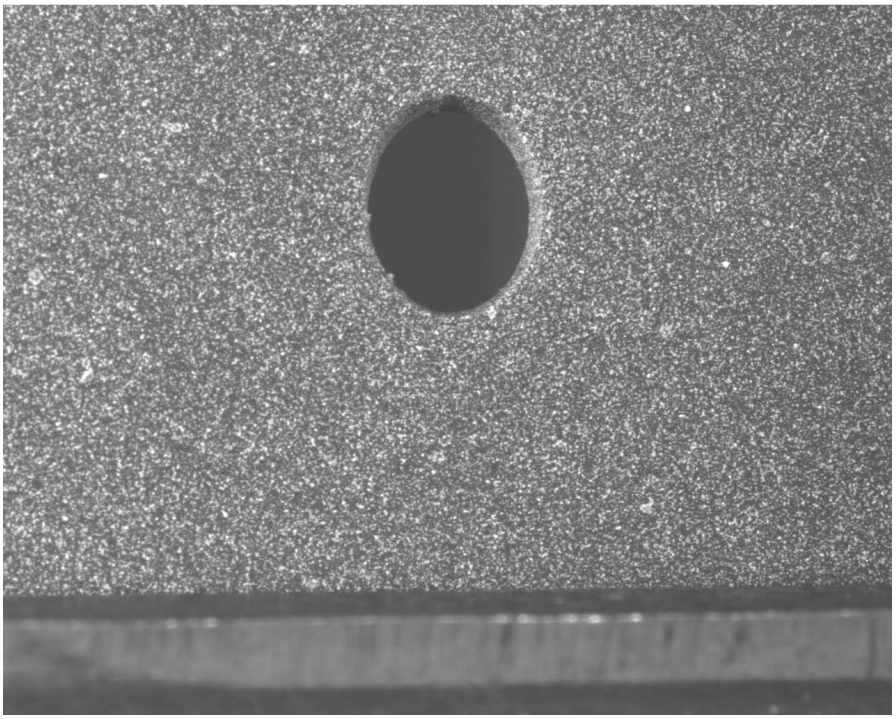

Figure 3.19: A well prepared specimen with good contrast.

3.8.6 Measurement and Processing

The deformation of the object under different load conditions was recorded by the CCD cameras and evaluated automatically by the software. The system tracked the pattern applied to the measurement surface with micron level accuracy. This meant that as long as the object remained within the field of view of the cameras, all of the local deformations were tracked **[43].** Thus, large deformations were analysed in a single measurement. In fact, measurements can be completed after a part has been removed, processed and replaced within the camera viewing zone. In Figure 3.20 each point visible on the specimen is the centre point of an individual facet.

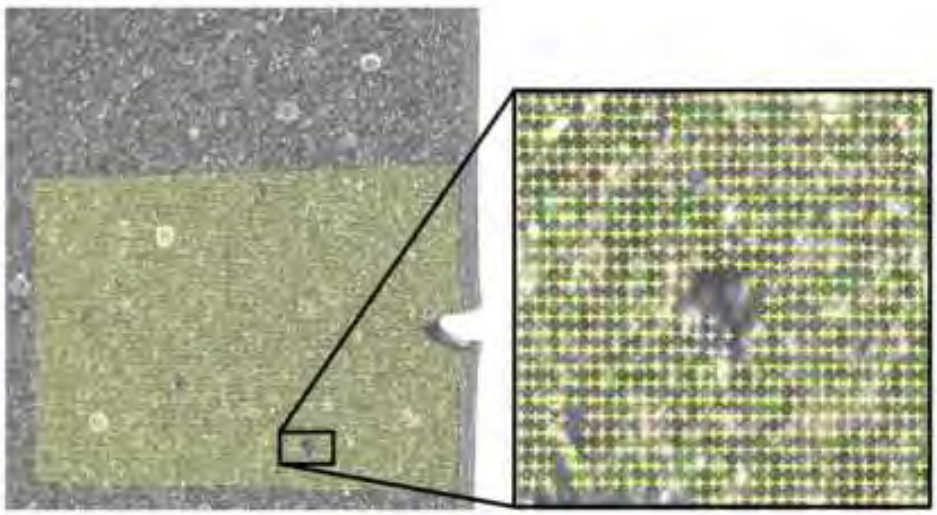

Figure 3.20: A single edge notched specimen (SEN) with sputtering. The cut away view illustrates the problems associated with a lack of contrast within the facets.

The initial image processing, requiring image correlation, defines unique correlation areas known as macro-image facets, typically 5-20 pixels square which can overlap for higher accuracy **[28]** across the entire imaging area. The centre of each facet is a measurement point as shown in the Figure 3.20. These facets are tracked in each successive image (with sub-pixel accuracy). Then, using photogrammetric principles **[42]**, the precise 3D co-ordinates of the entire surface of the specimen are accurately calculated. The results were the determined 3D contour of the component as it was deformed, the 3D displacements and the plane strain tensor.

3.8.7 Accuracy

The minimum sensitivity using 3D image correlation was 1/30,000 of the field of view. For example, with a 3cm field of view, sensitivity is 1μm and with a 30cm field of view, it is 10μm. Fields of view up to several metres square are not difficult to assimilate as long as deformations of several tens of microns are

present **[44].** The system intrinsically measures 3D shapes and therefore 3D deformations are measured simultaneously, rather than sequentially. This significantly improves robustness and accuracy. Furthermore, the use of pulsed high intensity illumination can facilitate dynamic deformation analysis. Complete 3D deformation measurements can occur at up to 20 Hz, while higher speed cameras are also available.

3.8.8 Tests on Single Edge Notched (SEN) Specimens

The first attempts at measuring localised strains at the crack tip used SEN specimens measuring 65 x 15 x 2mm, for various cut lengths ranging from 1mm to 5mm introduced as sharp razor cuts. The samples, made from a carbon filled natural rubber, were clamped in the MTS servo hydraulic Elastomer Testing System (MTS 831.50) fitted with a temperature chamber **[45]**. Unsatisfactory outcomes for the quasi-static testing resulted from a number of problems ranging from poor illumination to glare and reflection from the specimen and inadequate application of the pattern using an aerosol spray as depicted in Figure 3.18.

These shortcomings were taken into consideration and the tests were carried out again with necessary modifications including the use of two 500W halogen lights (see Figure 3.17) and improved pattern application techniques still using aerosol sprays, as explained in Section 3.8.5. Far better results were achieved. It proved possible to measure deformations and calculate strain throughout the entire experiment, across the full range of materials and test conditions. However the use of the two 500W lights generated considerable heat, so long-term exposure of the sample to the illumination sources was avoided to keep the temperature as

close to room temperature as possible and thus avoid inconsistencies in material properties.

3.8.9 Variation of the Facet Size and Step for SEN Specimens

Using the ICP system, a study of the effects of the variation of the facet size and step on the resulting calculated strain for the measurement was carried out. Comparisons were made using the same series of images of a 15% integral strain but varying facet size and facet step to achieve different results.

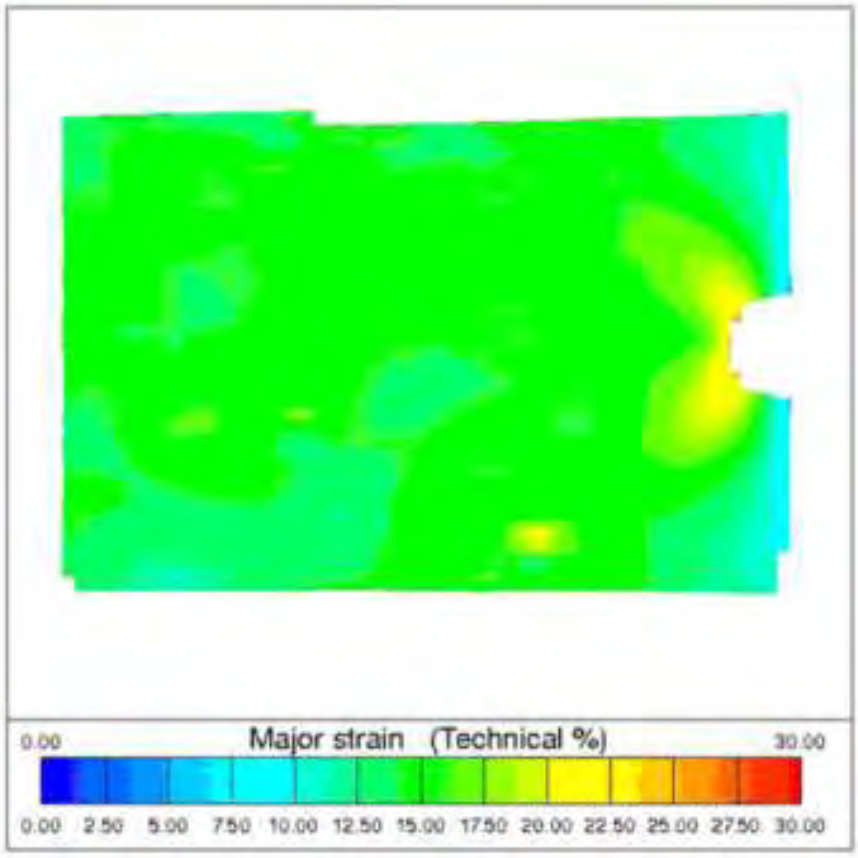

Figure 3.21: ICP measurement of an SEN specimen with a 1mm crack at 15% integral strain. Facet size of 21, facet step of 15. Max local strain 26%

Figure 3.21 shows an SEN specimen subjected to an integral strain of 15%. The facet size was 21 and the facet step was 15. From the measurement it can be seen that a maximum local strain of 26% was determined at the crack tip and that

when compared with the photograph of the specimen illustrated in Figure 3.22, the crack profile does not accurately represent that of the original cut. However from Figure 3.22 it can be seen that the smaller the facet step (the smaller the distance between the centre points of neighbouring facets) the higher the maximum local strain obtained and the more accurate the result. In this case, a facet size of 15 and a facet step of 6 were applied. Due to this reduction in the step, the local resolution was increased and it was possible to measure closer to the crack tip. Thus a higher maximum local strain of 30% was obtained.

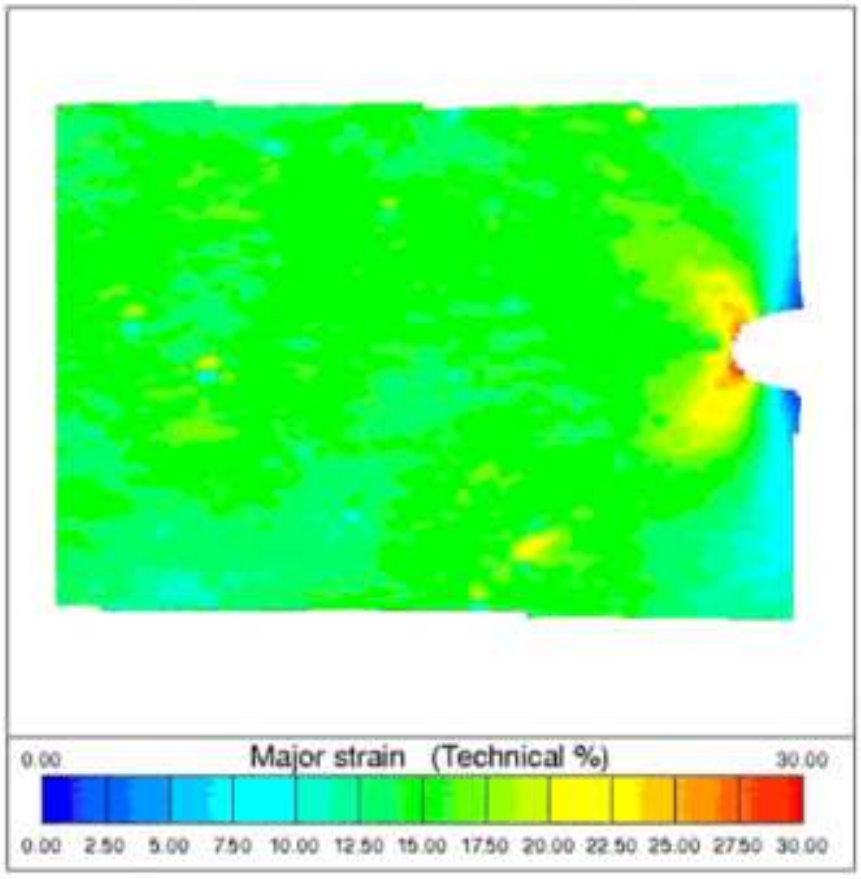

Figure 3.22: ICP measurement of an SEN specimen with a 1mm crack at 15% integral strain. Facet size of 15, facet step of 6. Max local strain 30%.

Conversely, there was a large increase in the time taken to carry out the calculations. Through experimentation it was shown that optimising the

resolution by reducing the facet size was limited by the contrast of the pattern within a facet (i.e. 50% black, 50% white). Adjusting the facet overlap provided a far superior method of improving the local resolution.

3.8.10 Variation of Initial Crack Length

For a series of ICP measurements, Figure 3.23 illustrates how the localised strains at the crack tip increased for greater crack lengths in each SEN specimen subjected to the same integral strain increase. All specimens were subjected to integral strains of 15%, however the maximum localised strain obtained in the case of the 1mm initial crack was 30%, compared with 58% for the specimen with the 4mm crack and 68% for the specimen with the 5mm crack as shown in Figure 3.23 and Table 3-8.

It should be noted that in the series of measurements depicted in Figure 3.23 each individual measurement was made with a constant facet size of 15 pixels, but all had a different facet step.

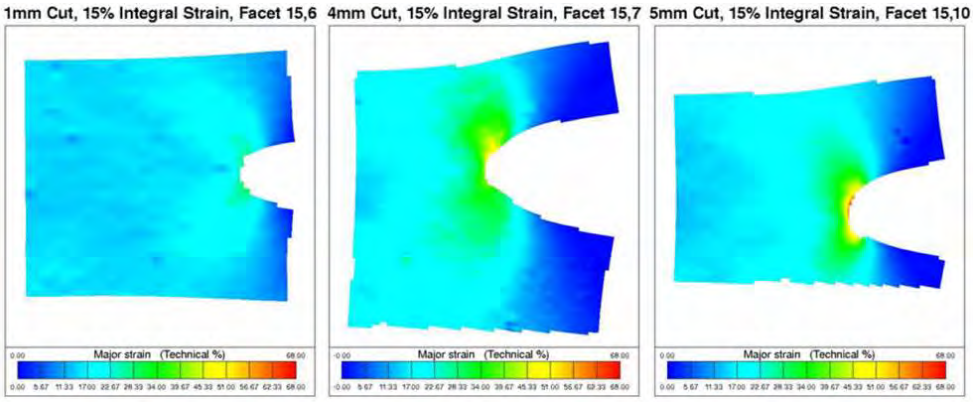

Figure 3.23: ICP measurements showing an increase in maximum local strain obtained with increasing crack length for individual SEN specimens.

The step was increased from 6 pixels for the 1mm crack to 7 pixels for the 4mm crack to 10 pixels for the 5mm crack. Even though the step was increased in

each sample with increase in initial crack size, there was still a pronounced increase in the local maximum strain obtained at the crack tip.

Cut Length (mm)	Facet size (pixels)	Maximum Local Strain (%)
1mm	15	30%
4mm	15	58%
5mm	15	68%

Table 3-8: Increasing maximum strain with increasing crack length on SEN specimen as measured by ICP.

3.9 Finite Element Analysis

The understanding of the behaviour of elastomers has been greatly enhanced by the work of many researchers including Rivlin, Thomas and Yeoh **[15][46] [47]**. Even so, the ability to model and simulate the hyperelastic behaviour of rubber-like materials under various loading and environmental conditions remains imperfect. There is still no universally accepted theory to describe the behaviour of elastomers and other hyperelastic materials. This is not made easier by the fact that the range of elastomeric materials seems to be infinite, with new compounds and different blends continually becoming available. Moreover, the difficulty also remains that the differences in the physical behaviour of elastomeric materials are so vast that no comprehensive database exists for even the simplest constants used to model them. Even the constants (e.g. C_{10}, C_{01}) of the James Green Simpson strain energy density function **[11]** can differ considerably for variations in mechanical properties when rubber is manufactured on an industrial scale and will vary depending on small differences in production from batch to batch, or even on the expertise of the machine

operator. However, the use of two constants is inadequate to accurately simulate the behaviour of the most basic elastomer components subject to complex loading, let alone the typical components that appear in machines and vehicles in everyday use (e.g. the drive shaft boot commented on in Section 1.3) **[48]**. Higher order models are necessary to accurately simulate the real behaviour of components under normal operating conditions. Individual uni- and multi-axial stress-strain tests must be carried out to characterise the materials under different loading modes in order to provide experimental data for fitting the constitutive equations and evaluation of realistic coefficients. Once this is complete, it is important to process the experimental data correctly and consistently before using a fitting procedure which can also have a bearing on the coefficients obtained **[49] [50]**.

Manufacturers in the automotive industry have become more reliant on FEA in the design and manufacture of rubber components. This is driven by the need to quickly solve problems with more complex designs and reduce "over engineering" in order to minimise cost. While doing all this, they will also want to minimise development time and avoid costly recalls of products that could be subject to premature failure.

3.9.1 Comparison of Notched SEN Tests with FEA

The photogrammetry measurements seen in Figure 3.22, depicting a maximum of 30% for an integral strain of 15%, were then compared with FEA. The outcomes did not correlate well with the FE analysis and this can be observed with reference to Figure 3.24 (derived from an analysis of a co-researcher) which reveals much higher localised strain values (125%) than those suggested in Figure 3.24.

This discrepancy would normally be attributed to the very high strain gradient at the crack tip. Due to resolution and optical limitations it was not possible to calculate the strain precisely at the crack tip, but only to within approximately 0.2mm of the free edge. (In photogrammetry a strain value for each facet is calculated at the centre of the facet, which will always set a limitation on the system, dependent on the facet size). However, the high strain predicted by the FEA resulted from an injudicious choice of material model.

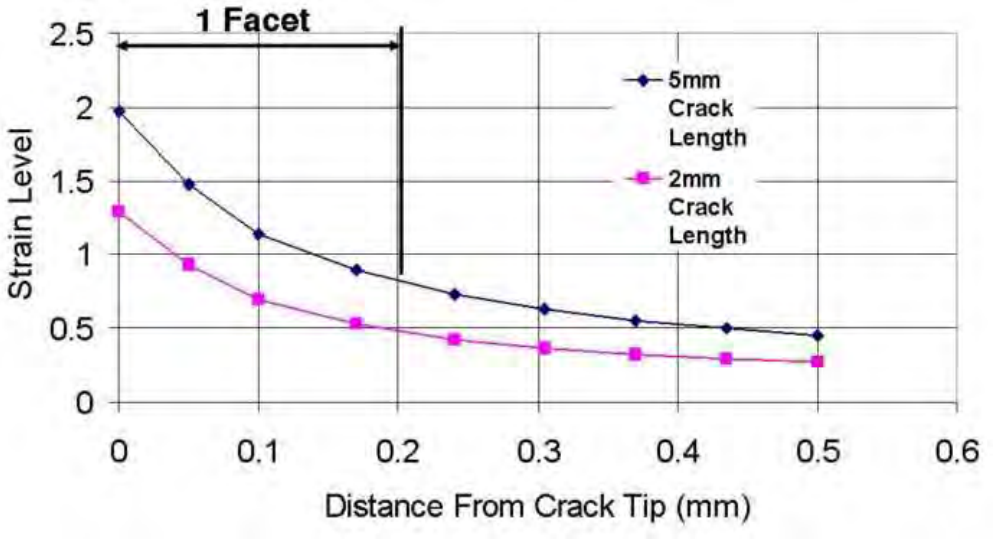

Figure 3.24: Diminution of strain with distance from the Crack Tip at 15% integral strain.

3.9.2 Modified SEN with Central Hole

Experiments were repeated on samples similar to the SEN specimen but with a different stress raiser. This assisted in verifying the methodology and provided insight into stress concentration where less severe discontinuities were employed. The alternative sample, made from a carbon filled NR (measuring 65 x 30 x 2mm), had a 6mm hole punched in the centre of the specimen and values of integral strains ranging from 10% to 50% were determined. Initially the results obtained did not correlate, but this was due to a poorly defined FE model. The

error had resulted from incorrect boundary conditions applied to the simplified model in the FEA simulations. The nodes on the axis of symmetry were defined as encastré but should have been free to move in the horizontal plane. This failing was corrected and thereafter the lower strains of 10% and 20% compared well with the FE simulations. Comparisons were subsequently made for higher strains (Table 3-9). Figure 3.25 shows the elastomer specimen under strain alongside the corresponding FEA simulation. Further examples are shown in Appendix 5.

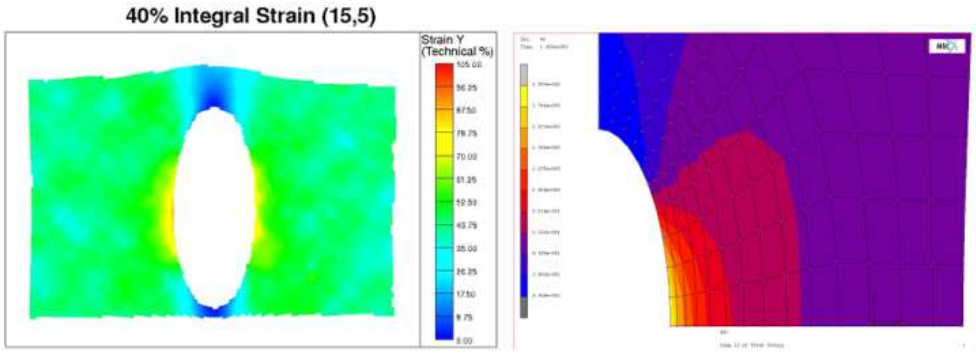

Figure 3.25: ICP measurement and FEA calculated strains for specimen at 40% integral strain.

Integral Strain	ICP	FEA
10%	30%	31%
20%	55%	66%
30%	75%	94%
40%	98%	119%
50%	105%	132%

Table 3-9: Correlation between ICP and FEA for the hole in planar specimen.

3.9.3 Modified SEN with 90° Vee Notch

Measurements of strains in SEN specimens (sized 15 x 65 x 2mm) carried out on the same carbon filled natural rubber were undertaken with 90° Vee notches of 5mm depth. The Vee notched specimens possessed much larger root radii than the SEN specimens, which were of the order of 0.03mm. Measurements in ICP compared more favourably with FE simulations. Figure 3.26 shows the notched specimen in both the zero and 10% integral strain state. Figure 3.27 and Table 3-10 show the evolution of the local strain in comparison with the FEA simulation. Further examples are shown in Appendix 5.

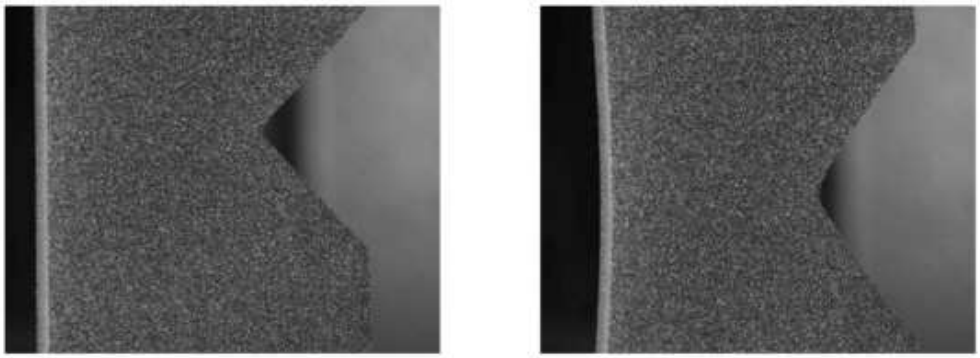

Figure 3.26: Images of the 90° Vee notched specimen at zero at 10% integral strain as measured by the ICP system.

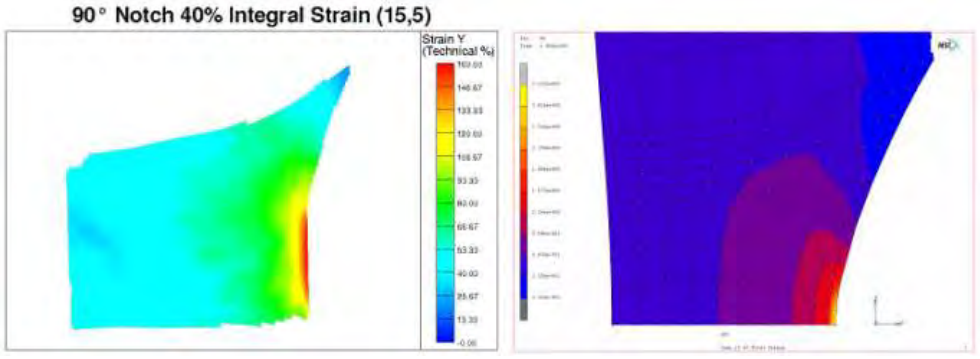

Figure 3.27: ICP measurement and FEA calculated strains for Vee notched specimen (40% integral strain. ICP max value 160%, MARC max value 169%).

Integral Strain	ICP (Strain at notch root)	FEA (Strain at notch root)
10%	58%	67%
20%	115%	123%
30%	140%	148%
40%	160%	169%

Table 3-10: 90° Vee notch specimen ICP compared to FEA (all values in engineering strain).

The values for engineering strain displayed in Table 3-9 are for the root of the notch. It is possible for FEA to predict the strain which is precisely at the notch providing that loads and boundary conditions are correct and the appropriate elements are chosen. However, it is not possible for the ICP system to measure the strain directly at the edge of the specimens, which accounts for the difference in the values obtained at the root for both methods. This is illustrated in Figure 3.28 where the offset from the edge of the specimen is evident between the FEA and ICP. Even so, taking this difference into account, away from the edge of the specimen the differences are very small and show good agreement between the two techniques. When this distance from the centre to the edge of the facet is taken into account (0.2mm) the results from the photogrammetric measurement and FEA are in better correlation. It is possible however to improve the resolution in ICP and measure closer to the crack tip by using longer focal length lenses to examine smaller areas. Also curves for strain for ICP can be extrapolated to allow a reasonable assessment of strain at the notch root.

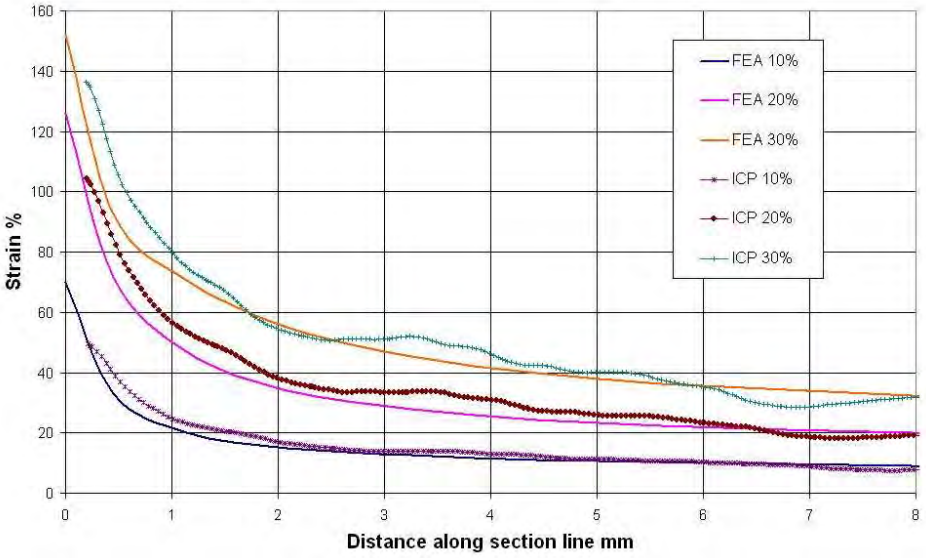

Figure 3.28: Comparison of strain measured using ICP and simulated with FEA for 90° Vee notch specimens.

Chapter 4 Varying Material Constants to Assimilate Stress Softening

4.1 Modifying Local Constants to Facilitate Accurate FEA Simulation

Varying material constants for FEA analysis to model stress softening was introduced by defining local coefficients on the basis of measured changes in strain invariant I_1 for successive load steps

4.1.1 Progressive Updating of FEA Material Constants to Model Stress Softening

In most current FEA codes the material properties defined for a model are assumed to be uniform, representing homogeneity throughout the entire FEA domain. However, this assumption can only be considered valid for the first loading cycle of an elastomeric component or specimen deformation, but not for subsequent cycles or for the rest of the component's life. Similarly, viscoelastic effects will vary throughout a rubber sample subject to cyclical loading due to the specimen geometry (i.e. stress softening at the root of a notch will be greater than that in the body of the specimen). As standard FEA codes do not take actual (time dependent) behaviour into account, it can be assumed that the lifetime predictions for elastomer components are unreliable. In all the simulations, a Yeoh model was used to represent material behaviour since it uses constants C_{10}, C_{20} and C_{30} which are a function of strain invariant I_1. It should be noted that other constitutive equations which use constants that are functions of both strain invariants I_1 and I_2 are more appropriate than the Yeoh model for modelling multi-axial deformations. Yeoh was chosen for this research to prove the concept of varying material constants from test data to allow for the

simulation of viscoelastic effects. The importance of the second strain invariant I_2 is briefly explained in Section 4.1.2.

4.1.2 Finite Element Modelling Requirements, Element Selection and Constraints

4.1.2.1 SEN Specimen with "Sharp 5mm Crack"

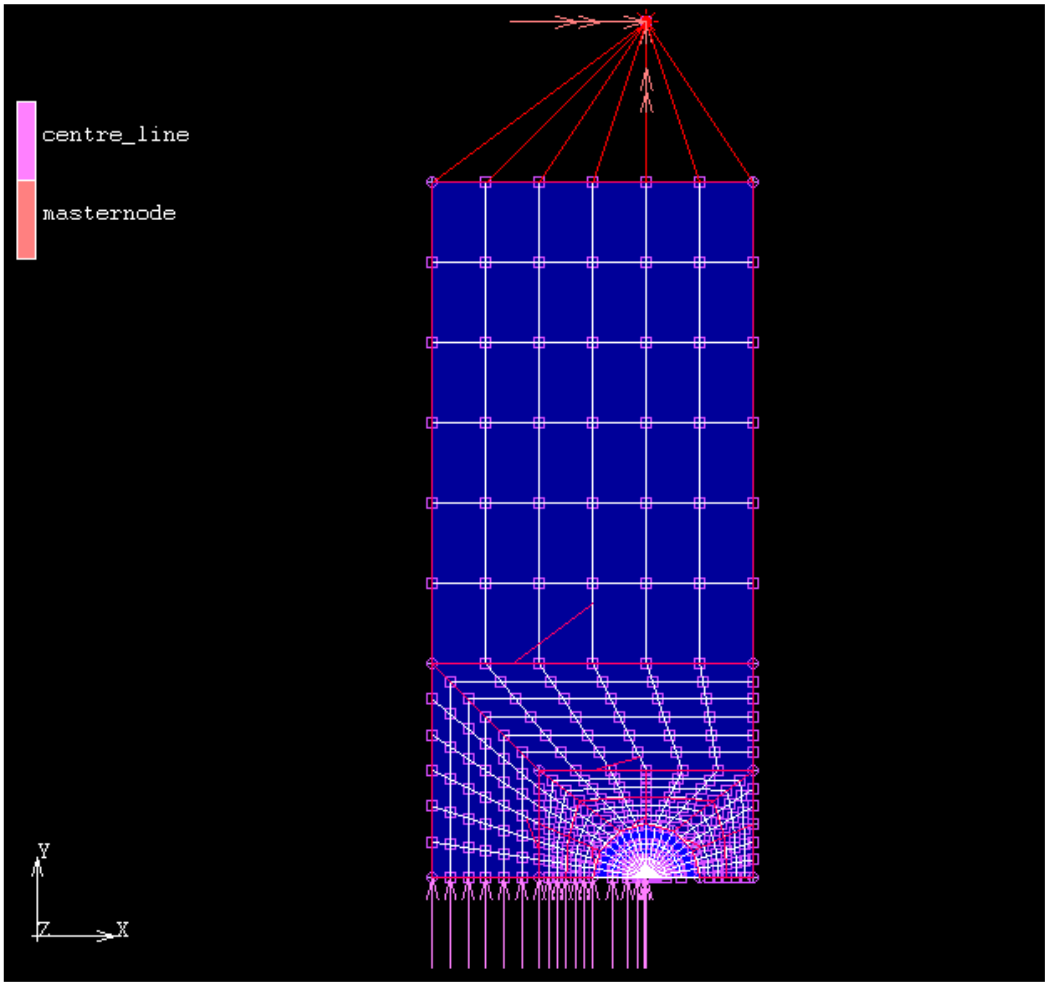

Figure 4.1: Half FEA model of an SEN specimen with a 5mm crack.

The SEN specimen was described previously in Section 3.1.6 and illustrated in Figure 3.5. A slight variation of this model represented a 90º Vee notch specimen (described in Section 3.1.7 and illustrated in Figure 3.5) was modelled as a planar specimen initially of unit thickness, subjected to a uniaxial deformation. It was then possible to simply extrude the model to the desired thickness to make a 3D (or volumetric) model, the only significant difference between the two is the element type. Only one half of the specimen was modelled. This made use of the axis of symmetry about the X-axis on either side of the crack, as illustrated in Figure 4.1. As the geometry can be considered to conform with a thin plate with in-plane loading, the requirements for a plane stress simulation are fulfilled. In the representation, the crack is sharp, hence the radius of the crack is zero. A mapped mesh construction was made with the mesh increasing in density in the vicinity of the crack tip. The material properties were assigned by fitting a nonlinear material model to uniaxial and equi-biaxial experimental data for equal values of the first strain invariant I_1.

Elements Employed

The type of elements used in the SEN model were plane stress, isoparametric and quadrilateral elements, specifically written for plane stress applications. The elements are particularly suitable for modelling incompressible and nearly incompressible materials such as elastomers (the Herrmann Formulation) **[51]**.

Modelling Boundary Conditions

All boundary conditions applied to the SEN model are depicted in Figure 4.1. The bottom nodes along the X-axis are only constrained in the Y direction from the left of the model to the crack tip. This line is also the line of symmetry of the

model. Elsewhere the nodes along the free edge of the crack are unconstrained and free to move in both the X and Y directions.

The nodes at the top of the model are fixed in the X direction and loaded in the Y direction, in order to simulate the effect of the clamps on the specimen. These are coupled to a master node above them with RBE2 elements, which control all displacement. The forces exerted on each top node are transmitted to the master node, which in effect replicates it acting as a load cell would in an experimental setup. This facilitates the display of load deflection curves and makes applying loads and displacements to the model easier.

4.1.2.2 Planar Specimen with 6mm Centrally Located Hole

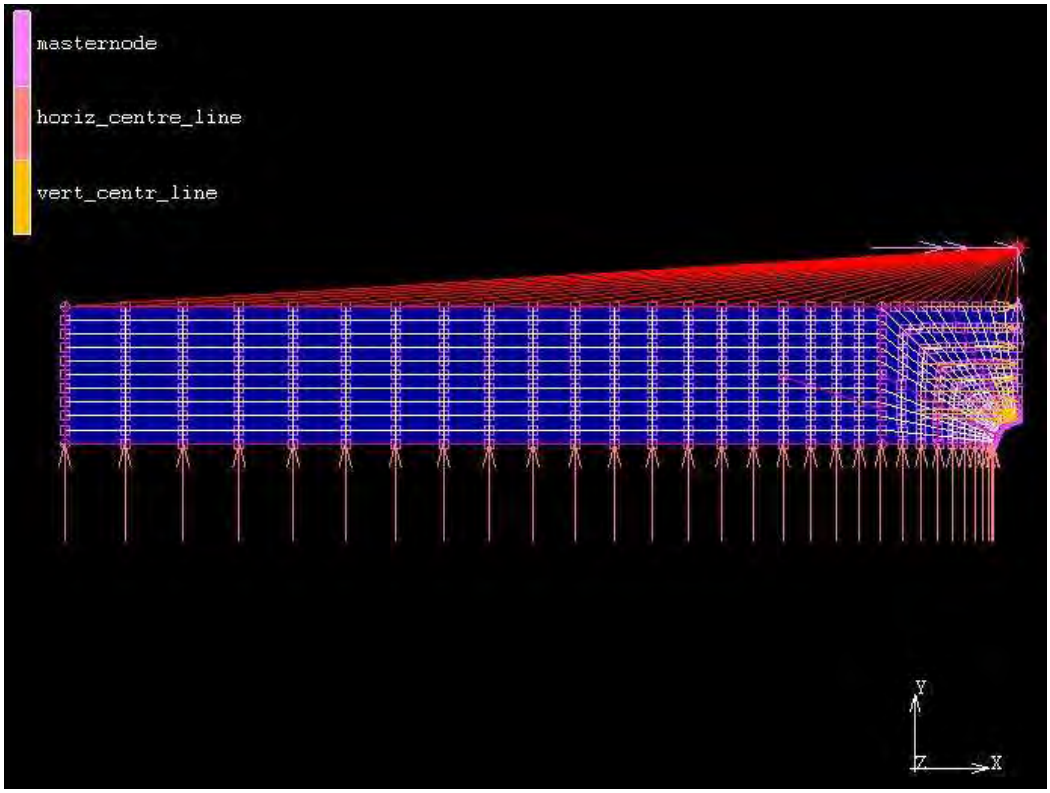

Figure 4.2: : Planar Specimen with a centrally located 6mm diameter hole.

Model Description

The Planar specimen (previously described in Section 3.1.8 and illustrated in Figure 3.6) was modelled with unit thickness and subjected to uniaxial deformation. It was possible to convert this model to a volumetric one simply by extruding it to the desired thickness. The only significant difference between the two models is the element type used. Axes of symmetry along the X and Y-axes from the hole at the centre of the specimen were exploited, as illustrated in Figure 4.2. As the geometry can be considered to be a thin plate loaded subjected to in-plane loading, the assumptions for a plane stress simulation are fulfilled. The hole is of 6mm in diameter. A mapped mesh was employed with the mesh increasing in density in the vicinity of the hole. The material properties were assigned by fitting a nonlinear material model to uniaxial and equi-biaxial experimental data to equal values of the first strain invariant I_1.

Elements Employed

The elements used to simulate the planar specimen with a centrally located hole were plane stress, isoparametric and quadrilateral elements, which are specifically written for plane stress applications. Again the elements are suitable for modelling incompressible and nearly incompressible materials such as elastomers (Herrmann Formulation) **[51]**.

Modelling Boundary Conditions

The nodes at the base of the model are constrained in the Y direction. This represents the horizontal centre line of the specimen. The nodes on the right hand side of the model are constrained in the X direction only as this represents the vertical centre line of the specimen. The nodes along the top of the model

represent where the specimen is clamped, here they are constrained in the X and Y directions and coupled to a master node with RBE2's elements to facilitate load application with Rigid Body Element Type 2 link (RBE2's) These are useful as they allow the Degrees of Freedom (DOF) to be only partially constrained, they can also be used to realistically simulate really rigid connections meaning that the displacement of the nodes is under precise control.

4.1.2.3 Modified SEN with 6mm Central Hole

Model Description

The specimen (previously described in Section 3.9.3 and illustrated in Figure 3.25) was modelled as a planar specimen initially of unit thickness, subjected to a deformation in the Y direction.

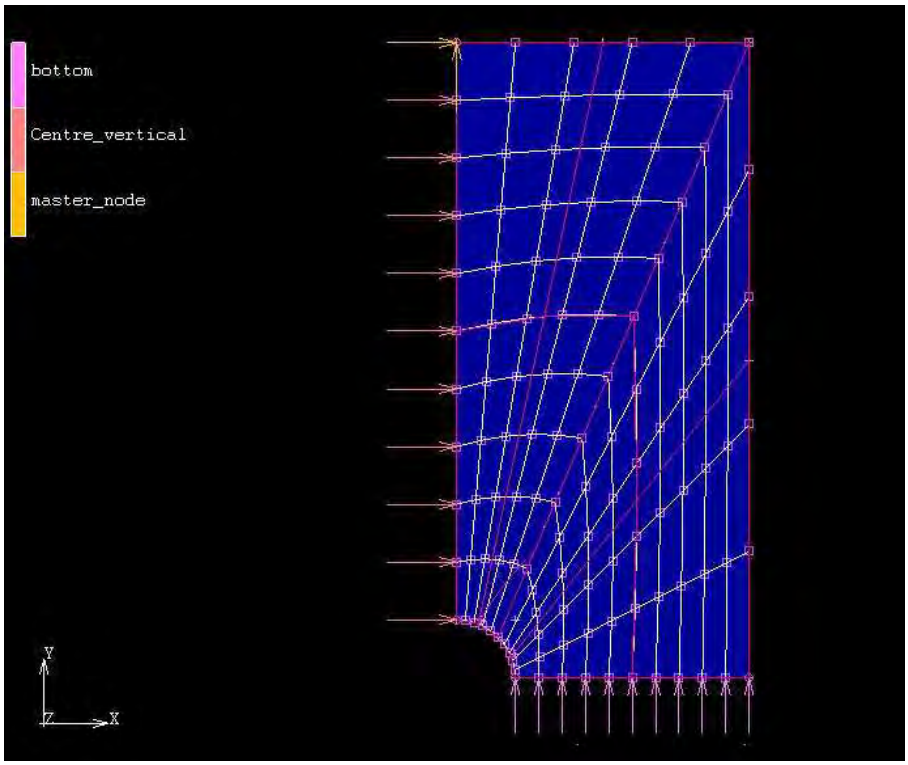

Figure 4.3: Modified SEN model with a 6mm central hole.

It was possible to convert this model to a volumetric one by simply extruding it to the desired thickness. As the geometry can be considered to be a thin plate with in-plane loading, the requirements for a plane stress simulation are fulfilled. The hole is of 6mm in diameter. A mapped mesh was employed with a bias towards mesh density increasing in the vicinity of the hole. The material properties were assigned by fitting a non-linear model to uniaxial and equi-biaxial experimental data to equal values of the first strain invariant I_1.

Elements Employed

The elements used in the simulation were plane stress, isoparametric and quadrilateral elements, which are specifically written for plane stress applications. As previously, the elements are also suitable for modelling incompressible and nearly incompressible materials such as elastomers (Herrmann Formulation) **[51]**.

Modelling Boundary Conditions

The nodes along the base of the model are constrained in the Y direction. This represents the horizontal centre line of the specimen. The nodes on the left hand side of the model are constrained in the X direction only as this represents the vertical centre line of the specimen. The nodes on the top edge of the model represent where the specimen is clamped and are constrained in the X and Y directions and coupled to a master node to facilitate the application of loads using RBE2 elements.

4.1.2.4 Planar Specimen (Pure shear) with 35mm Cut

Model Description

The Planar specimen (previously described in Section 3.1.8 and illustrated in Figure 3.6) was modelled with unit thickness and subjected to a uniaxial deformation in the Y direction. It was possible to convert this model to a volumetric one simply by extruding it to the desired thickness. The only significant difference between the two models is the element type used. The X and Y axes of symmetry from the tip of the 35mm induced crack at the end of the specimen were exploited, as illustrated in Figure 4.2. As the geometry can be considered to be a thin plate with in-plane loading, a plane stress simulation was created. A mapped mesh was employed with the mesh increasing in density in the vicinity of the crack tip. The material properties were assigned by fitting a non-linear material model to uniaxial and equibi-axial experimental data to equal values of the first strain invariant I_1.

Elements Employed

The elements used in the simulation were plane stress, isoparametric and quadrilateral elements, which are specifically written for plane stress applications. The elements are also suitable for modelling incompressible and nearly incompressible materials such as elastomers (Herrmann Formulation) **[51]**.

Modelling Boundary Conditions

The nodes along the base of the model are constrained in the Y direction. This represents the horizontal centre line of the specimen.

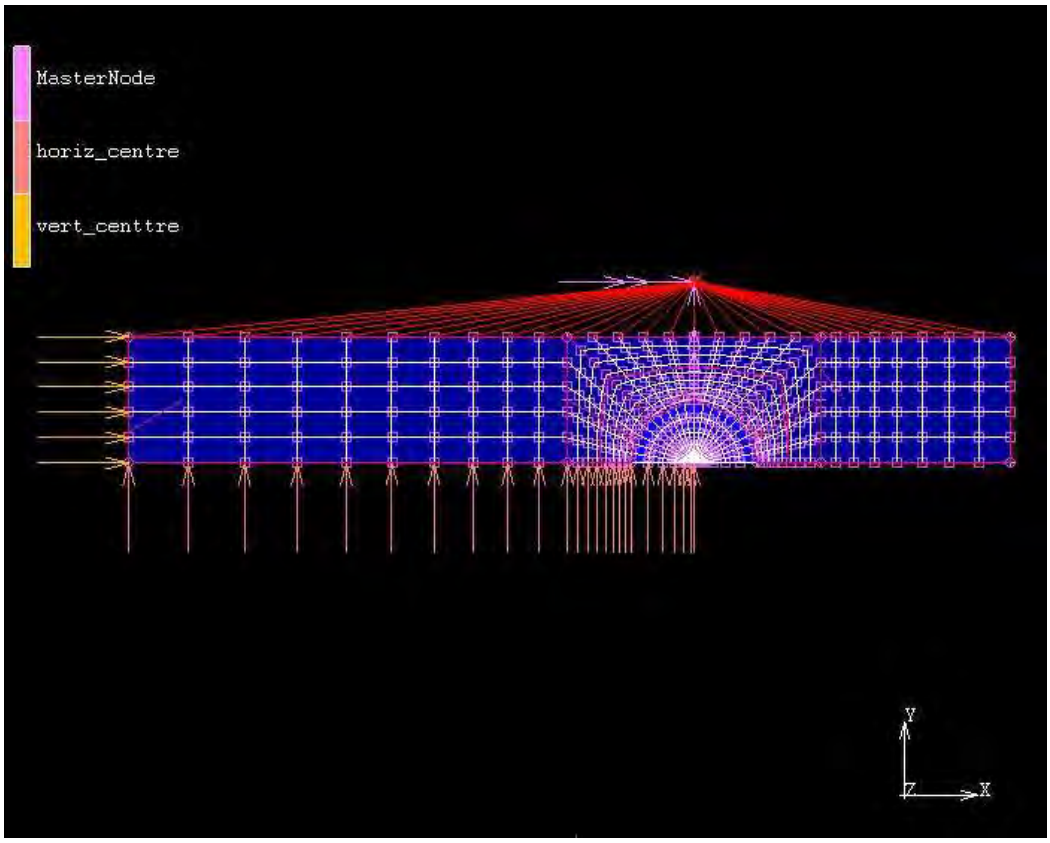

Figure 4.4: Planar specimen (pure shear) with a 35mm crack.

The nodes on the left hand side of the model are constrained in the X direction only as this represents the vertical centre line of the specimen. The nodes on the top edge of the model represent where it is clamped and are constrained in the X and Y directions and coupled to a master node to facilitate the application of loads using RBE2 elements. The nodes on the right-hand side of the model are unconstrained as they represent the free edge of the specimen.

4.1.2.5 Uniaxial S2 Model

Model Description

The S2 specimen (previously described in Section 3.1.1 and illustrated in Figure 3.1) was modelled in 3D by importing a *.dxf format drawing of the specimen in AutoCAD.

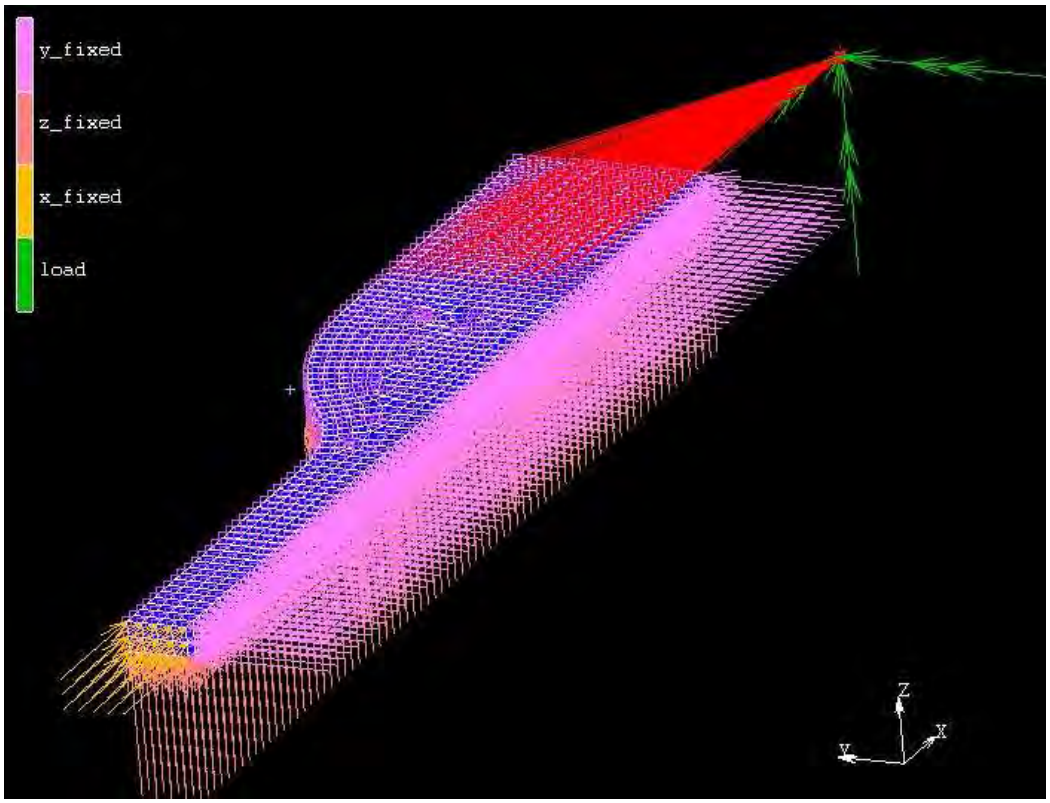

Figure 4.5: Uniaxial S2 model reduced to 1/8th of the original.

It was subjected to a uniaxial deformation in the X direction. To exploit axes of symmetry only one eighth of the specimen was modelled as illustrated in Figure 4.5. A mapped mesh was employed in order to ensure an even mesh for the gauge length of the model. The material properties were assigned in the usual manner employed in DIK, by fitting a non-linear material model to uniaxial and equi-biaxial experimental data to equal values of the first strain invariant I_1. This particular model was used to validate whether the material coefficients determined by the fitting procedure matched the actual experimentation carried out on the Zwick tensile testing machine prior to more complex simulations of actual components manufactured from the material being carried out.

Elements Employed

The elements used in the simulation S2 specimen were eight node, three-dimensional, first-order isoparametric elements. The elements are also suitable for modelling incompressible and nearly incompressible materials such as elastomers (Herrmann Formulation) **[51]**.

Modelling Boundary Conditions

The nodes on the bottom edge of the model are constrained in the X direction. This represents the horizontal centre line of the specimen. The nodes on the right hand side of the model in the X plane are constrained in the Y direction only as this represents the vertical centre line of the specimen. The nodes on the axial centre line of the model are constrained in the Z direction. The nodes along the surface at the top of the model represent where it is clamped and are constrained in the X and Y directions and coupled to a master node to facilitate axial loading using RBE2 elements. The nodes on the left-hand side of the model are unconstrained as they represent the free edge of the specimen.

4.1.2.6 Equi-Biaxial Model

Model Description

The Equi-biaxial specimen (previously described in Section 3.1.4 and illustrated in Figure 3.4) was modelled in 3D by importing a *.dxf format drawing of the specimen in AutoCAD. It was subjected to an equi-biaxial deformation in the X direction. To exploit axes of symmetry, only one eighth of the specimen was modelled. A mapped mesh was employed in order to ensure an even mesh on the gauge area of the model. The clamps on the edge of the specimen were also

modelled. Material properties were assigned in the usual manner employed in DIK by fitting a non-linear material model to uniaxial and equi-biaxial experimental data to equal values of the first strain invariant I_1. This model was employed in the same way as the S2 specimen previously mentioned and was used to validate whether material coefficients determined by the fitting procedure matched experimentation carried out on the Zwick tensile testing machine prior to complex simulations of actual components manufactured from the material being carried out.

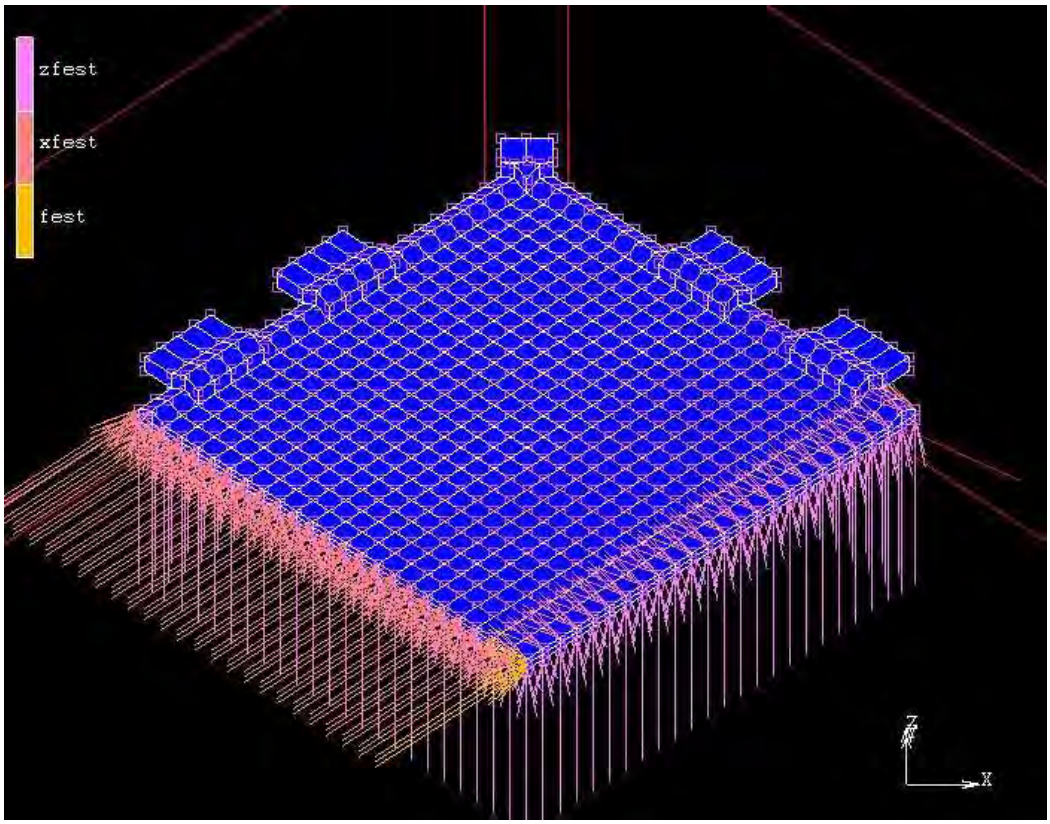

Figure 4.6: Equi-biaxial model modelled as 1/8th of its actual size.

Elements Employed

The elements used in the simulation of S2 specimen were eight-noded, three-dimensional, first-order isoparametric elements. The elements are also suitable

for modelling incompressible and nearly incompressible materials such as elastomers (Herrmann Formulation) **[51]**.

Modelling Boundary Conditions

The nodes on the axial centre-line of the model are constrained in the Z. The modelled clamps were fixed to the ribs of the simulated elastomeric specimen and allowed to slide at 45º to simulate the experimental set-up loading.

4.1.2.7 Dumbbell Model 3D

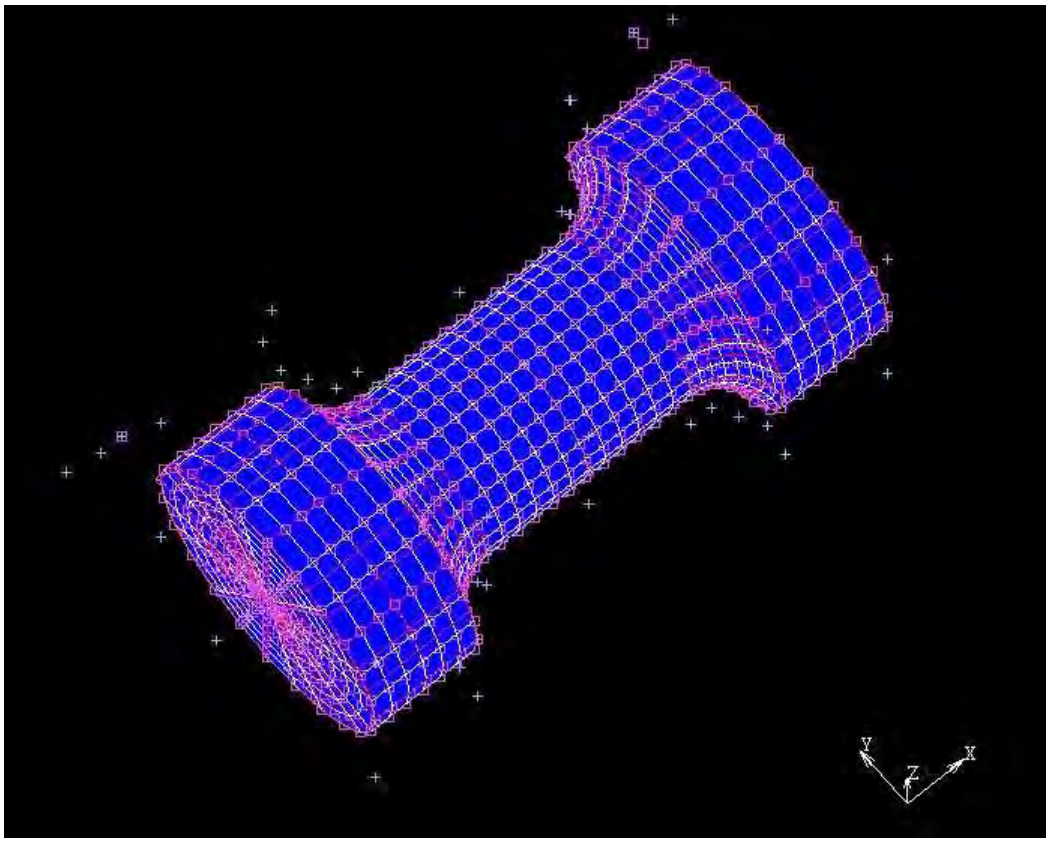

Figure 4.7: Model of a Dumbbell specimen as used in fatigue to failure and uniaxial experiments.

Model Description

The Dumbbell specimen (previously described in Section 3.1.2 and illustrated in Figure 3.2) was modelled in 3D by importing a *.dxf format drawing of the specimen in AutoCAD. It was subjected to a uniaxial deformation in the X direction simulating contact from the clamps as illustrated in Figure 4.5. The material properties were assigned in the usual manner employed in DIK by fitting a material model to uniaxial and equi-biaxial experimental data to equal values of the first strain invariant I_1. This particular model was used to validate whether the material coefficients determined by the fitting procedure matched the experimentation carried out on the Zwick tensile testing machine prior to complex simulations of actual components manufactured from the material being carried out.

Elements Employed

The elements used in the dumbbell specimen simulation were nine-noded, three-dimensional, first-order isoparametric elements (arbitrarily distorted bricks) with Herrmann Formulation. This makes the elements suitable for modelling incompressible and nearly incompressible materials such as elastomers **[51]**.

Modelling Boundary Conditions

The top and bottom edges of the model were clamped in the same manner as the physical experiment as shown in Figure 3.17. Both clamps were constrained in all directions and coupled to a master node to facilitate the load deflection characteristics of the test-piece. Contact and friction were simulated between the clamps and the elastomer material.

4.1.2.8 Notched Dumbbell Model

Model Description

The notched dumbbell specimens (previously described in Section 3.1.3 and illustrated in Figure 3.3) were modelled in axisymmetric elements with an axis of symmetry along the X-axis. They were subjected to a uniaxial deformation in the X direction. It was possible to convert this model to a 3D one by simply revolving the model about the axis of symmetry. This method of modelling saves on computation time without a compromise in accuracy of the results. A saving is achieved by making use of the symmetry along the X and Y-axes on the centre of the specimen, as illustrated in Figure 4.8. In this case the auto mesh function was used with some refinement in the critical areas around the notch and clamps.

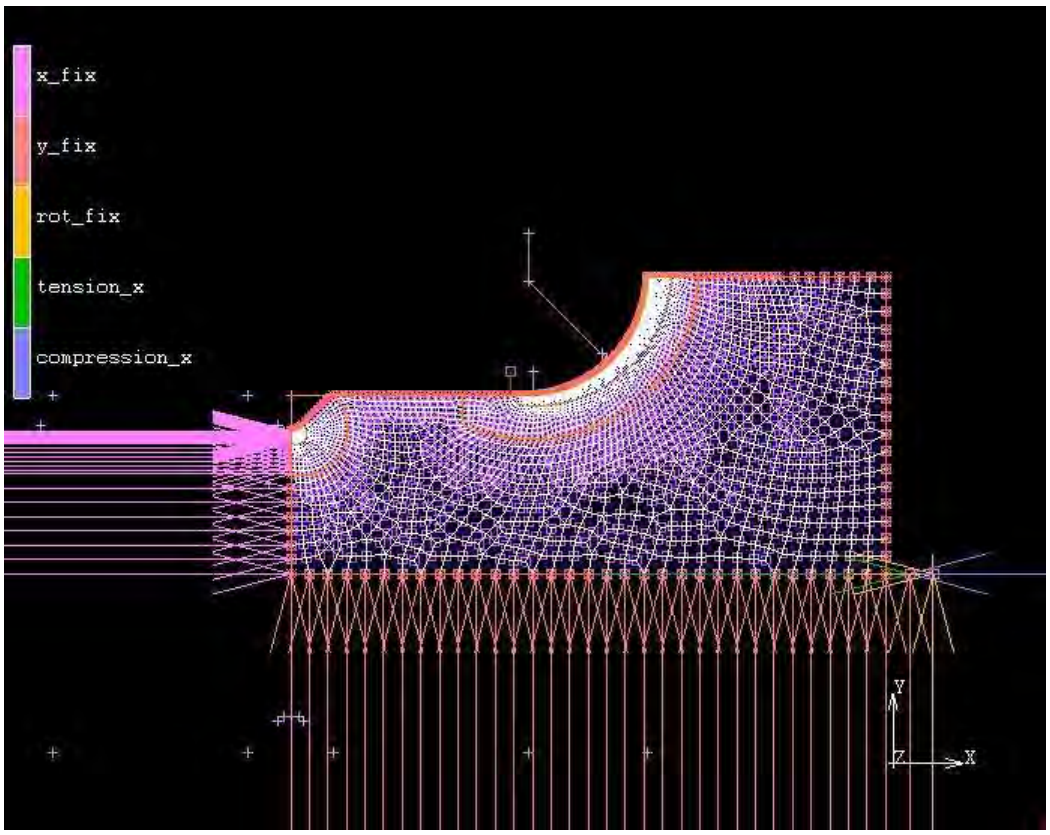

Figure 4.8: Axisymmetric model of a modified dumbbell specimen.

The material properties were assigned by fitting a Yeoh model to uniaxial and equibi-axial experimental data to equal values of the first strain invariant I_1 and the stress softening subroutine was run on these models.

Elements Employed

The elements used in the simulation were Axisymmetric, arbitrary ring elements with a quadrilateral cross section, with the Herrmann formulation. The elements are also suitable for modelling incompressible and nearly incompressible materials such as elastomers (Herrmann Formulation) **[51]**.

Modelling Boundary Conditions

The nodes along the bottom edge of the model on the X-axis of symmetry were constrained in the Y direction. This represents the horizontal centre line of the specimen. The nodes on the left hand side of the model are constrained in the X direction only as this represents the vertical centre line of the specimen at the notch. The Clamp over the right-hand end of the model is coupled to a master node to allow the simulation of the load application using RBE2 elements. The nodes on the top edge of the model are unconstrained as they represent the free surface of the specimen.

4.1.3 The Significance of Strain Invariant I_2 in Multi-Axial Simulation of Elastomeric Deformation

The relevance of I_2 can most easily be demonstrated with a simple example. Using the James Green Simpson constitutive equation for stress in rubber-like materials and the relationship

$$I_2 = \lambda_1^2 \lambda_2^2 + \lambda_2^2 \lambda_3^2 + \lambda_3^2 \lambda_1^2 \qquad \text{Eqn. 4-1}$$

Where λ_1, λ_2 and λ_3 are the three principle stretch ratios and for equi-biaxial tension $\lambda_1 = \lambda_2 = \lambda$ Eqn. 4-2

and for incompressibility $\lambda_1\lambda_2\lambda_3 = 1$ Eqn. 4-3

so $\lambda_3 = \lambda^{-2}$ Eqn. 4-4

Therefore equation 4-1 becomes

$$I_2 = \lambda^2\lambda^2 + \lambda^2(\lambda^{-2})^2 + (\lambda^{-2})^2\lambda^2 \quad \text{Eqn. 4-5}$$

$$I_2 = \lambda^4 + 2\lambda^{-2} \quad \text{Eqn. 4-6}$$

and $$\frac{\partial I_2}{\partial \lambda} = 4\lambda^3 - 4\lambda^{-3} \quad \text{Eqn. 4-7}$$

Stress is given by $$\sigma = \frac{\partial W}{\partial \lambda} \quad \text{Eqn. 4-8}$$

which for the James Green Simpson constitutive equation results in

$$\sigma_1 = C_{10}\frac{\partial I_1}{\partial \lambda} + C_{01}\frac{\partial I_2}{\partial \lambda} + C_{11}\frac{\partial I_1(I_2-3)}{\partial \lambda} + C_{11}\frac{\partial I_2(I_2-3)}{\partial \lambda} + 2C_{20}\frac{\partial I_1(I_1-3)}{\partial \lambda} + 3C_{30}\frac{\partial I_1(I_1-3)^2}{\partial \lambda} \quad \text{Eqn. 4-9}$$

where C_{10}, C_{01}, C_{11}, C_{20} and C_{30} are elastic constants determined from specific material test data.

If a reasonable value is applied for C_{01} of say 0.04 MPa and a stretch ratio λ of 3 is assumed, the component of stress for the second term in the equation becomes

$$C_{01}\frac{\partial I_2}{\partial \lambda} = C_{01}(4\lambda^3 - 4\lambda^{-3}) \quad \text{Eqn. 4-10}$$

$$= 0.04\ (108 - 0.15)$$

$$= 4.31\text{MPa}$$

which alone is a significant component of stress for a rubber-like material irrespective of the evaluation of the other terms.

The requirement to develop procedures for modelling stress softening using higher order material models is returned to in Section 8, 'Recommendations for further research'.

4.1.4 Using Subroutines to Vary Material Constants

The proposed concept uses two subroutines called "Write" and "Read" and was based on the determination of local material properties at each Gauss point in the FEA model using the first strain invariant (I_1) of the Green deformation tensor **[52]**. Initially the material properties are defined as a function of I_1. Hence for the fitting procedure to determine the C_{ij} coefficients, different sets of uniaxial and bi-axial tests are carried out to the same I_1 state. For example a uniaxial deformation of 100% is equal to an I_1 value of 5.05. A bi-axial test to the same value of I_1 should only necessitate inducing a strain of 55.4%. The working hypothesis is that elastomer samples deformed to the same value of I_1 experience the same amount of stress softening regardless of whether the loading mode is uniaxial or bi-axial, which justifies the use of a Yeoh model to explore the concept of varying material coefficients to represent this viscoelastic phenomenon. The hypothesis is illustrated in Figure 4.9 where a sheet of NR was deformed twice to 55.4% and then an S2 specimen was cut from it and strained uniaxially to failure. This is then compared to a previously unstrained S2 sample which is unixially loaded to 100% twice and on the third cycle stretched to failure.

The two stress-strain curves are virtually coincident, indicating that testing to equal values of I_1 is a good indicator of damage experienced by

elastomers under the deformation modes in this exercise. Sets of uniaxial and bi-axial tests were then carried out to strains corresponding to several different values of I_1.

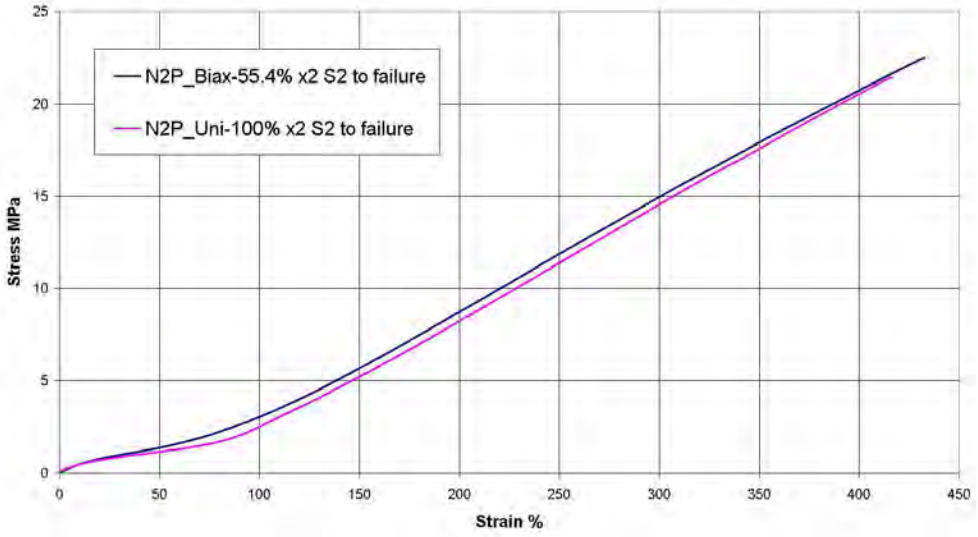

Figure 4.9: Damage effects of deformation to equal values of I_1 under both uniaxial and equi-biaxial loading

Figure 4.10 depicts the loading cycles of a series of tests on the NBR material described in Section 3.4. Each specimen was cycled 5 times. The 5^{th} cycle was taken to be representative of the damage experienced by the specimen and the fitting to determine the C_{ij} coefficients was carried out for this 5^{th} cycle. The experiments were carried out at different values of I_1 in order to determine the magnitude of the stress softening corresponding to these values.

The C_{ij} coefficients for the Yeoh material model were then determined for each set of uniaxial and bi-axial tests and then plotted as functions of I_1 as shown in Figure 4.11.

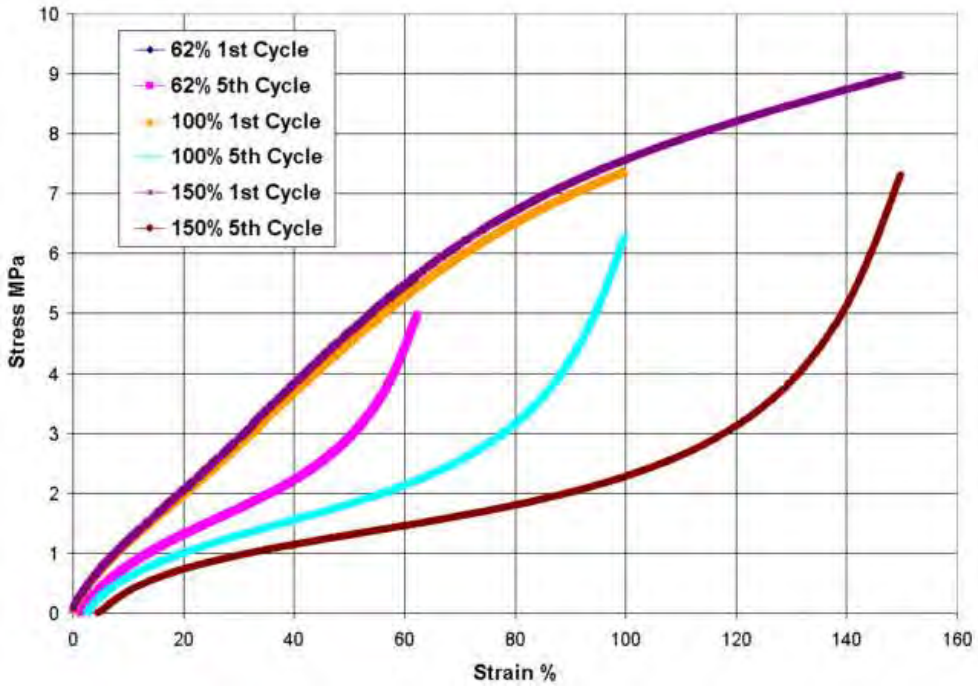

Figure 4.10: 1st and 5th upward cycles for a silica filled NBR material

A polynomial fit was applied to each set of points for C_{10}, C_{20} and C_{30} as shown in Figure 4.11

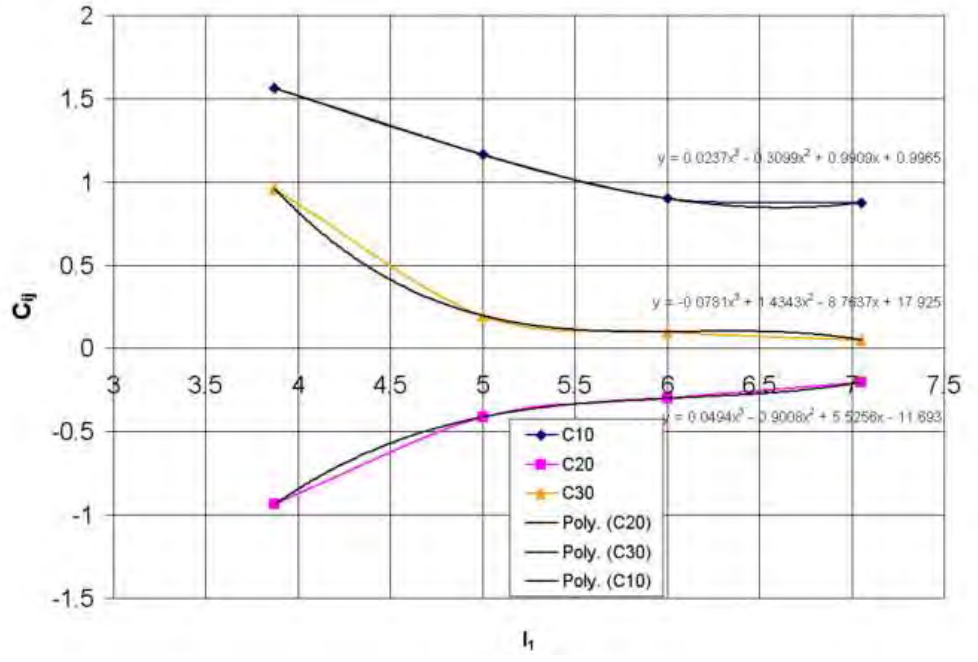

Figure 4.11: The change in C_{ij} with increasing values of I_1

For the 1st simulation, material properties were defined for a fitting of the 1st experimental stress-strain cycle to the maximum I_1 value, as in the case of the test to 150% in Figure 4.10. As stated, normally the C_{ij} coefficients define the material properties for the entire material model. This defines the model as a homogenous, isotropic material as it can reasonably be considered to be before the first loading cycle. As the simulation of the 1st strain cycle is run, the 1st subroutine "Write" is implemented. This records the I_1 values reached for each Gauss point in the model throughout the deformation.

The second simulation implements the second subroutine "Read" which reads the I_1 values recorded for the 1st simulation and assigns new material properties for each Gauss point in the model. The new material properties are a function of the previous maximum I_1 values reached in the 1st simulation. They come from the polynomial equations shown in Figure 4.11. In this way the simulation defines an inhomogeneous material as cyclic deformation continues and stress softening in the material is taken into account.

4.1.5 Experimental Verification Using the Pure Shear (Planar) Specimen Test as an Example

Experiments were carried out on pure shear (planar) samples made from a carbon filled natural rubber (measuring 196 x 20 x 2mm) with pre-prepared cracks 35mm long. Figure 4.12 shows the experimental set-up. The specimens were clamped in the Zwick Tensile Testing machine (5kN load cell) and were cycled 5 times at a feed rate of 20mm per minute to a maximum integral strain of 50%. The ICP system recorded the deformation for the first and fifth cycles. The reflective points can be seen on the sample in Figure 4.12.

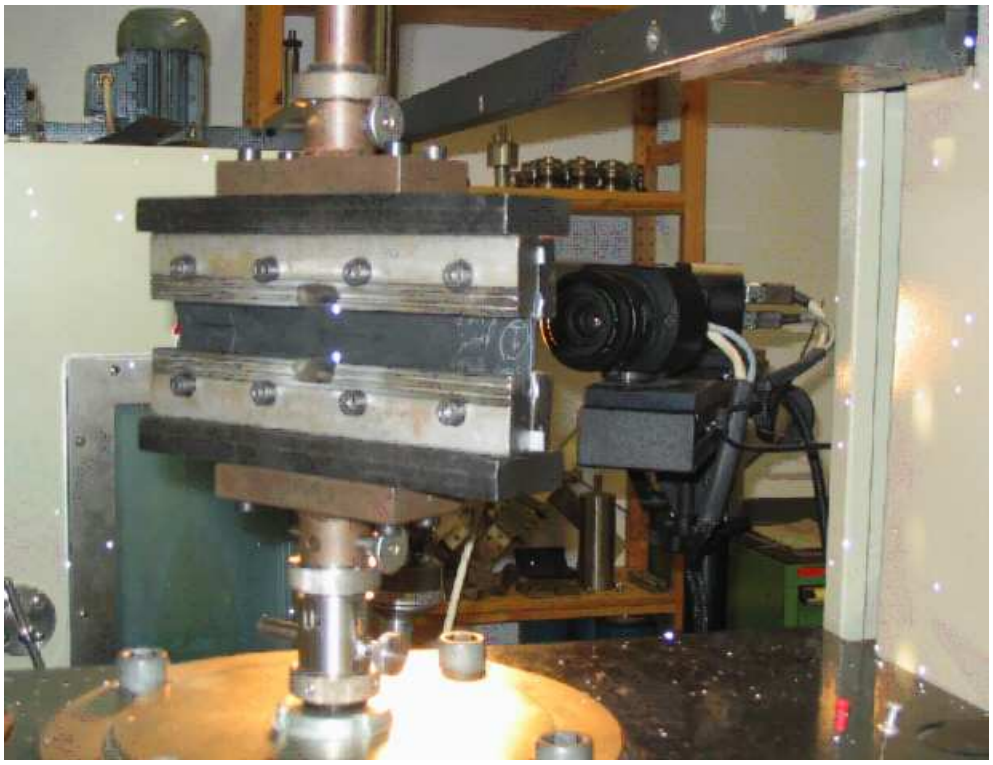

Figure 4.12: ICP system and experimental set up with planar specimen clamped at zero strain

This enables the optical extensometer to accurately measure the integral strain applied to the specimen. Figure 4.13 shows the results of the ICP measurement and the manner in which a section line was assumed at the axis of symmetry in order to plot the strains. The section line was taken from the cut/crack tip in the x direction and a plot was made of the strain data in the y axis versus distance from the crack tip along this section line. When compared with the FE calculation used to model the experiment, similarities in the strain fields between the two are evident for both cases. As stated, the simulations were carried out using the Yeoh material model **[47][53]** with coefficients determined by fitting the material model to uniaxial and bi-axial data obtained experimentally for 1^{st} and the 5^{th} load cycle.

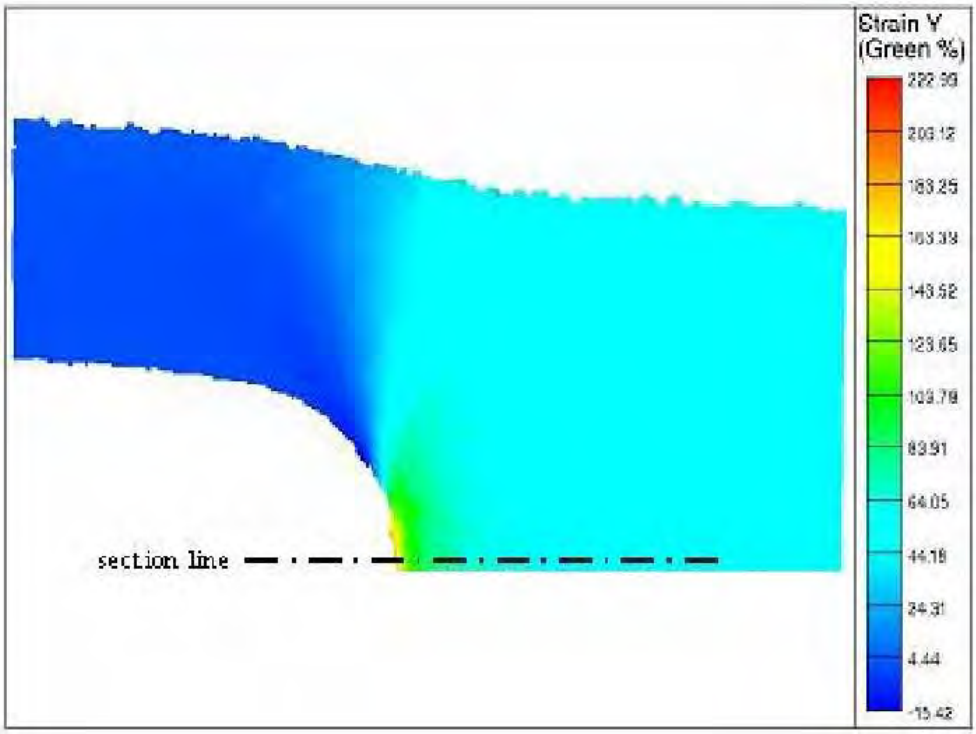

Figure 4.13: ICP measured strains for pure shear specimen with 35mm crack at 50% integral strain

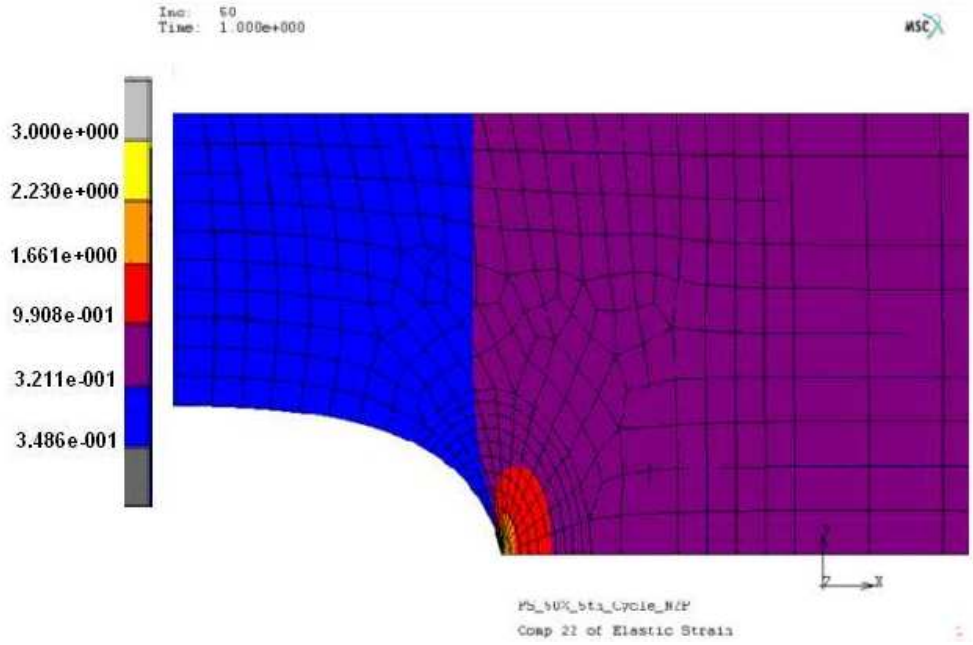

Figure 4.14: FEA calculated strains for pure shear specimen with 35mm crack at 50% integral strain (note that strains in this graph are depicted on a logarithmic scale)

For the simulation of the first cycle of the planar sample, the coefficients determined from the fitting to the 1st experimental load cycles were used. For the simulation of the 5th cycle of the planar sample, the model coefficients determined from the fitting to the 5th experimental load cycles were used **[54]**. Figure 4.14 shows the results of the simulation of the 5th cycle of the planar specimen. Similarly a section line was taken on the FE simulations at the horizontal axis of symmetry and the results were plotted along with the results of the ICP measurements.

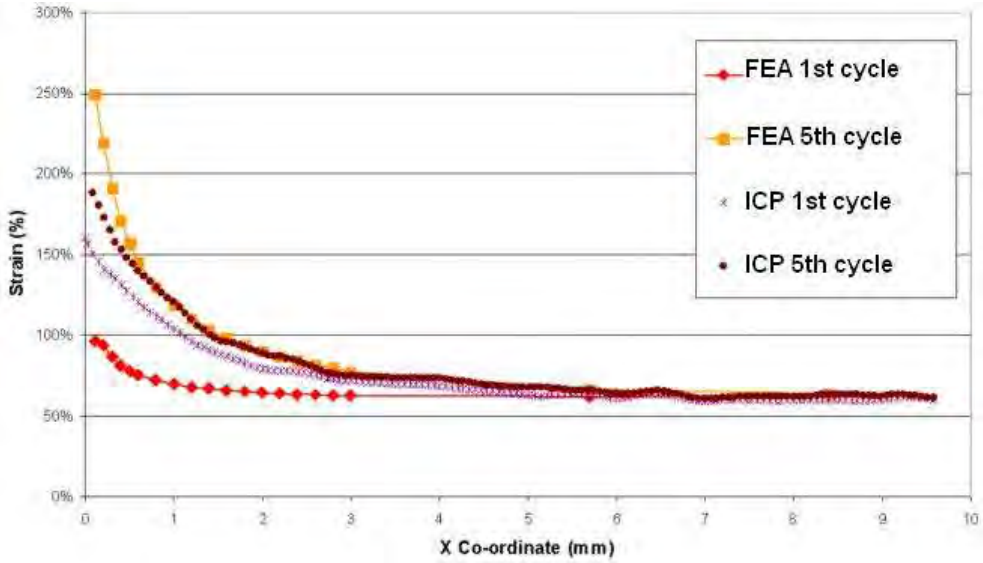

Figure 4.15: Comparison of FEA and ICP for a Pure Shear Specimen

From the graph in 4.15 the effects of stress softening in the specimen in the region of the crack tip were evident in the ICP data from the 1st cycle to the 5th cycle. It can also be seen that there was satisfactory correlation between the FEA and the ICP results at distances greater than 0.5mm from the crack tip for the 5th cycle. The FEA calculation however predicted a lower local maximum strain for the simulation of the 1st cycle. This is unsurprising as higher strains will be achieved at the crack tip giving a high amount of stress softening even for the crack opening in the 1st cycle. The ICP system is capable of measuring this

phenomenon, whereas FEA is not capable of predicting it. Another reason for this may be attributed to the fact that there was evidence of crack growth as the specimen was strained to 50%. In Figure 4.16 the same specimen strained to failure is shown in order to illustrate the manner in which the crack propagated through the sample.

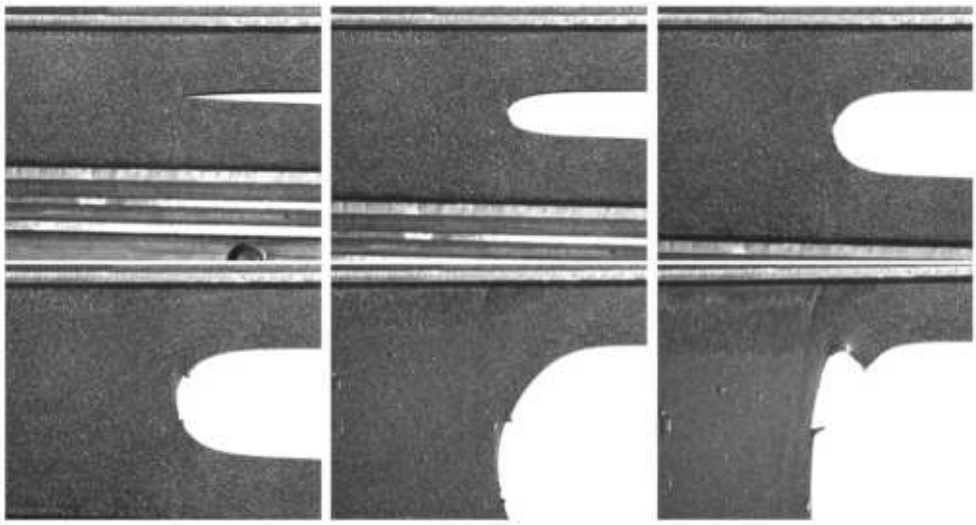

Figure 4.16: Crack propagation and the resultant failure of the planar sample

4.1.6 Experimental Verification Using the Pure Shear (Planar) Specimen with a Centrally Located Hole.

In order to verify the stress softening subroutines, a tensile test was carried out on a planar silica filled NBR specimen (195 x 20 x 2mm). The sample was modified with a 5mm diameter hole punched in the centre. It was clamped in the Zwick tensile testing machine (5kN load cell) and the specimen was cycled 5 times at a feed rate of 20mm per minute to a maximum integral strain of 50%. The ICP system recorded the entire deformation sequence from the first to the fifth cycle. The results of the ICP measurement for the 5^{th} cycle at 50% strain are shown in Figure 4.17.

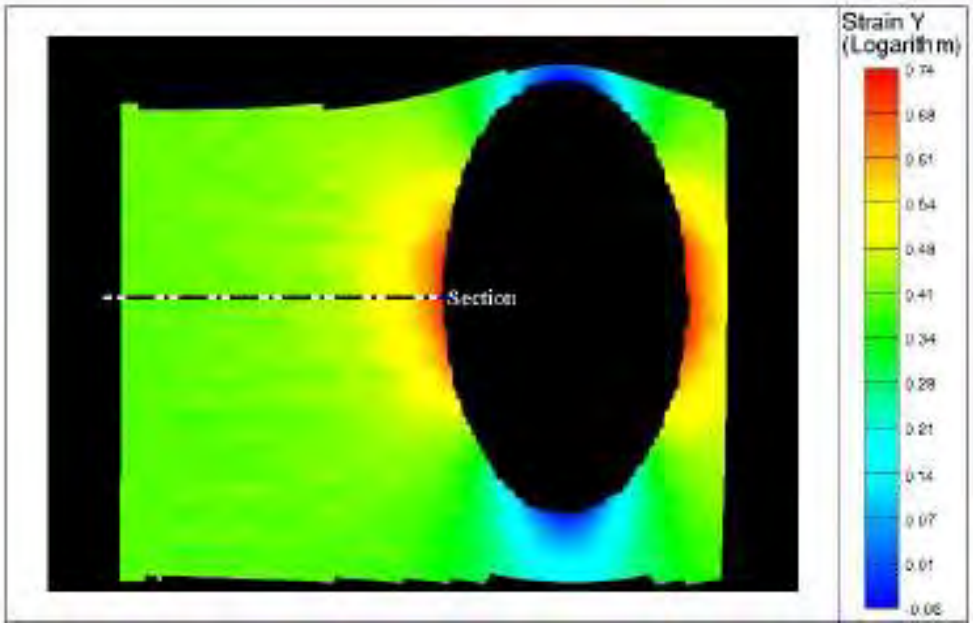

Figure 4.17: Photogrammetric measurement of the strains in the Y axis of the specimen with a 5mm hole, for the 5th cycle at 50% integral strain

A centre line on the axis of symmetry (section line) was taken from the edge of the hole in the x direction and a plot was made of the strain data in the y axis verses distance from the edge of the hole along this line as shown in Figure 4.17. The results were also plotted graphically as depicted in Figure 4.18. The FEA simulation of the same experiment was then carried out, but this time the stress softening subroutines were implemented as described in Section 4.1.3. The results of the simulation, including stress softening, can be seen in Figure 4.19. As in the ICP tests, an axis of symmetry (centre line / section line) was taken in the FEA simulation and both the first and the 5th cycles measured in the experiment were compared with the 1st and 2nd FEA simulation modelling stress softening. Comparisons are shown in Figure 4.18. Figures 4.17 and 4.19 show similarities between the strain fields. Scrutiny of Figure 4.18 indicates that the effects of stress softening were evident in both FEA and ICP.

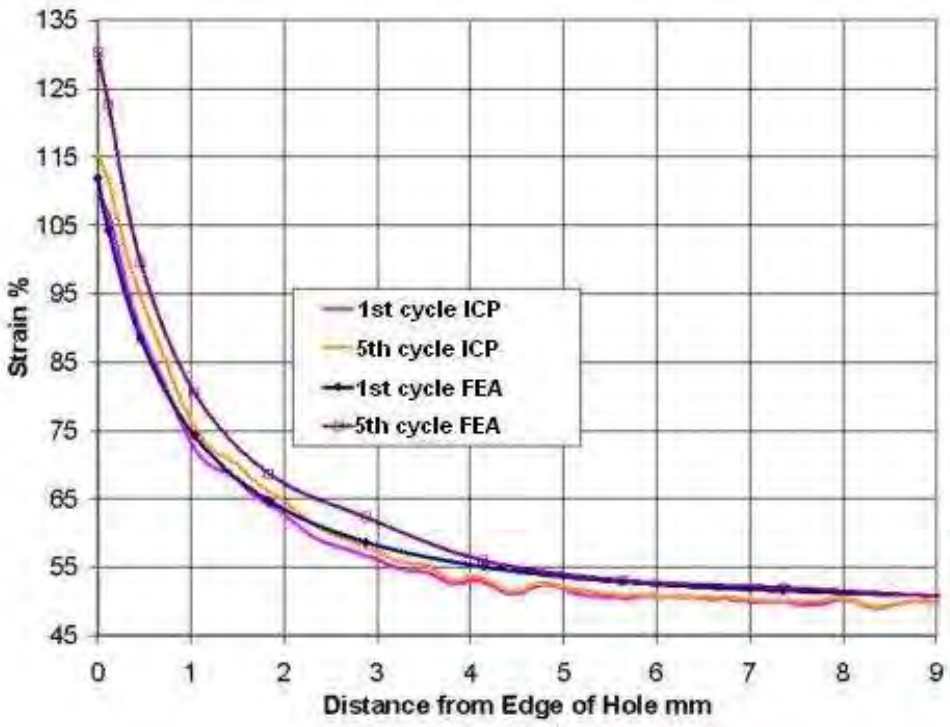

Figure 4.18: Comparison of ICP and FEA results including Stress softening

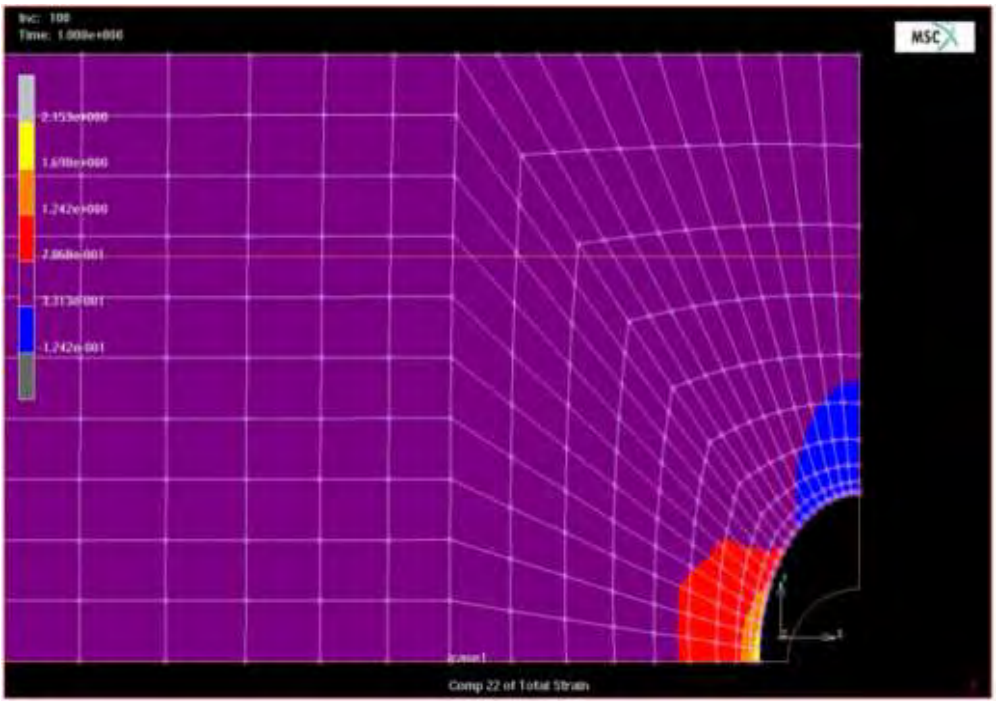

Figure 4.19: Results of FEA simulation including stress softening showing a maximum simulated engineering strain of 130% at the left edge of the hole

The first experimental cycle measured by the ICP system correlated with the FEA simulation of the same cycle and therefore validated the simulation. The difference between measured and simulated 5^{th} cycles was much more pronounced. The FEA exhibited higher stress softening effects than were measured by the ICP system. The respective strains were 130.4% and 115.4%.

Chapter 5 Results of Fatigue Tests and Simulations

5.1 Overview

This section describes fatigue to failure tests on plain dumbbells for the six materials specified in Section 3.2. The data from the tests was used to compile Wöhler curves for each material. In addition to this testing, further fatigue to failure tests were carried out on the model materials E1 M and N1 M but using notched dumbbell specimens in order to evaluate the notch sensitivity of the two materials.

5.2 Results of Fatigue Tests on Plain Dumbbells

The stress depicted in the graphs is 'engineering stress'. In reality, true stress will vary throughout each of these load controlled fatigue to failure tests. Engineering stress is found by dividing the applied load by the original cross-sectional area of the test sample. Often a more meaningful insight is given into elastomeric stress if 'true stress' is considered. At any instant in the test, true stress is defined as the applied load divided by the deformed cross-sectional area. Hence, for an isochoric material, true stress 't' for uniaxial loading is found from the relationship:

$$t = \sigma\lambda \qquad \text{Eqn. 5-1}$$

where λ is the stretch ratio at that instant.

Moreover, under load control, the specimen will elongate in successive cycles and cross-sectional area will also reduce accordingly for this reason throughout the test. Engineering stress is used here as a simplifying assumption to aid comparisons. Figure 5.1 shows the changing modulus for four specimens of the N1 M material during uniaxial fatigue testing to failure. The behaviour illustrated

in this Figure was typical for all materials tested and graphically illustrates the scatter associated with fatigue life tests of elastomeric specimens. Figures 5.2, 5.3 and 5.4 show Wöhler curves for the full range of materials tested with life in cycles plotted respectively against maximum force, engineering stress and strain. All plots illustrated are derived from the same testing parameters where the minimum stress for each cycle was zero. The full range of elastomers subjected to dynamic testing is shown, but the two materials that warrant close scrutiny are the model materials; E1 M (EPDM) and N1 M (NR), since these two were the materials investigated using ICP. Obviously, Figures 5.2 and 5.3 exhibit a direct relationship between force and engineering stress, so a comparison of fatigue life where engineering stress and strain are the ordinates follows. Predictably, in general the harder / stiffer materials exhibited higher fatigue lives for a given stress, whilst the softer / less rigid materials exhibited higher fatigue lives for a given strain. This supports the view that fatigue life is related to dynamic stored energy, since greater energy is available to fail rigid samples in comparison with less rigid samples at constant strain amplitudes, whilst greater energy is available to fail less rigid samples in comparison with rigid samples at constant stress amplitudes. The tests were carried out under load amplitude control. This infers that the dumbbells will continue to elongate throughout the tests, so reliance on Wöhler curves plotted with strain as ordinate can be misleading and provide minimal insight into fatigue life. This is highlighted by comparing Figures 5.4 with Figures 5.3 and 5.2. All Figures show the results from the same experiments, just in different formats.

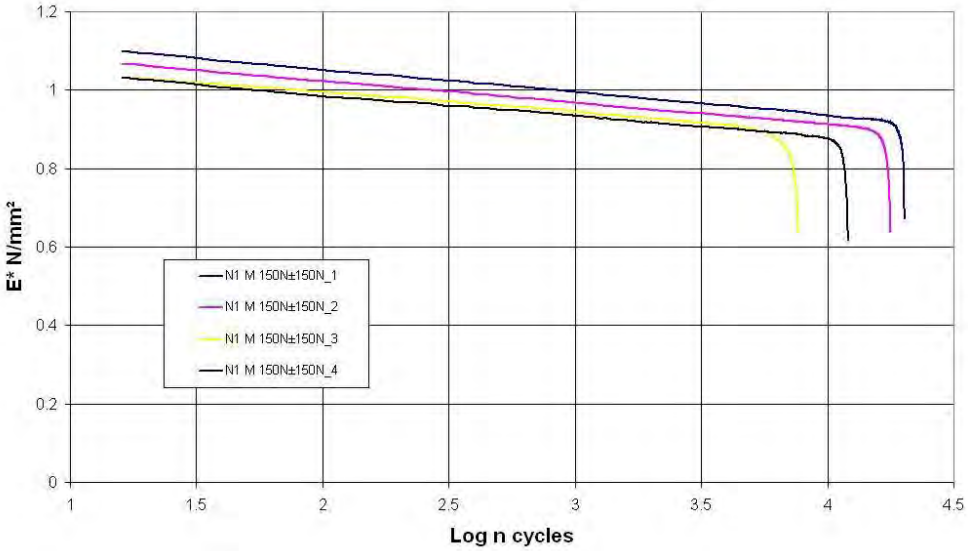

Figure 5.1: Changing modulus over duration of fatigue to failure test.

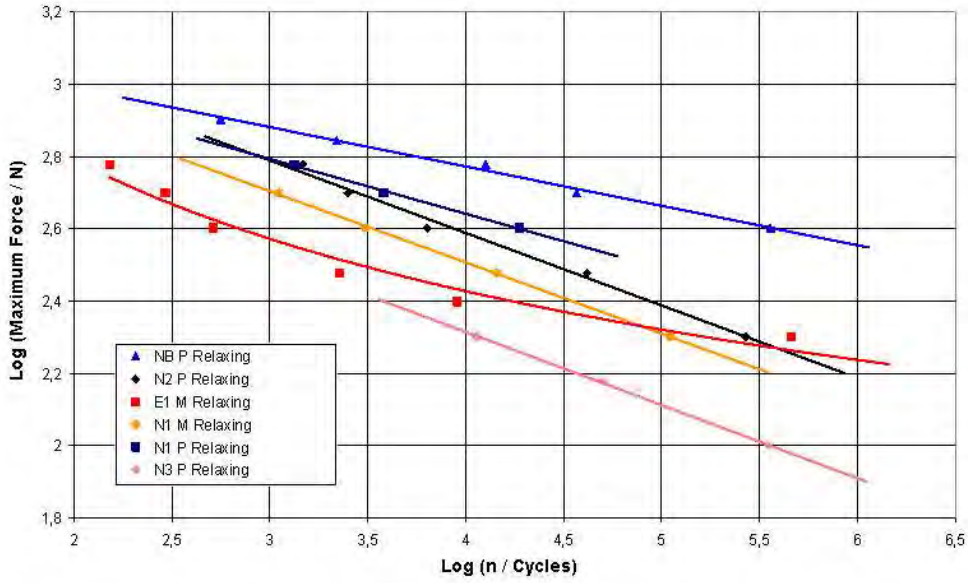

Figure 5.2: Wöhler curve for plain dumbbells maximum applied force.

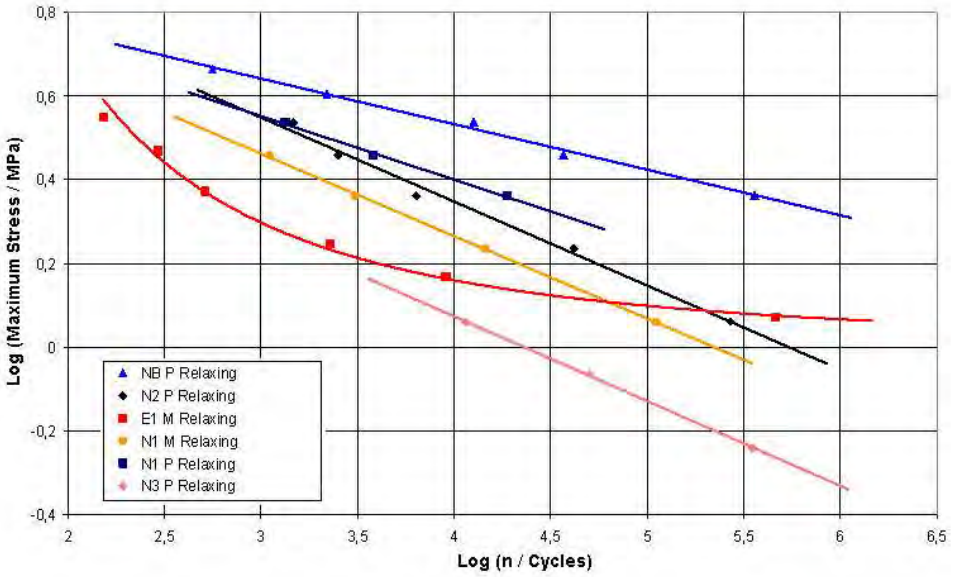

Figure 5.3: Wöhler curve for plain dumbbells displaying maximum stress as ordinate.

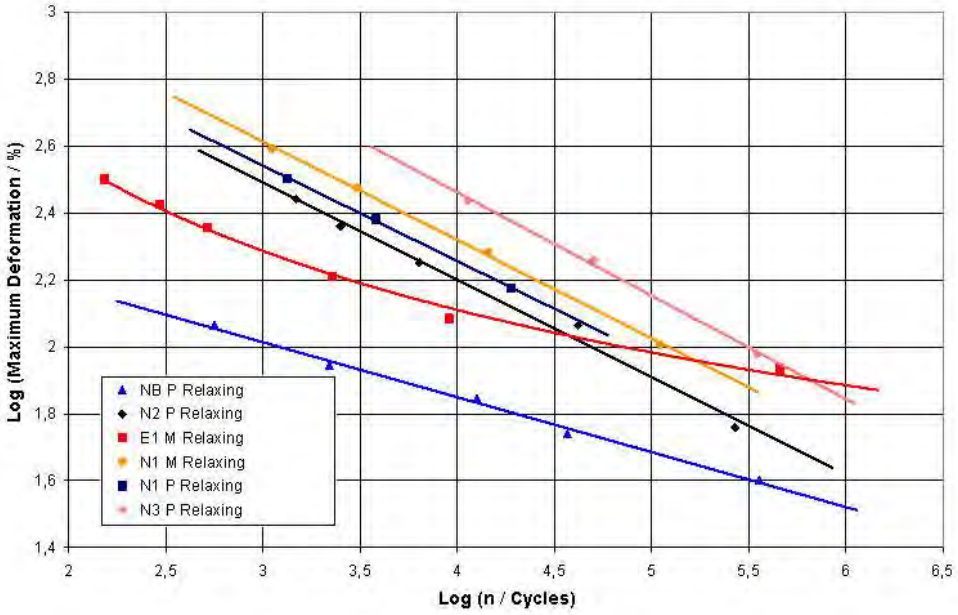

Figure 5.4: Wöhler curve for plain dumbbells displaying maximum strain as ordinate.

Fatigue tests are markedly different if either constant strain amplitude or constant stress amplitude is used as the control parameter for dynamic loading. With the former, the load required to maintain the constant strain will fall away with

repeated cycling and successively less energy will be used to deform the test piece. Fatigue tests can be inordinately long or not induce a failure in this situation. Conversely, with a constant stress (or load) amplitude, the test-piece will continue to elongate throughout the test and the strain limits of the test facility may be exceeded. These extremes are indicative of the difficulties encountered in conducting a meaningful fatigue test on an elastomer.

Figures 5.5 and 5.6 illustrate the difference between what are termed relaxing and non relaxing load conditions. Relaxing conditions are when the minimum load is zero during the fatigue to failure cycle as in Figure 5.5. Figure 5.6 illustrates non-relaxing loading where a minimum load is maintained on the specimen throughout the fatigue to failure test until rupture.

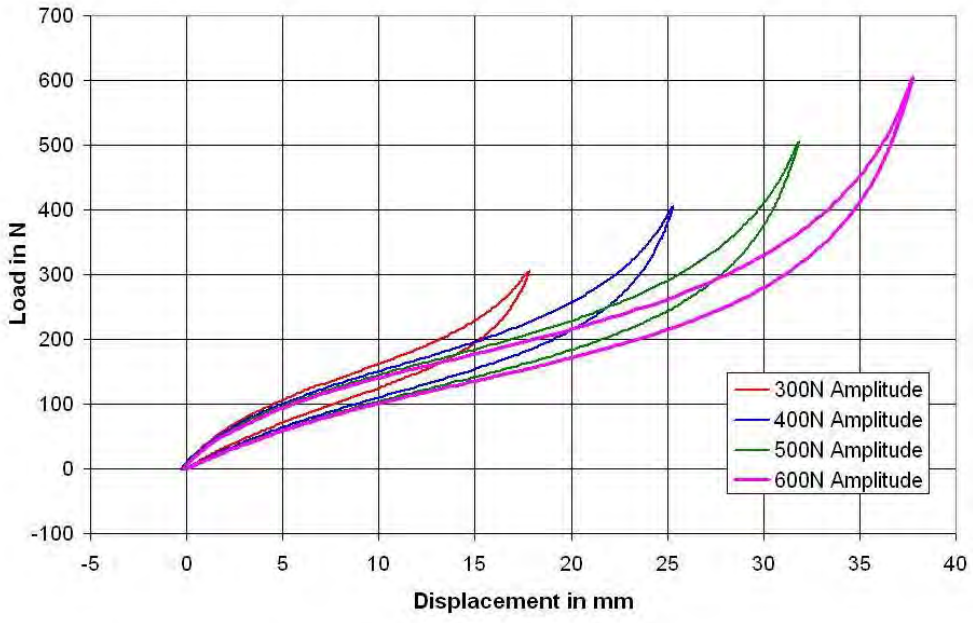

Figure 5.5: Examples of hysteresis curves for relaxing load cases applied during fatigue to failure tests.

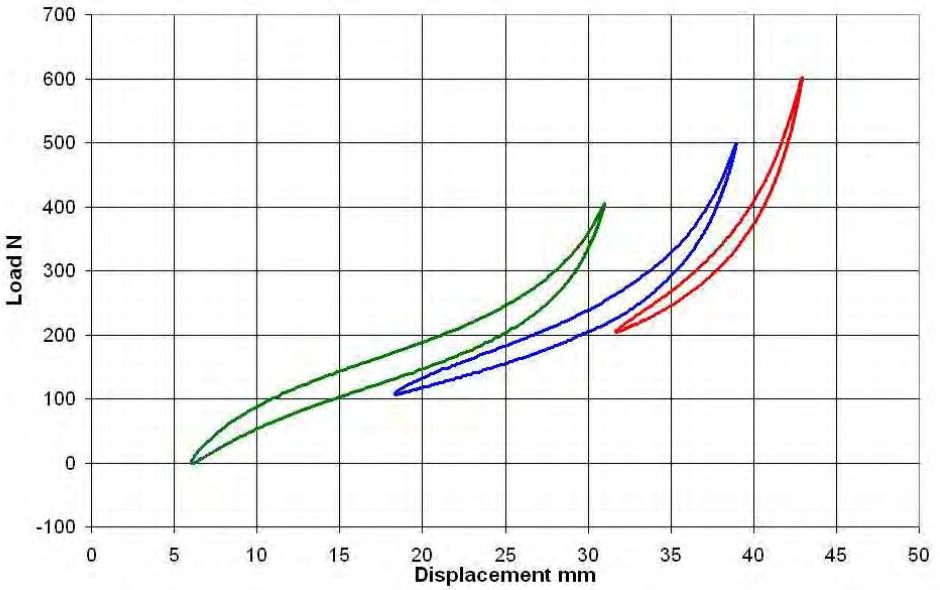

Figure 5.6: Examples of hysteresis curves resulting from non-relaxing loads applied during fatigue to failure tests.

Figures 5.3 and 5.4 show results for the 6 different model and commercial materials together. For clarity Figure 5.7 and 5.8 show the same results but just for the model EPDM material in isolation. In addition to the relaxing tests (denoted by the ◆ symbol) the non relaxing tests are also plotted (denoted with a ■ symbol). The effect of the increase in preload for the same load range (as shown in Figure 5.6) was to prolong the average fatigue life for the specimens tested under that load condition.

Abraham et al **[26]** looked for an effective method to predict the fatigue life of elastomers from Wöhler curves. From Abraham's research on non-strain crystallising elastomers it was concluded the best predictor for the fatigue life of an elastomer was obtained when the log of dynamic stored energy was plotted against the log of fatigue life. It can be seen from Figure 5.9 in comparison with Figures 5.6 and 5.7 that as all the points on the curve approximately fall on a single line indicating that Abraham's energy criteria applies in this case of EPDM.

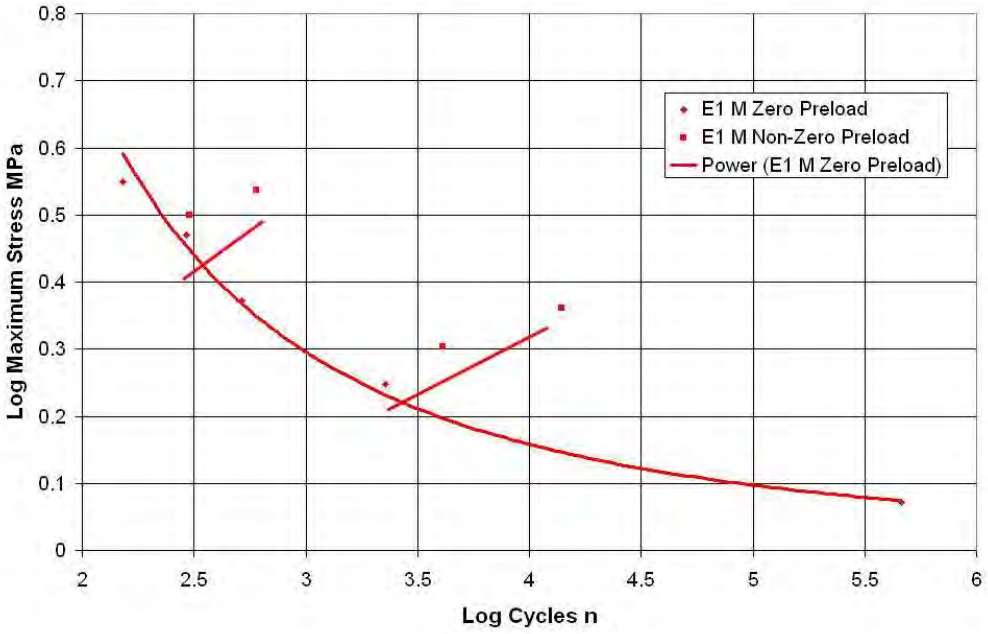

Figure 5.7: Results of fatigue tests for EPDM showing fatigue life and maximum engineering stress.

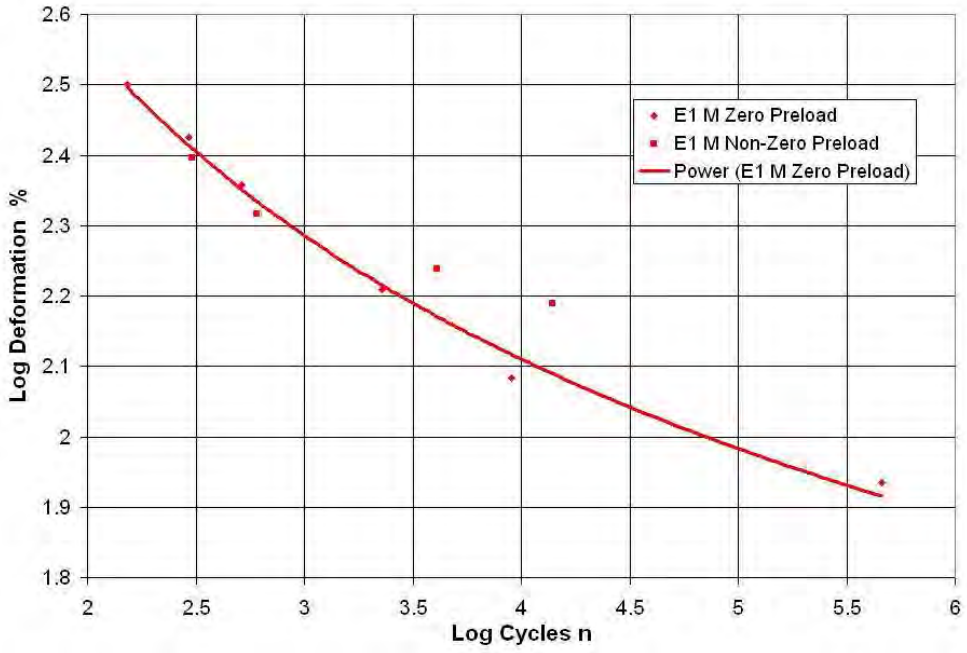

Figure 5.8: Log log plot of maximum deformation plotted against log of fatigue life for EPDM.

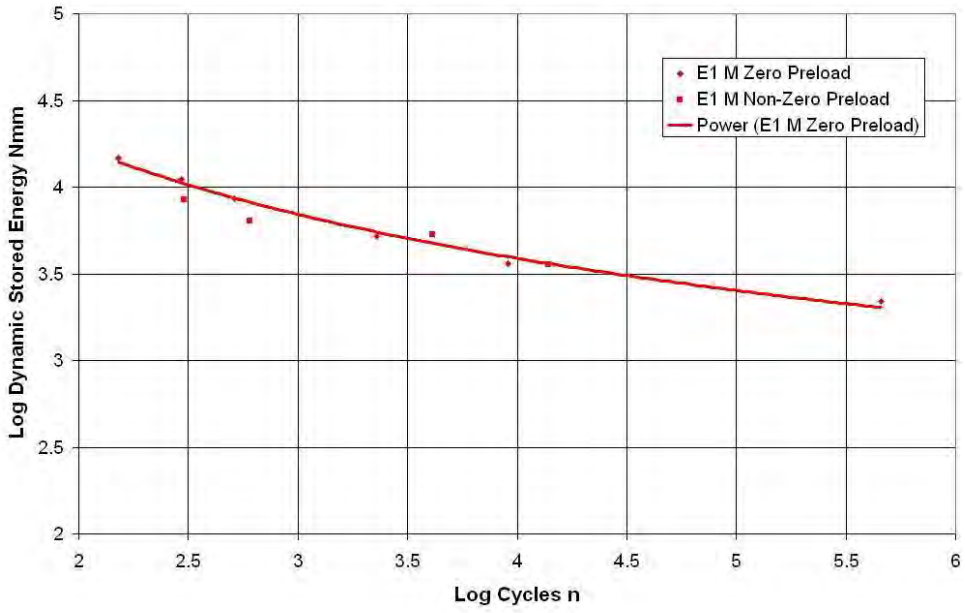

Figure 5.9: The dynamic stored energy plotted against fatigue life in cycles for EPDM.

The same results for the model NR material are presented in the same manner in the following Figures 5.10 to 5.12 with both results for relaxing (denoted with the ◆ symbol) and non-relaxing (denoted with a ■ symbol) testing conditions. What is most notable however, shown in Figure 5.12, is that the energy criteria for the prediction of fatigue life as proposed by Abraham does not appear to apply in the case of the NR material. It is probably because NR is a strain crystallising material and the formation of crystallites during cycling will have a profound effect on the dynamic stored energy in each cycle.

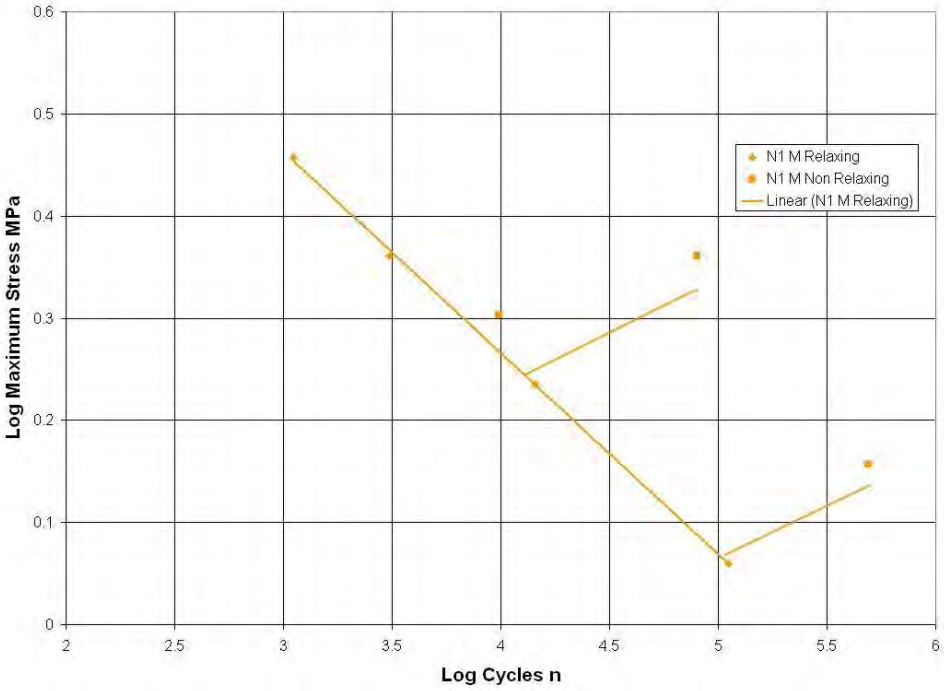

Figure 5.10: N1 M maximum stress verses log number of cycles.

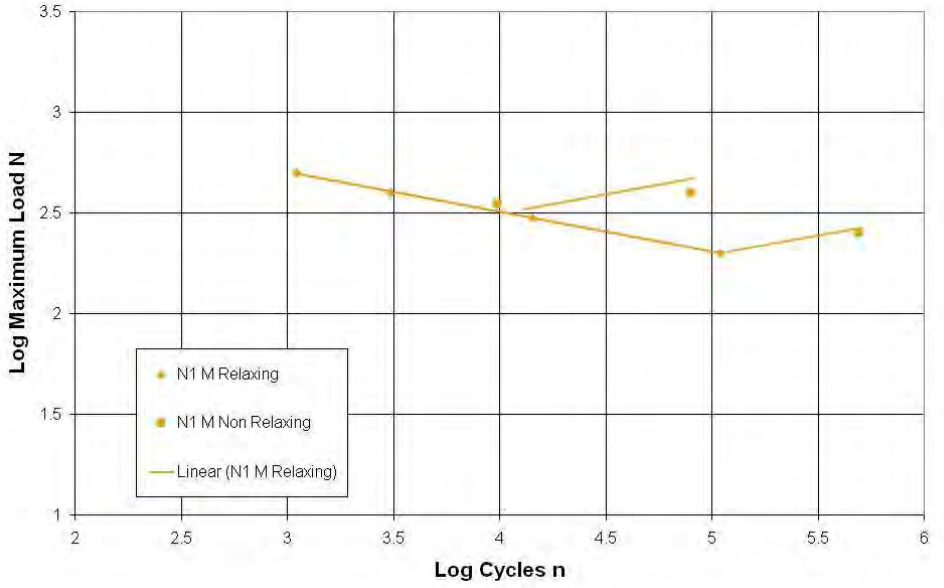

Figure 5.11: N1 M maximum load versus number of cycles.

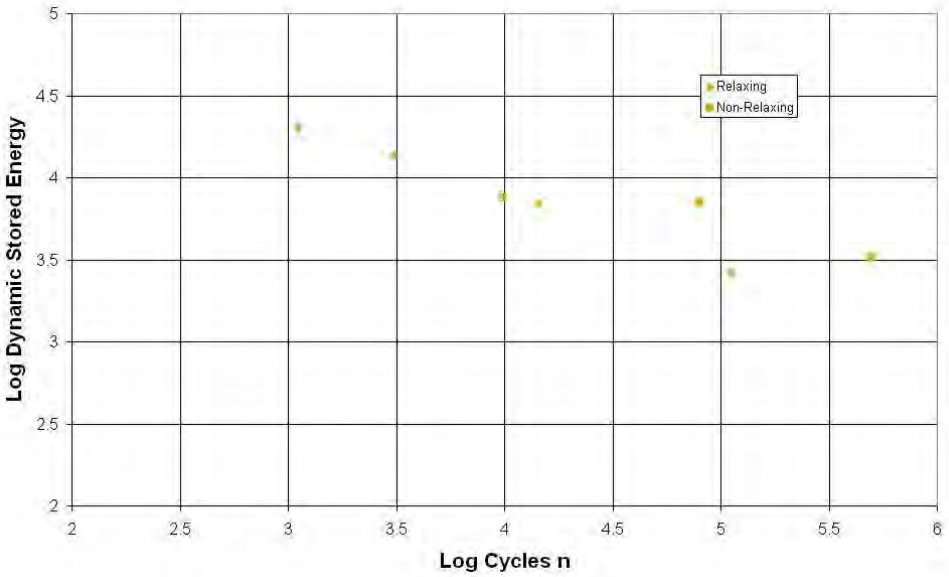

Figure 5.12: Dynamic stored energy plotted against log number of cycles.

5.3 Results of Notched Dumbbell Tests

Earlier in Section 3.1.3 notched dumbbell specimens were discussed. Specimens were prepared from the E1 M and N1 M model materials. The specimens were tested under fatigue load conditions that matched the maximum engineering stresses that the plain dumbbell specimens experienced during testing. The results for EPDM are presented in Figures 5.13 and 5.14 along with the plain dumbbell results under relaxing load conditions from Section 5.2. Two configurations of the notched dumbbell results are presented, the 45º notch with a 0.75mm and a 0.375mm fillet radius at the notch. The results for the same experiments are presented in two different forms. Figure 5.13 shows the fatigue life plotted against maximum force while Figure 5.14 shows life plotted against maximum stress. From the results it is evident that the severity of the notch has a direct influence on the fatigue life of the specimen.

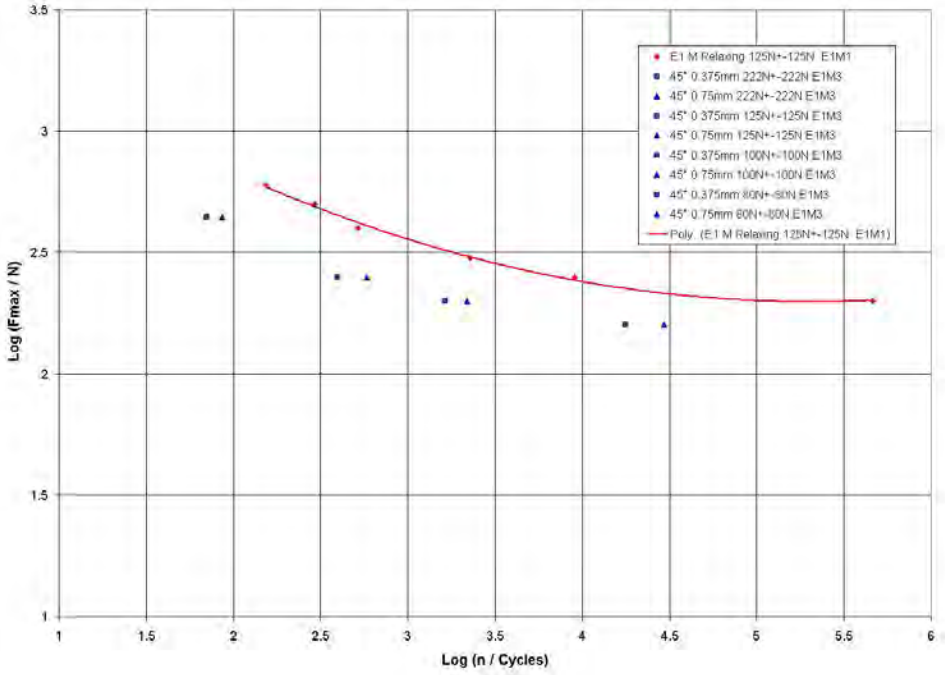

Figure 5.13: E1 M Wöhler curve maximum force as ordinate

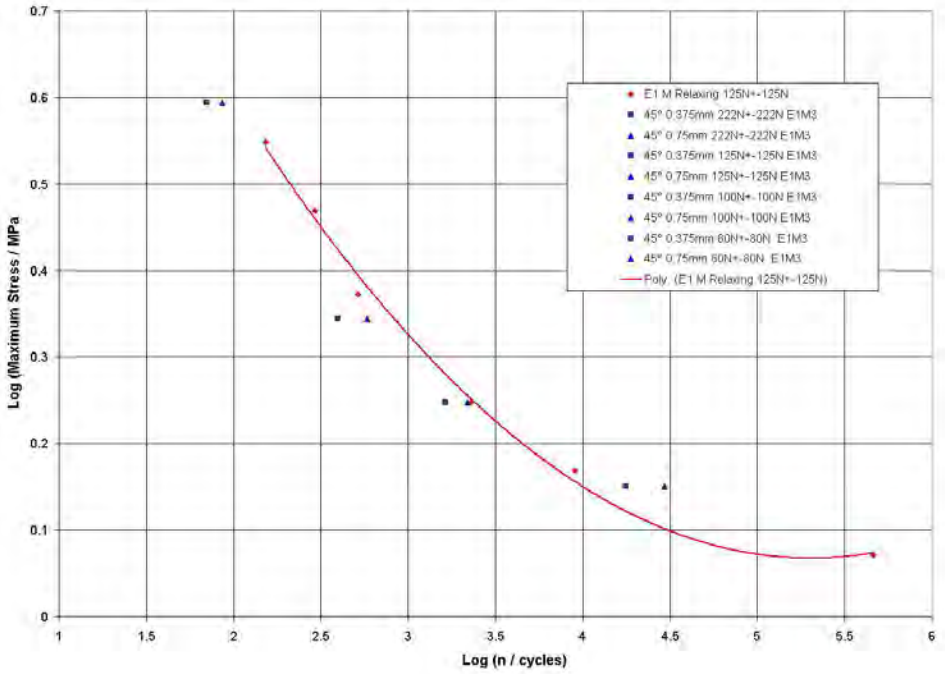

Figure 5.14: E1 M Wöhler curve maximum stress as ordinate

The results for the N1 M material are presented in Figures 5.15 and 5.16. The severity of the notch has the same effect on the fatigue life of the NR material but

the differences are not as pronounced as for the EPDM material which is non-strain crystallizing. Also there was a higher amount of scatter in the results. A theory relating to this is presented in Section 5.5.

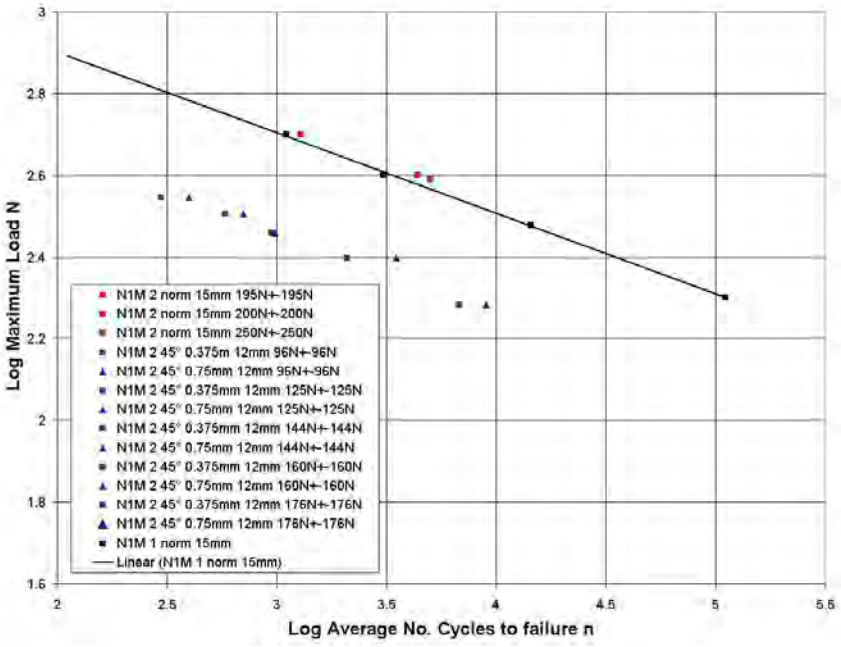

Figure 5.15: N1 M Wöhler curve maximum load as ordinate

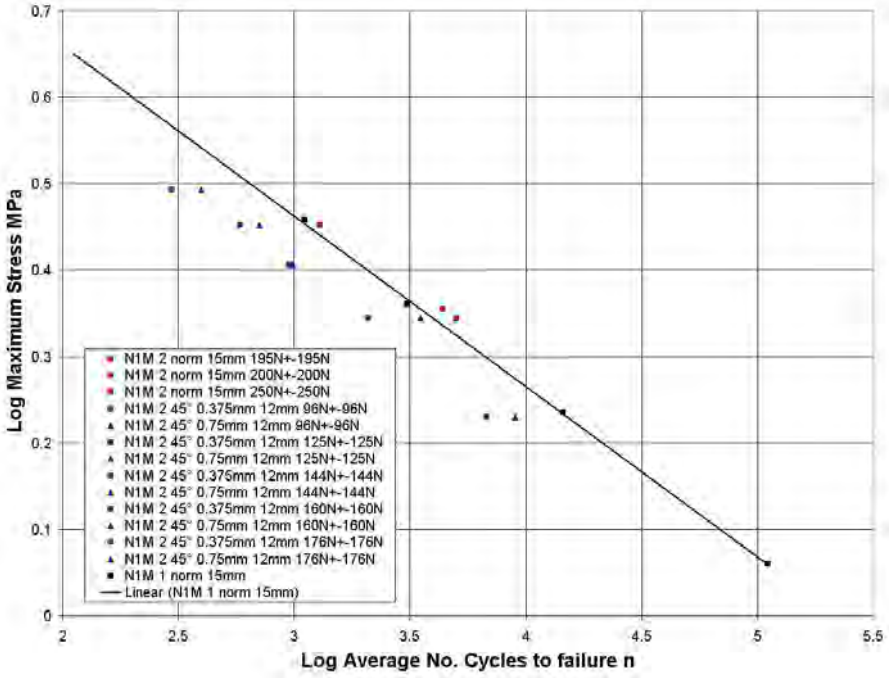

Figure 5.16: N1 M Wöhler curve maximum stress as ordinate

5.4 Influence of Notch Geometry

Rubber is almost unique as an engineering material in that it can absorb more energy per unit mass than practically all others. This ability to absorb such large amounts of energy has a secondary benefit in that notches and other stress raisers are less injurious in elastomeric components than in conventional linear materials. Also, the influence of material flaws can be reduced through the use of increased mixing times in the production of rubber which has the effect of reducing the size and frequency of large agglomerates of filler, voids etc. As a result it is statistically less likely that a flaw of a large critical size will occur in an area of high stress in a component. The ability of rubber to withstand very large deformations has a secondary benefit. An example of this can be seen in Figure 5.24 where a specimen that has a notch and fillet radius incorporated into its design is subjected to tensile loading. The tensile deformation has the effect of reducing the severity of the stress concentration as the fillet radius and the notch angle increase with deformation.

5.4.1 The Probability of Flaws Occurring in Critical Volumes in Elastomer Samples

Previous research carried out by Abraham et al **[55]** suggested that fatigue failure prediction in rubber elastomers was subject to high levels of scatter due to the random presence or absence of large flaws in the critical volume. Contrary to previous research, **[56]**, Abraham showed that fatigue cracks usually emanated from flaws of 200 μm or greater. Hence, as depicted in Figure 5.17, he was able to prove that scatter in fatigue tests of rubber samples could be reduced by introducing uniform flaws (glass beads) of 200 micron diameter in size. Though this provides insight into the nature of dynamic failure in elastomers, the

generally reduced fatigue lives of the samples were unrepresentative of the mean fatigue lives from standard tests or of the fatigue lives that would be anticipated for dynamically loaded components.

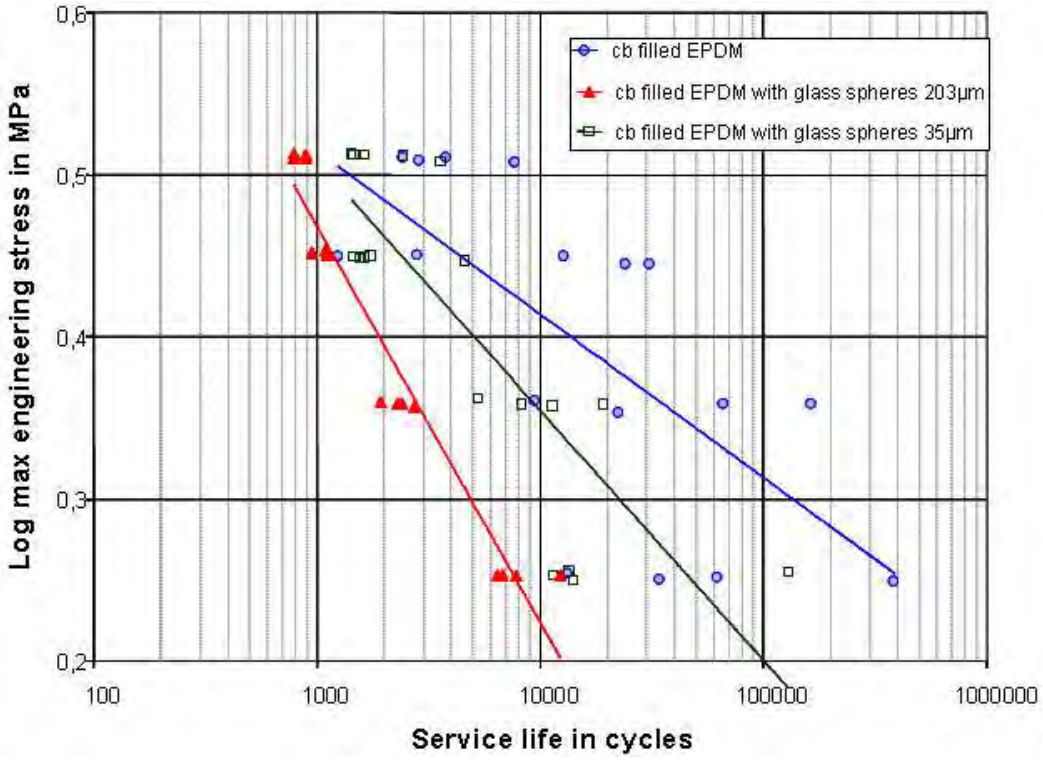

Figure 5.17: Wöhler curve for EPDM with and without glass beads of different sizes [22]

Abraham's research gave rise to the hypothesis that fatigue failures at stress concentrations in notched specimens did not provide consistent repeatable fatigue data because flaws of a size likely to induce failure (200 µm+) were often absent in the critical vicinity of the notch.

Abraham took an EPDM test specimen and cut 30 thin slices and examined them with a Dispersion Index Analysis System (DIAS) which consisted of a light microscope, connected to a particle size measurement system, developed by DIK, to determine the prevalence of different sized flaws in representative

EPDM sliced samples. A typical result from these experiments is shown in Figure 5.18. It is worth noting that in this analysis only one flaw in excess of 200 μm was identified for all 30 measurements.

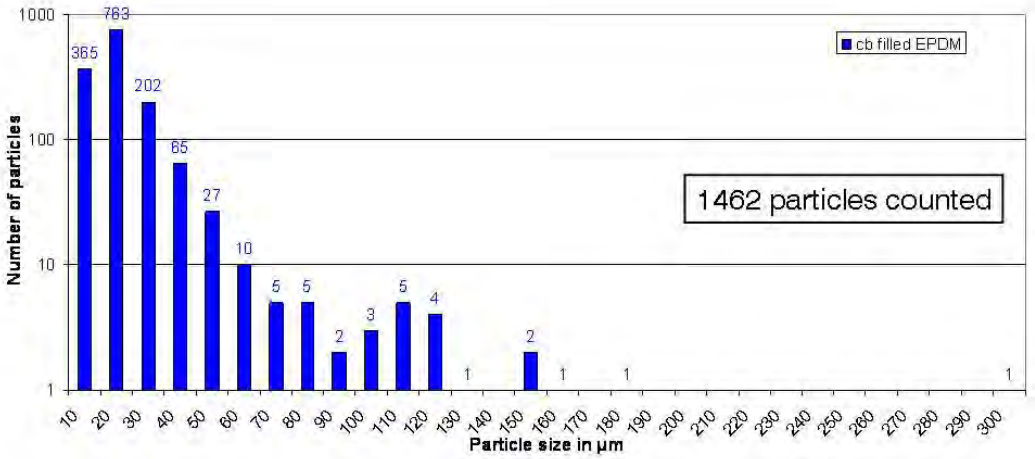

Figure 5.18: Particle distribution as analysed with a DIAS [23]

Returning to Figure 5.17 which shows Wöhler curves for EPDM materials with glass beads used to artificially introduce a consistent flaw size; a reduction in scatter for the samples containing 203 micron beads is evident. It is also notable that the low fatigue lives attributable to the samples containing 203 μm beads, were not of the same order of life of standard EPDM test samples, which lacked artificially induced stress concentrations.

To relate these findings to stress concentration, CT scan X-rays were performed on the dumbbell test samples used to determine fatigue life using Computer Tomography with a GE Phoenix X-ray, 180kV/15W high power nano-focus tube. Each test sample had a volume of 3500mm^3. A typical sample on one of the measurements made is shown in Figure 5.20. The number of large flaws and their sizes detected in a representative sample are shown in Figure 5.19.

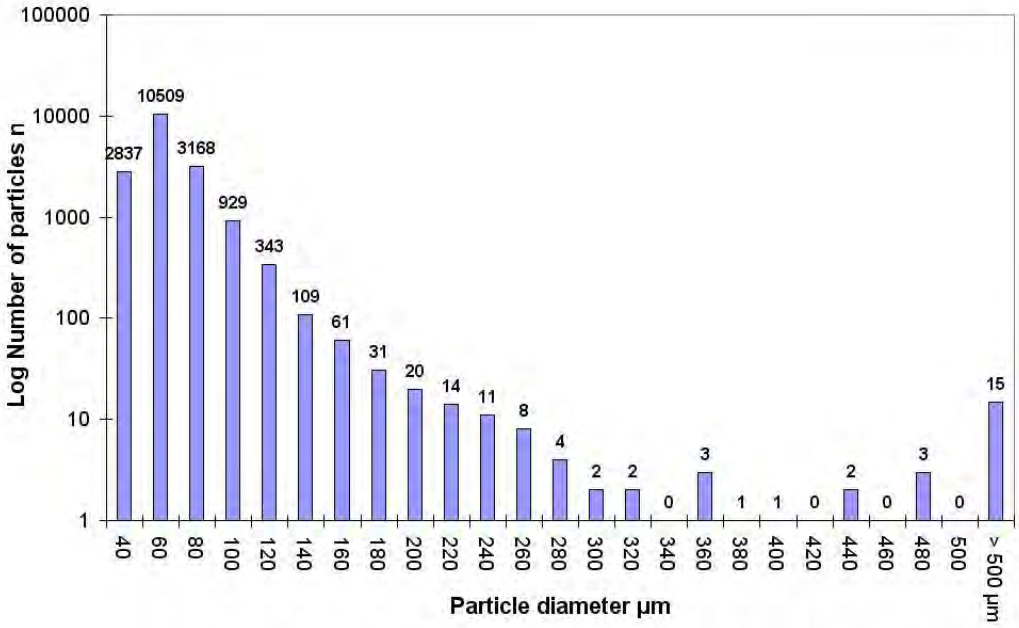

Figure 5.19: Particle count for a typical dumbbell test specimen as analysed on a CT X-ray machine

Surprisingly, there were typically 20 flaws of approximately 200 µm diameter in size (and hence of the magnitude thought to induce fatigue failure) and a further 51 larger flaws, up to a size of 500 µm were observed. This can explain why notched test samples exhibit a lack of uniformity when used to provide fatigue life data. The probability of a significantly sized flaw occurring in the vicinity of the notch can be shown to be approximately 82% for the test samples used, as shown in Section 5.5. This finding explains the unusual phenomenon that notched rubber specimens, cyclically loaded uni-axially, occasionally have longer fatigue lives than un-notched specimens subjected to the same loading conditions.

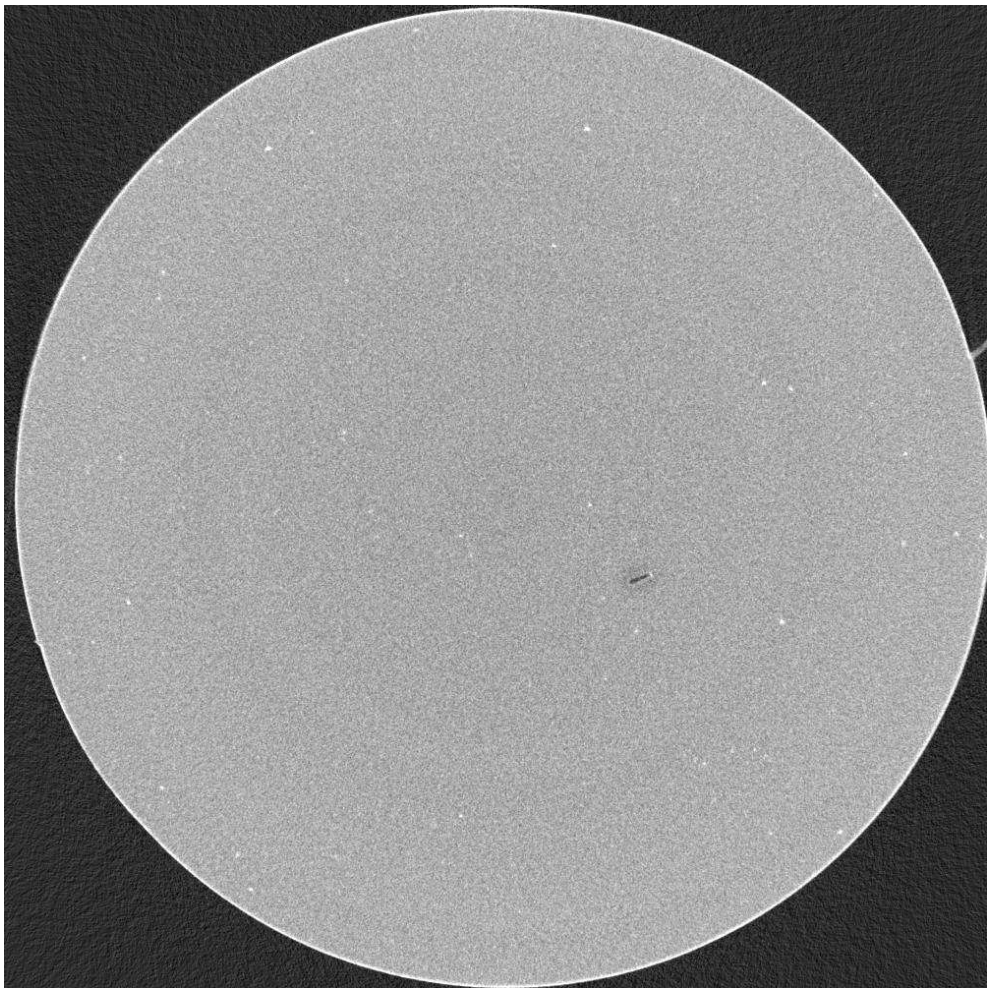

Figure 5.20: X-ray of a dumbbell sample showing particles of various sizes along with a large void close to the centre of the sample [57]

5.4.2 Diminishing Notch Severity at Higher Deformations

Some calculations of stress concentrations at the notch were made using accepted empirical methods and the empirical formula for static stress concentration is given in Eqn 5-2.

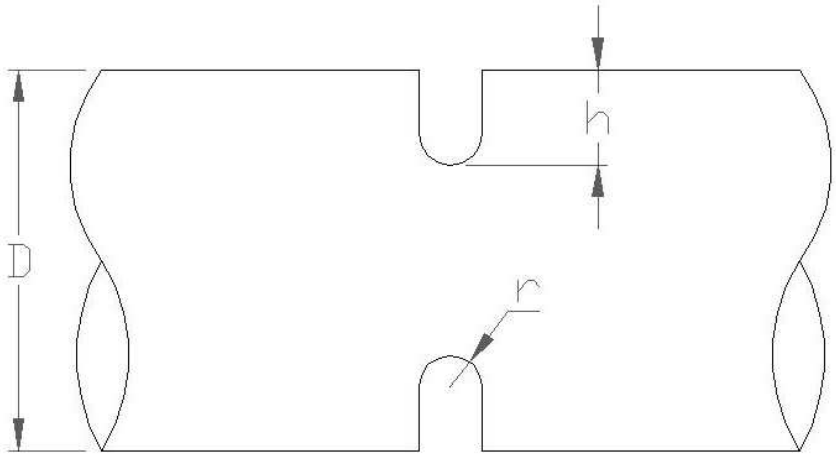

Figure 5.21: U-notches for a specimen of a rectangular section

$$K_{tu} = C_1 + C_2\left(\frac{2h}{D}\right) + C_3\left(\frac{2h}{D}\right)^2 + C_4\left(\frac{2h}{D}\right)^3 \qquad \text{Eqn. 5-2}$$

Where C_1-C_4 are determined according to the criteria set out in Table 5-1.

	$0.1 \le h/r \le 2.0$	$2.0 \le h/r \le 50.0$
C_1	$0.850 + 2.628\sqrt{h/r} - 0.413h/r$	$0.883 + 2.069\sqrt{h/r} - 0.009h/r$
C_2	$-1.119 - 4.862\sqrt{h/r} + 2.575h/r$	$2.732 - 4.157\sqrt{h/r} + 0.176h/r$
C_3	$3.563 - 0.514\sqrt{h/r} - 2.402h/r$	$-8.859 + 5.327\sqrt{h/r} - 0.320h/r$
C_4	$-2.294 + 2.713\sqrt{h/r} + 0.240h/r$	$6.294 - 3.239\sqrt{h/r} - 0.154h/r$

Table 5-1: Formulae for the determination of constants for K_{tu}

Then to determine the stress concentration of a V-notch, values calculated for K_{tu} Table 5-1 are substituted into the following equations provided that the appropriate condition for $\frac{2h}{D}$ are satisfied for the equation and that the values for D, h and r are the same as for the U-notch shown in Figure 5.22. High deformations in elastomers result in pronounced changes in notch geometry in a

component under load. The influence of dimensional change in a notch specimen under load is considered here.

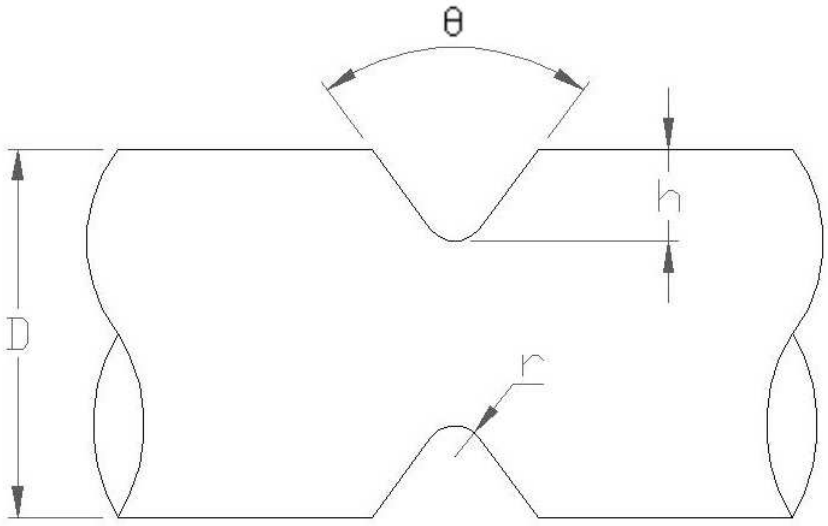

Figure 5.22: Stress concentration factor for the V-notch, $K_{t\theta}$

$$K_{t\theta} = 1.11K_{tu} - \left[0.0275 + 0.000145\theta + 0.0164\left(\frac{\theta}{120}\right)^8\right]K_{tu}^2 \quad \text{Eqn. 5-3}$$

for $\frac{2h}{D} = 0.4$ and $\theta \le 120^\circ$

$$K_{t\theta} = 1.11K_{tu} - \left[0.0275 + 0.000142\theta + 0.0075\left(\frac{\theta}{120}\right)^8\right]K_{tu}^2 \quad \text{Eqn. 5-4}$$

for $\frac{2h}{D} = 0.667$ and $\theta \le 120^\circ$

However a problem existed in that, of the dumbbells used in the experiments, only the 9mm minor diameter samples satisfied the appropriate condition of $\frac{2h}{D} = 0.4$ for Equation 5-3 and the remainder of the 12mm minor diameter

dumbbells had a value for $\frac{2h}{D} = 0.2$. Hence, it was necessary to formulate a new equation to meet this condition.

Observing equations 5-3 and 5-4, the only variables that change are the ones multiplied by θ. Using the reasonable assumption that the change is approximately linear, these variables can be plotted against 2h/D and the equation for the straight line can be extrapolated backward to predict values for $\frac{2h}{D} = 0.2$ as shown in Figure 5.23.

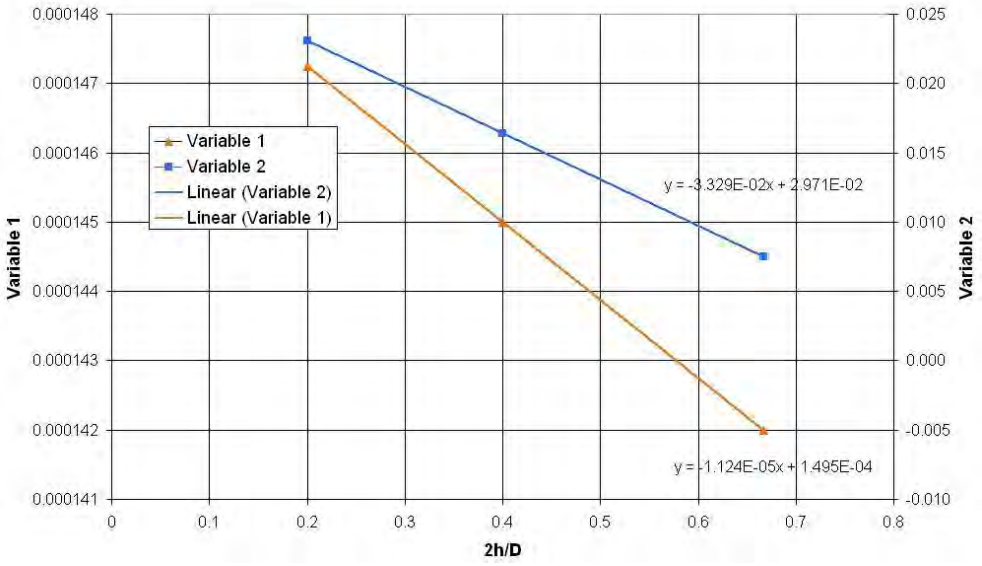

Figure 5.23: Extrapolation of variables one and two for $\frac{2h}{D} = 0.2$

Taking the new values for the variables multiplied by θ and substituting them for the corresponding values in equation 5-3 or 5-4 gave the new eqn 5-5:

$$K_{t\theta} = 1.11K_{tu} - \left[0.0275 - 0.000061\theta + 0.023066\left(\frac{\theta}{120}\right)^8\right]K_{tu}^2 \quad \text{Eqn. 5-5}$$

for $\frac{2h}{D} = 0.2$ and $\theta \leq 120^\circ$

Eqn 5-5 was then used to evaluate the $K_{t\theta}$ values for the 12mm minor diameter dumbbells where $\frac{2h}{D} = 0.2$.

Major Diameter (mm)	Minor Diameter (mm)	Angle Of Notch	Fillet Radius (mm)	Notch Sensitivity 0% Strain $K_{t\theta}$	Notch Sensitivity 25% Strain $K_{t\theta}$	Notch Sensitivity 50% Strain $K_{t\theta}$
15	12	90º	0.75	3.043386#	2.34683*	1.696056*
15	12	90 º	0.375	3.834445#	-	-
15	12	45 º	0.75	3.130216#	-	-
15	12	45 º	0.375	3.985168#	-	-
15	12	0 º	0.75	3.11922#	-	-
15	12	0 º	0.375	4.109616#	-	-
15	9	0 º	0.75	3.093848#	-	-
15	9	0 º	0.375	4.044934#	-	-

#Values calculated from Roarks theory for notch sensitivity **[58]**
*Values of $K_{t\theta}$ calculated from ICP images, dimensions measured using AutoCAD,

Table 5-2: Notch sensitivity values calculated according to Roarks notch theory

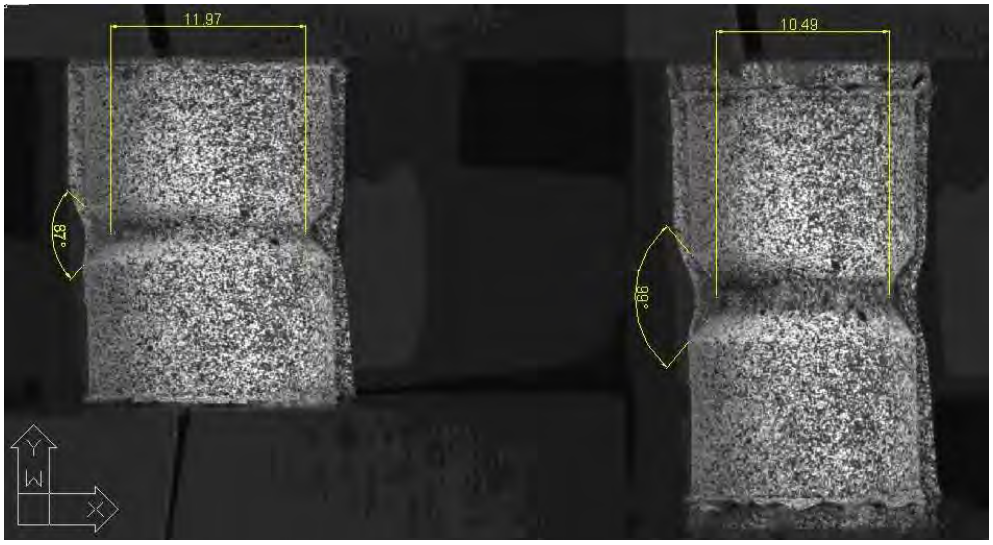

Figure 5.24: Analysis of ICP images of a dumbbell deformed to 25% strain

5.5 Calculation of the Probability of the Presence of Flaws

Probability is a measure of the likelihood that a particular event will occur, in any trial (in this case fatigue to failure experiment) carried out under prescribed conditions. The ability to predict with confidence outcomes such as the fatigue life of a component has obvious benefits in establishing service lives, setting overhaul times, improving user confidence, industrial quality control and efficient use of resources.

In a manufacturing run it would be too time consuming and hence uneconomical to subject every component produced to full inspection. It is usual, therefore to examine a sample batch of components, taken at random, as being representative of the whole output. The larger the random sample the more representative of the whole population it is likely to be.

The determination of probability may be undertaken from two approaches: Empirical or Classical. Empirical probability is based on previous known results so that the relative frequency of the number of times the event has previously occurred is taken as an indication of likely occurrences in the future. In this study of the fatigue lives of notched dumbbells, the sample size is not large enough to get a representative average of the fatigue lives of the notched dumbbells. For this reason empirical probability is not employed. However, further research is being undertaken at DIK so that empirical probability calculations can be compared to classical probability at a later stage.

Classical probability is based on a consideration of the theoretical number of ways in which it is possible for an event (a failure of a specimen) to occur.

Simplifying Assumptions

In order for the classical probability of failure to be calculated, it is necessary for some simplifying assumptions to be made in the calculation of the probability of a major flaw occurring in the critical volume of a test specimen that will give rise to crack propagation (i.e. a flaw of 200μm or greater). It is assumed that major flaws are randomly distributed throughout the volume of the test specimen.

The probabilities are calculated as percentages of the scanned volume of the specimen in the X-ray count of the flaws in the notched dumbbell.

As the specimen is large, the probability that any unit volume has a flaw, is not affected by the unit volume initially chosen. Hence the normal statistical procedure of reducing a sample by one, every time a volume of average flaw size is considered is not used here.

The work of Abraham et al **[59]** strongly suggests that failure in EPDM fatigued samples emanate from flaws of 200μm or greater. Consequently a determination of the probability of a flaw occurring in the critical area follows:

Number of particles ≥ 200μm "N" = 67

Total volume of flaws ≥ 200μm = 26.41790mm^3

Average volume of flaws of diameter ≥ 200μm = 0.39429697mm^3

Scanned volume of specimen in X-ray = 4771.2938mm^3

For calculation purposes, the X-rayed dumbbell is divided up into discrete volumes, each volume being the size of the average critical flaw (≥ 200μm) present in the sample, giving

$$\frac{x-rayed\ volume}{volume\ of\ average\ flaw}$$

$\frac{4771.2938}{0.3941} \approx 12107$ The discrete volumes or units present in the scanned dumbbell

The critical volume in a 90º notched dumbbell with a 0.75mm notch is 122.7185mm^3

This equates to ≈ 311 units in the critical section, so V_A = 4771mm = 12107 units and V_B = 122.7mm = 311 units

Hence the probability that there are no particles present in the critical section is

$$\left(\frac{V_A - N}{V_A}\right)^{V_B} \qquad \text{Eqn 5-6}$$

$$\left(\frac{12107 - 67}{12107}\right)^{311}$$

$= 0.178$

This is the probability that there will be no flaws of $\geq 200\mu m$ in the critical volume of a 90º, 0.75mm notched dumbbell. Thus, for this material and a test sample of this configuration, it can be anticipated that approximately one of every six test specimens will have a far higher fatigue life than the norm. This finding is borne out by the small number of fatigue tests carried out.

5.6 Results of Simulations of Stress Softening on Notched Dumbbell

FEA models of the notched dumbbells were prepared (as in Figure 5.25) and simulations were carried out as described in Section 4.1.2.8. Deformations of 25% integral strain were applied to the dumbbell specimens and the stress softening subroutine was applied as described in Section 4.14 and the results were plotted graphically in Figures 5.26 and 5.27.

In order to validate the FEA simulations of the notched dumbbells with the stress subroutine, physical experiments were carried out and recorded using ICP. The notched dumbbells were clamped in the Zwick tensile machine and prepared in the normal manner as described earlier in section 3.8.5. Images of a prepared specimen undergoing deformation are presented in Figure 5.24. The ICP measurements were made for both the E1M and N1M materials and the results are of the 1^{st} and 5^{th} cycles are plotted in Figures 5.26 and 5.27 along with the results of the FEA simulations including stress softening.

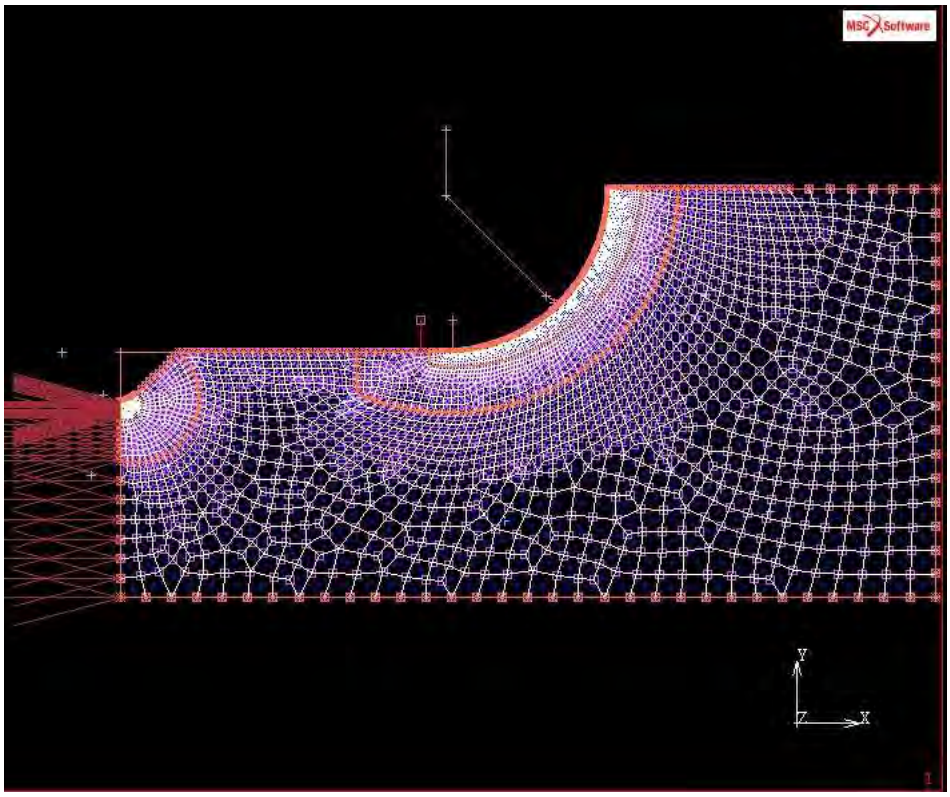

Figure 5.25: FEA model of a notched dumbbell model

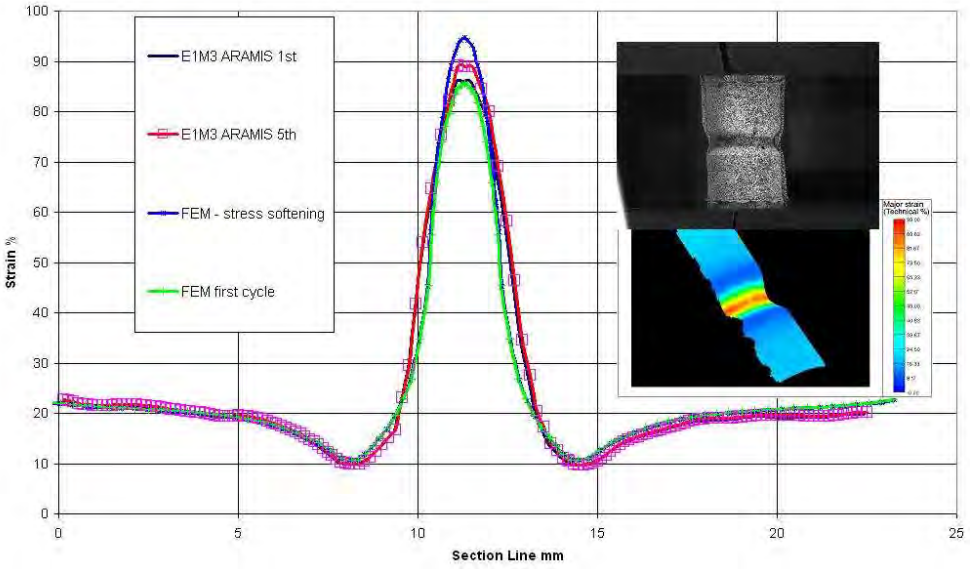

Figure 5.26: ICP measurement of an E1M specimen (with a 90° Notch, 0.75mm fillet radius at the tip and a 12mm minor diameter)

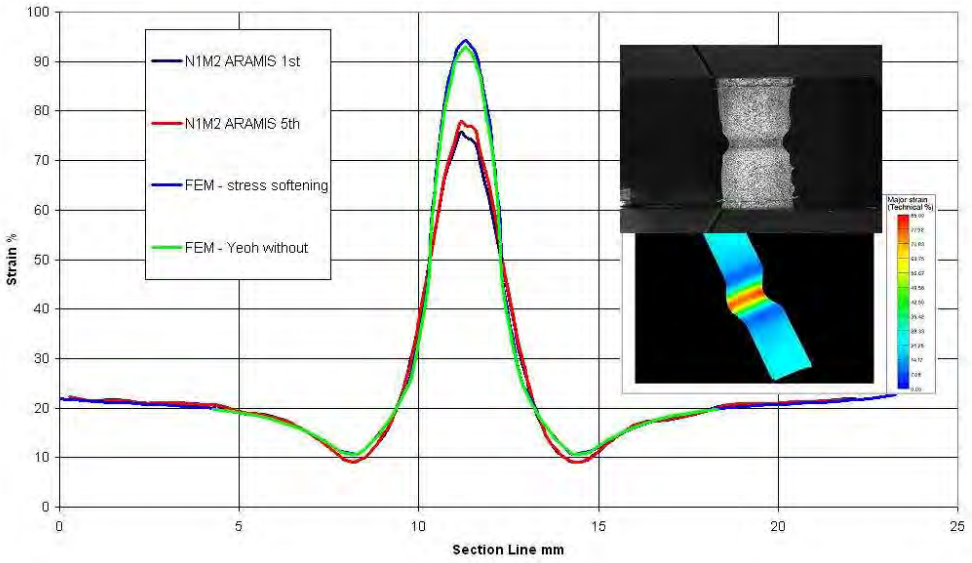

Figure 5.27: ICP measurement of an N1M specimen (with a 90° Notch, 0.75mm fillet radius at the tip and a 12mm minor diameter)

An excellent correlation was obtained between the FEA and the ICP measurements in the region away from the notches. The results for the E1M simulations displayed in Figure 5.26 had a better correlation in the region at the notch than the N1M simulation in Figure 5.27, with the stress softening subroutine over predicting the strains in the region of the notch. This may be due in part to the fact that the stress softening routine is based only on the first strain invariant I_1 and the second strain invariant I_2 is omitted.

Chaper 6 Discussion

The primary aim of this research was to provide a novel method of modelling stress softening in elastomeric materials. This has been accomplished by the creation of a subroutine in FEA which allows the variation of local material constants based on their adjustment determined from dynamic change in strain invariant I_1. Firstly the material was characterised through a series of uniaxial and equi-biaxial experiments to various values of I_1 and fittings were then made to the first and fifth stress strain cycles. Once this was completed FEA simulations of components manufactured from the material were made. The simulation process comprised of two steps. In the 1st the simulation, material properties were defined for a fitting of the 1st experimental stress-strain cycle to the maximum I_1 value. These C_{ij} coefficients defined the material properties for the entire material model as a homogenous, isotropic material. As the simulation of the 1st strain cycle was run, the 1st subroutine "Write" was implemented and this recorded the I_1 values reached for each Gauss point in the model throughout the deformation. The second simulation implemented the second subroutine "Read" which reads the I_1 values recorded for the 1st simulation and assigns new material properties for each Gauss point in the model. The new material properties were defined as a function of the previous maximum I_1 values reached in the 1st simulation. In this way the simulation defined an inhomogeneous material as cyclic deformation continued and stress softening in the material was taken into account.

To facilitate the development of the subroutine it was necessary to complete numerous tests on a range of elastomer materials with various standard

discontinuities (holes, vee notches etc.) Calculations of stress concentrations at the notches were made using accepted empirical methods and the empirical formula for static stress concentrations. Images of deformed notched specimens recorded using ICP were taken and the notch angles at various levels of λ were measured and used to calculate the change in notch sensitivity with increasing λ. A comparison was then made of the calculated and measured stress concentration values. The tensile deformation had the effect of reducing the severity of the stress concentration as the fillet radius and the notch angle increased with deformation.

Image correlation photogrammetry was uniquely developed as a tool to study strains at these discontinuities and during testing this method was improved in the following ways for use with rubber. Improvements were made in the techniques used to prepare the specimens for measurement with the use of aerosols to produce a fine random pattern to allow a more precise measurement resolution. Improved lighting techniques were used in order to reduce glare and optimise the quality of the images captured. As the accuracy of sensitivity of the ICP system detecting displacements is related to the width of the field of view of the specimen it was important to keep this as small as possible. This can create problems however as the area of interest on the specimen must remain within the field of view throughout the experiment. This makes it necessary to carefully plan measurements as they are very time consuming.

Further, the work of Abraham was extended with a detailed analysis of flaw size in typical components and samples. It is evident that larger flaws than previously

considered are responsible for many of the unforeseen early failures in rubber parts. The tests show that in EPDM materials it is probable that flaws of 200μm up to 500μm will be present in specimens or components produced on an industrial scale mixer. Calculations were carried out on the probability that one of these very large flaws would occur in a critical section of the notched dumbbell specimens that were used for the fatigue to failure experiments. According to the classical probability calculations at least one in 6 specimens can be expected to have no large flaws in the critical section of the specimen and so will last considerably longer than typical test specimens. Further tests are required however to verify this finding with empirical data.

Also a great deal of physical testing was carried out on samples with various stress softening properties and a comparison of NR and EPDM revealed that the NR and EPDM materials showed a considerable increase in fatigue life under non zero preload (Tension and Compression). This increase in fatigue life was observed when preloads were introduced for a fixed load amplitude and hence the maximum stress and strain increased. There was also a cross over of the material behaviour on the Wöhler curves where the EPDM reached a fatigue limit before the NR material and had a longer fatigue life for the same applied load. The opposite was the case above this critical point however, where the NR exhibited superior fatigue properties. In the load ranges tested, the NR material did not reach an apparent fatigue limit.

The final contribution that this study makes to the understanding and modelling of stress softening is the semi empirical equation to represent it. The formula

relating complex modulus to stress cycles for any point on the fatigue to failure curve, prior to the on-set of catastrophic failure, was obtained from fitting a logarithmic curve to the stress data. It is a simple but feasible method of predicting stress softening in dynamic testing. The complex modulus E* at any point in a test can be represented by the formula presented on page 69 in Section 3.6.

The formula was derived and verified for the E1M and N1M, EPDM and NR materials.

Chapter 7 Conclusion

Overall the research provides new knowledge in respect of the following:

A novel method for modelling stress softening in elastomeric materials was developed, through the creation of an effective subroutine to enable this phenomenon to be simulated. The subroutine can be easily implemented in standard FEA code. It allows the variation of local material constants based on their adjustment determined from dynamic change in strain invariant I_1 previously experienced by the sample material. The method is robust and could be employed for any elastomer.

The research employed ICP in a new capacity with elastomeric materials in order to verify the accuracy of the novel stress softening subroutine. In addition to this, the ICP was used to shed light on the stress concentrations in elastomers and to compare empirical formulae used to calculate the notch sensitivity of stress concentrations. This allowed the deformation of the notch to be accurately measured with increases in λ and hence show how notches become less injurious as an elastomeric component is deformed.

Improvements were made in the techniques used to prepare the specimens for measurement with a fine random pattern to allowed measurements with a high resolution. Improved lighting techniques reduced glare and optimised the quality of the images captured. Experimental preparation was optimised as the accuracy of sensitivity of the ICP system detecting displacements is related to the width of

the field of view of the specimen it was important to keep this as small as possible.

The study of flaw size built upon that of Abraham et al **[24]** and showed that a larger quantity and size of flaw exist in industrial materials than previously thought. This has important implications for understanding fatigue to failure experiments and the influence large flaws contribute to the large scatter detected in the fatigue lives of specimens with stress raisers and notches present in them. These findings are verified by classical probability calculations.

Fatigue to failure experiments gave a better understanding of the performance of a range of elastomers, their fatigue lives and how their performance crosses over at various loading conditions and how preload influences the fatigue life.

Observations of standard stress concentrations, substantiated that these are less injurious in elastomers subjected to high amplitude cyclic deformations.

The research proposed a novel and effective empirically derived formula for the prediction of complex modulus in stress cycles for any point on the fatigue to failure curve prior to the on-set of catastrophic failure. This formula was shown to be applicable to NR (N1 M) and EPDM (E1 M) samples.

Chapter 8 Future Work

There is potential for further development of the stress softening routine. Deficiencies in the prediction of strains in elastomers may be improved by the incorporation of changes in constants that include I_2 the second strain invariant, used with the James, Green, Simpson formula for example.

Further work is being carried out at DIK into the study of flaw size in compounds other than EPDM, such as NBR, SBR etc. using tomography as described in section 5.4.1. Consideration should also be give to the investigation of strain crystallisation in the vicinity of flaws using the same methods.

Further consideration of the diminution of static stress concentration with higher stretch ratios can now be carried out. In particular, the developments in the algorithms used in ICP to calculate the strains now mean that higher deformations can be measured.

The process of measuring deformations in experiments with ICP could be improved if the control of the ICP system was triggered by the displacements observed in the machine used to carry out the changes in the deformation on the elastomeric specimen.

The stress softening subroutine formulated during the research should be applied to a larger range of strain and non strain crystallising materials to see if the subroutine has general applicability.

.

The methods used by Ronan et al **[60] [61] [62]** should be explored to see if they can be employed to differentiate between the chemical and physical processes influencing stress softening during cycling. These may occur during the fatigue to failure tests due to temperature rise during cycling.

Finally, further work should be carried out to see if the semi empirical formula proposed for stress softening can be universally applied to elastomeric materials.

Glossary of Terms

- **Amorphous.** Lacking definite form, lacking distinct crystalline structure, shapeless
- **Anelastic.** Pertaining to behaviour showing no obvious relation between stress and strain
- **Carbon-black.** An amorphous form of finely divided carbon
- **Conditioning**. Straining a test-piece for a number of cycles to remove stress softening to a level where the material is considered to be at a consistent level of rigidity
- **Crosslink density.** The average molecular weight or mass between crosslink points
- **Dynamic modulus.** Complex modulus of material under dynamic shear loading. It is equal to the sum of static shear modulus and loss modulus
- **Elasticity.** Ability of a material to return to its original shape when the load causing deformation is removed
- **Empirical.** Relying on or derived from observation or experiment
- **Entropy.** A measure of disorder or randomness
- **Hardness.** Measure of a materials resistance to localised plastic deformation. Most hardness tests involve indentation, but hardness may be reported as resistance to scratching (file test), or rebound of a projectile bounced off the material
- **Hookean.** Conforming to Hooke's Law that describes a linear relationship between stress and strain
- **Hyperelasticity.** The property of being capable of exhibiting highly reversible deformations

- **Macroscopic.** Large enough to be perceived or examined by the unaided eye
- **Modulus**. Used alone generally refers to tensile modulus of elasticity. Shear modulus can be determined by plane or torsional shear testing and for both the term modulus of rigidity is used
- **Strain.** Change per unit length in a linear dimension of a part or specimen, often expressed in %. Strain as used with most mechanical tests is based on original length of the specimen
- **Stress.** Load on a specimen divided by the area through which it acts. As used with most mechanical tests, stress is based on original cross section area without taking into account changes in area due to applied load. This sometimes is called conventional or engineering stress. True stress is equal to the load divided by the instantaneous cross sectional area through which it acts
- **Stress relaxation.** Decrease in stress in a material subjected to prolonged constant strain at a constant temperature. Data often is presented in the form of a stress vs. time plot. Stress relaxation rate is the slope of the curve at any point
- **Viscoelasticity.** Exhibiting time dependent behaviour. The property of a viscous material that also shows elasticity
- **Vulcanisation.** The process of forming crosslinks between long chain molecules by chemical reaction, achieved by heating rubber in the presence of sulphur and/or other reagents

References

1. GOM Optical Measuring Techniques GmbH, “Manual for deformation measurement using the grating method”, ARAMIS 4.7 Pg. 25, Braunschweig, 2001.

2. J.P. Berry, “Fracture of non-metals and composites”, Fracture: An Advanced Treatise, Vol. 7, Ch. 2, Academic Press, New York, 1972.

3. A.N. Gent, “Strength of elastomers”, Science and Technology of Rubber, Pg. 422, Academic Press, 1978.

4. F. Tabaddor, “Elastic stability of rubber products”, Rubber Chemistry and Technology, Vol. 60, Pg. 957-965, 1988.

5. L. Mullins, “Softening of rubber by deformation” Rubber, Chemistry and Technology, Vol. 42. Pg. 339, 1969.

6. T. Alshuth and F. Abraham, “Strategies to predict dynamic properties of elastomer products”, Deutsche Kautschuktagung (DKT) 2000, Nürnberg, Sept. 2000.

7. M. Klüppel et al, “Impact of pre-strain on dynamic-mechanical properties of carbon black and silica filled rubbers”, European Conference on Constitutive Models for Rubber (ECCMR), London, Sept. 2003.

8. A.R. Payne, “The dynamic properties of carbon black loaded natural rubber vulcanizates part 1” Rubber, Chemistry and Technology, Vol. 36, Pg. 432, 1963.

9. A.R. Payne, “The dynamic properties of carbon black loaded natural rubber vulcanizates part 2” Rubber, Chemistry and Technology, Vol. 36, Pg. 444, 1963.

10. L.R.G. Treloar, “The physics of rubber elasticity” 3rd Edition, Oxford University Press.

11. A.G. James et al, “Strain energy functions of rubber, 1: characterisation of gum vulcanisates”, Journal of Applied Polymer Science, Vol. 19, Pg. 2033-2058, 1975.

12. R.W. Ogden, “Large deformation isotropic elasticity: on the correlation of theory and experiments for incompressible rubber like solids”, Proceedings of the Royal Society, Vol. A, Pg. 556, 1992.

13. D.W. Nicholson, N.W. Nelson, “Finite element analysis in design with rubber”, Rubber, Chemistry and Technology Vol. 63 Pg. 394, 1990.

14. R.H. Finney, “Finite element analysis”, Engineering with Rubber 2nd edition, Pg. 267-276, Hanser, 2001.

15. A.G. Thomas, "Rupture of Rubber, II. The strain concentration at an incision", Journal of Polymer Science, Vol. 18, Pg 177, 1955.

16. M.D. Ellul, “Mechanical fatigue” (Chapter 6), Engineering with Rubber A.N. Gent, Hanser, 2001.

17. W.D. Pilkey, “Peterson’s stress concentration factors”, 2nd Edition, Wiley and Sons,1997.

18. W.C. Young, R.G. Budynas, “Roark’s formulas for stress and strain”, 7th Edition, McGraw-Hill, 2002.

19. M. Takano, “The notch sensitivity of polymeric materials”, Journal of Applied Polymer Science, Vol. 20, Pg. 2193, 1976.

20. C.F. Balazs, “Mechanical design and notch sensitivity of moulding materials”, American Society of Mechanical Engineers (ASME), Winter Annual Meeting, New York, 1964.

21. R. Prabhakaran, “Notch sensitivity of polymers” Journal of Applied Polymer Science, Vol. 22, Pg. 3011, 1978.

22. F. Abraham, “The influence of glass spheres as model flaws on fatigue life and dynamic crack propagation of elastomers” Kautschuk Herbst Kolloquium (KHK), Hannover, 2004.

23. F. Abraham, “Testing and simulation of the influence of glass spheres on fatigue life and dynamic crack propagation of elastomers” European Conference on Constitutive Models for Rubber *(*ECCMR), Stockholm, 2005.

24. MTS Systems Corporation, TestStar^{TM} II Control System (manual) 790.31, Nov. 1996.

25. F. Abraham, “The influence of minimum stress on the fatigue life of non strain-crystallising elastomers”, PhD Thesis, Coventry University, Dec. 2002.

26. A. Le Gal “Investigation and modelling of rubber stationary friction on rough surfaces”, PhD Thesis, Leibniz Universität Hannover, 2007

27. K. Galanulis, A. Hofmann, “Determination of forming limit diagrams using an optical measurement system”, Proceedings of Sheetmet ‘99, Braunschweig, Germany, Oct. 1999.

28. T. Tyson et al, “Biomechanics deformation and strain measurements with 3D image correlation photogrammetry”, Experimental Techniques, Vol 26 No 5, Pg 39-42, Sept. /Oct. 2002.

29. Jenoptik AG, http://www.jenoptik.com/en_40150_thermographic_ Cameras, (Accessed 2011).

30. J. Mc Namara, T. Alshuth, S. Jerrams, “An investigation of thermal build-up in elastomeric specimens fatigue tested to failure”, Kautschuk Herbst Kolloquium, Hannover, Pg. 145 , Nov. 2008.

31. International Standards Organisation, ISO Standard 37: (1994). http://www.iso.org/iso/home.html.

32. F. Abraham, T. Alshuth, S. Jerrams, Poster: “Dependence of fatigue life of elastomers on stress amplitude and pre-stress”, Kautschuk Herbst Kolloquium, Hannover, DIK, Nov. 2000.

33. T. Alshuth, J. Mc Namara, R.H. Schuster, “Fatigue properties of elastomer materials”, Forschungsvereinigung Antriebstechnik (FVA) Project 438, 2005.

34. S. Jerrams, et al, “The effects of strain rate and hardness on the material constants of nitrile rubbers”, Journal of Materials and Design, Vol. 19 No. 4, Aug. 1998.

35. International Standards Organisation, ISO Standard 7618, http://www.iso.org/iso/home.html.

36. R.H. Finney, “Material specification” (Chapter 9.2), Engineering with Rubber, A.N. Gent, Hanser, 2001.

37. British Standards Institute, BS 903, Methods of testing vulcanised rubber Part 19 (1950) and Part A7 (1957).

38. H.J. Qi et al, “Durometer hardness and the stress-strain behavior of elastomeric materials”, Rubber Chemistry and Technology, Vol. 76 (2), Pg.. 419-435, 2003.

39. Infratec GmbH, http://www.infratec.de/en/thermography/thermographic-software/irbis-3-analysis-software.html. (Accessed 2011)

40. J.D. McNamara, “Investigation of heat build up in elastomer specimens under deformation using shortwave thermography”, Deutsche Institut für Kautschuktechnologie (DIK), (internal presentation), Aug. 2005.

41. R. Seldén, “Fracture mechanics analysis of fatigue of rubber - a review” Progress in Rubber and Plastics Technology, Vol. 11, No 1, The Institute of Materials/RAPRA, 1995.

42. E.M. Mikahil, et al, “Introduction to modern photogrammetry”, John Wiley and Sons, 2001.

43. J. Tyson et al, “Advanced photogrammetry for robust deformation and strain measurement”, Proceedings of the 2002 SEM annual conference and exhibition of experimental and applied mechanics, Jun. 2002.

44. T. Schmit et al, “Full-field dynamic displacement and strain measurement using advanced 3D image correlation photogrammetry”, Experimental Techniques, Vol. 27, Pg. 47, Part May/Jun. 2003.

45. MTS Systems Corporation 2010, “Elastomer Testing” (http://www.mts.com/ucm/groups/public/documents/library/dev_005077.pdf). (Accessed 2011)

46. R.S. Rivlin and A.G. Thomas, “Rupture of rubber. I. characteristic energy for tearing.”, Journal of Polymer Science, Vol. 10., No. 3. Pg. 291, 1953.

47. O.H. Yeoh, “Characterisation of elastic properties of carbon-black-filled rubber vulcanizates”, Rubber Chemistry and Technology Vol. 63, Pg. 792, 1990.

48. S. Shepherd and R. Shorter, MSc Research Programme, “Drive shaft boot modelling and analysis”, Coventry University, 1998.

49. R. Johannknecht, “Behaviour of elastomers in physical tests and computer simulated finite element analysis”, PhD thesis, Coventry University, 1999.

50. R. Johannknecht, S.J. Jerrams, G. Clauss, “The uncertainty of implemented curve fitting procedures in finite element software”, Finite Element Analysis of Elastomers, Professional Engineering Publications LTD, 1998

51. Marc® 2007 r1 Volume B: Element Library (support manual).

52. G.A. Holzapfel, “Nonlinear solid mechanics”, John Wiley and Sons, 2001.

53. O.H. Yeoh, “Some forms of the strain energy function for rubber”, Rubber. Chemistry and. Technology, Vol. 66, Pg 754, 1993.

54. J. Meier, F. Huls, J. Mc Namara, “Zur beschreibung der spannungserweichung in elastomeren”, Kautschuk Herbst Kolloquium, Hannover, Pg. 61, Nov. 2008.

55. F. Abraham et al, “Investigation and simulation of the influence of flaws on the cut growth resistance and the fatigue of elastomers”, Kautschuk Gummi und Kunststoffe, Nov. 2005.

56. A.N. Gent et al, “Cut growth and fatigue of rubbers. I. The relationship between cut growth and fatigue” Rubber Chemistry and Technology, Vol. 38, Pg. 292, 1965.

57. J. Mc Namara, S. Jerrams, T. Alshuth, S. Robin, “New insights into the distribution and size of flaws in rubber compounds produced by commercial processes”, Materials Ireland, Dublin, 2010.

58. W.C. Young, and R.G Budynas, “Roark’s formulas for stress and strain”, McGraw-Hill, 2002.

59. F. Abraham, “Definition and use of an effective flaw size for the simulation of elastomer fatigue”, European Conference on Constitutive Models for Rubber (ECCMR), Sept. 2011.

60. S. Ronan, “A novel approach to predicting the lifetime of elastomers undergoing stress relaxation”, PhD Thesis, Dublin Institute of Technology, Sept. 2009.

61. International Standards Organisation, ISO 11346:2004 “Rubber vulcanised or thermoplastic – Estimation of lifetime and maximum temperature of use from an Arrhenius plot”.

62. M.L. Williams et al “The temperature dependence of relaxation mechanisms in amphorus polymers and other glass forming liquids” Journal of the American Chemical Society, Vol. 77, Pg. 3701, 1955.

Appendices

Appendix 1 – Short wave thermography cameras specifications

Appendix 2 – Published papers relevant to the research

Appendix 3 – Indentor measurements using photogrammetry

Appendix 4 – Dynamic mechanical thermal analysis (DMTA)

Appendix 5 – Double shear sandwich tests (DSST)

Appendix 1 – Short wave thermography specifications

Detector resolution	256 x 256 pixels
Spectral sensitivity	3.4…5.0 µm
Temperature measurement range	-25˚C…+ 1200˚C
Thermal resolution	<0.1˚C
(30˚C object temperature)	
Field of view	14˚ x 14˚
Geometrical resolution	1.0 mrad
Minimum object distance	0.4 m…∞
Maximum image rate	50 Hz

Table A1-1: Thermography camera specifications

Appendix 2 – A list of published papers relevant to the research

1. "Effect of slats, three mat types and out-wintering pads on performance, physiological, immunological and behavioural responses of finishing beef steers" (B. Earley, J. Mc Namara, S. Jerrams) work in progress with Teagsc for Irish Journal of Agricultural and Food Research, 2011.

2. “Effect of slats, two mat types (EasyFix and Irish Custom Extruders) and Wood-chip (on slats) on performance, physiological, immunological and behavioural responses of finishing beef steers” (B. Earley, J. D. McNamara, S. Jerrams) work in progress with Teagsc for Irish Journal of Agricultural and Food Research, 2011

3. “New insights into the distribution and size of flaws in rubber compounds produced by commercial processes” J. Mc Namara, T. Alshuth, S. Robin, S Jerrams, Materials Ireland 2010

4. "Accurate prediction and modelling of localised stress concentration“ (J. Mc Namara, T. Alshuth, J. Meier) Tire Technology Expo, Germany, February 2010

5. "Development of a vessel mimicking material for use in anatomical flow phantoms" (J. McNamara, D. King, J. Browne) Annual Scientific Meeting of the Association of Physical Scientists in Medicine, February 2009

6. "An investigation of thermal build-up in elastomeric specimens fatigue tested to failure" (J. McNamara, T. Alshuth, S. Jerrams) 8th Fall Rubber Colloquium, Germany November 2008

7. "Zur Beschreibung der Spannungserweichung in Elastomeren" (Jens Meier, Felipe Hüls, John Mc Namara) 8th Fall Rubber Colloquium, Hannover November 2008

8. "Improving the prediction of stress softening in rubber components" (J. McNamara, T. Alshuth, S. Jerrams) Kautschuk Gummi Kunststoffe, Germany December 2007

9. "Finite element calculation and experimental determination of local softening of elastomers" (J. McNamara, T. Alshuth, S. Jerrams) IRC (International Rubber Conference) Lyon May 2006

10. "Improving elastomeric finite element analysis by modelling local strains obtained from photogrammetry" (J. D. Mc Namara, Dr. T. Alshuth, Dr. S. Jerrams**, N. Murphy**) MED 06 (Materials Engineering and Design) Dublin, March 2006

11. "3D image correlation photogrammetry ~ A tool for determining the physical properties of elastomers" (T. Alshuth, J. McNamara, R. Granier, S. Jerrams, N. Murphy) presentation to SENAI-CETEPO (Centro Tecnologico de Polimeros), Sao Leopoldo, Rio Grande de Sul, Brazil, April 2005

12. "A comparison of local strains in elastomer specimens using 3D image correlation photogrammetry and finite element analysis" (J McNamara, T. Alshuth, S. Jerrams) 10th International Macromolecular Colloquium, Gramado, Brazil, April 2005

13. "Evaluation of local strains in elastomer specimens using 3D image correlation photogrammetry" (J. McNamara, T. Alshuth, S. Jerrams) 10th International Seminar of Elastomers ISE 2005, Rio de Janeiro, Brazil, April 2005

14. "Evaluation of local strains in elastomer specimens using 3D image correlation photogrammetry" (T. Alshuth, J. McNamara, R. Granier, S. Jerrams, N. Murphy) KHK 2004 (Kautschuk Herbst Kolloquium), Hannover, Germany, Nov 2004.

Appendix 3 – Indentor measurements using photogrammetry

Further measurements have been carried out to complement friction measurements research conducted in DIK. See Figures A.3.6 to A.3.6 The experiments involved the pressing on an indentor into a rubber surface with a load of 30N to obtain data in respect of the strain gradient in the area of deformation around the area of contact with the indentor. Further measurements to support this study will be carried out with two or more indentors in close proximity to each other to investigate how the strain fields overlap.

A load of 30N was applied which resulted in an initial indentor insertion depth of 1.2mm

Figure A.3.1: Indentor pressing on the rubber surface

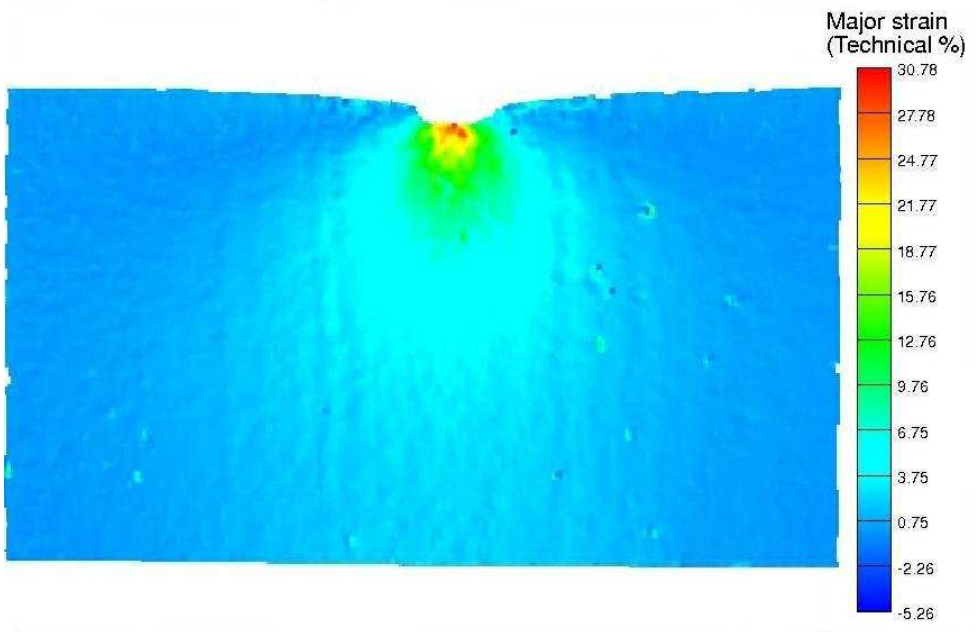

Figure A.3.2: Measured strain gradient from the indentor pressing on the rubber surface

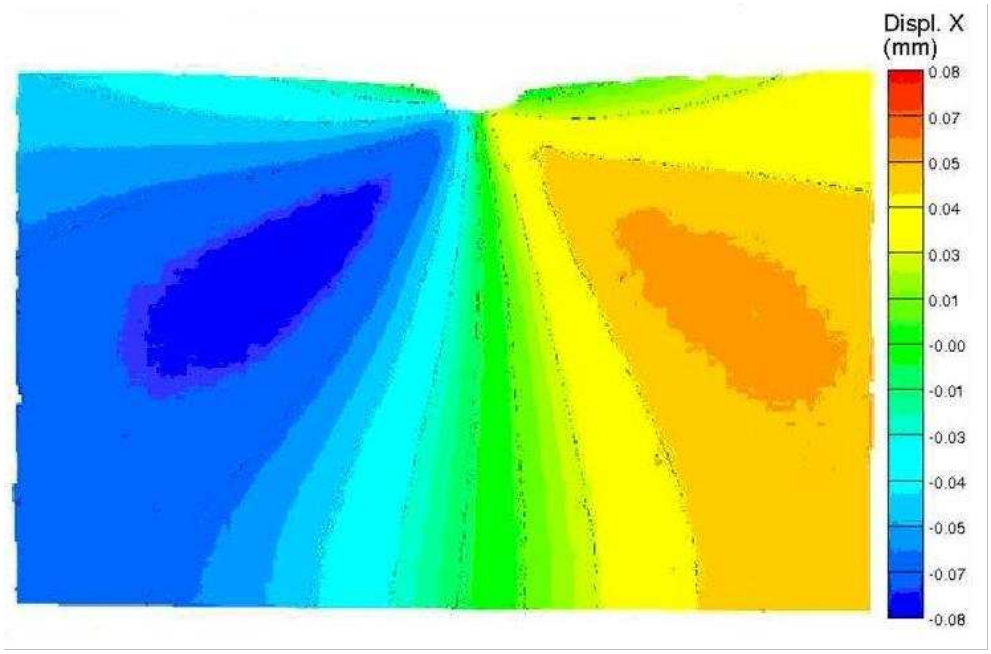

Figure A.3.3: ICP measurement showing displacement in the X direction

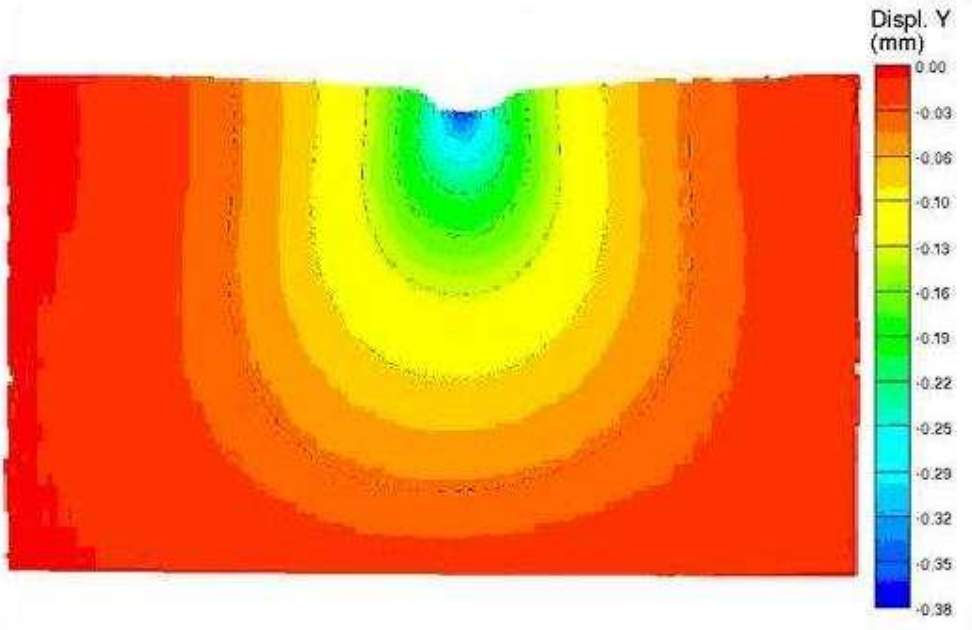

Figure A.3.4: ICP measurement showing displacement in the Y direction

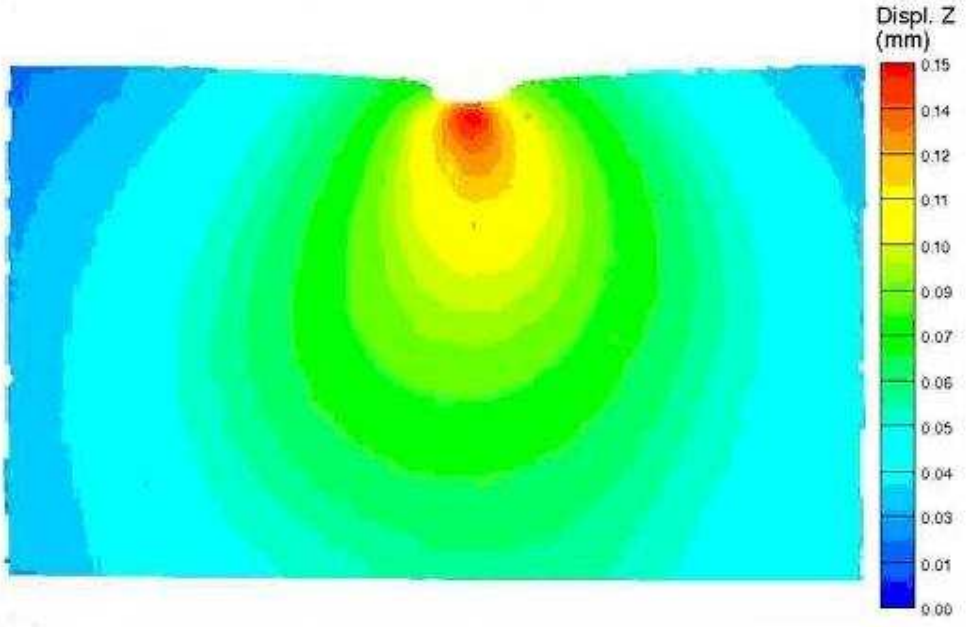

Figure A.3.5: ICP measurement showing displacement in the Z direction

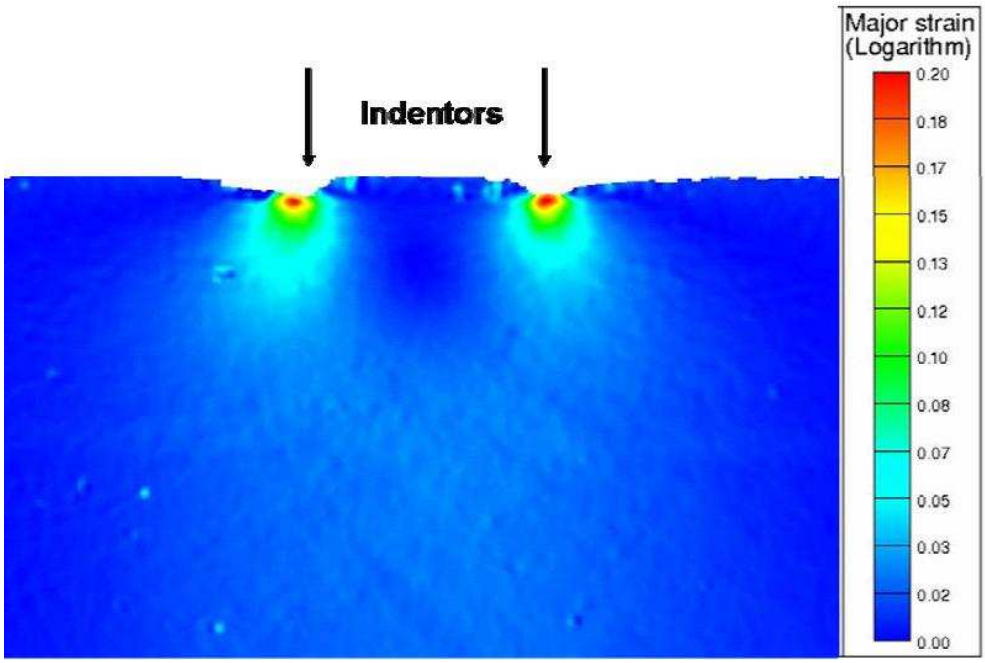

Figure A.3.6: Double indentors pressing on the a rubber pad

Appendix 4 – Modified SEN with central hole

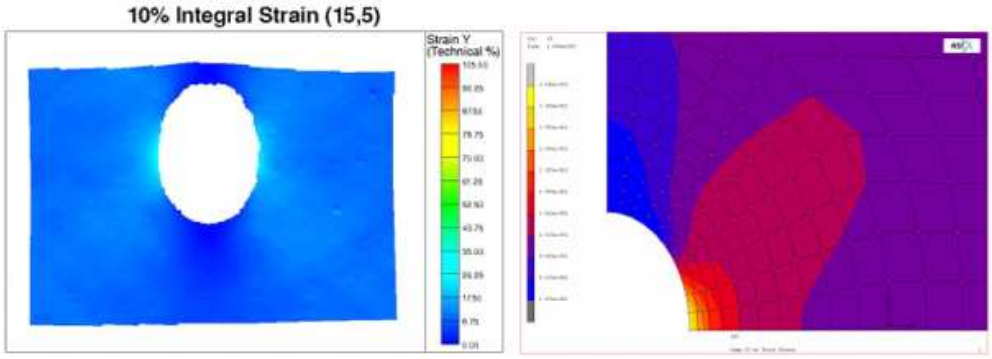

Figure A.4.1: ICP measurement and FEA calculated strains for specimen at 10% integral strain

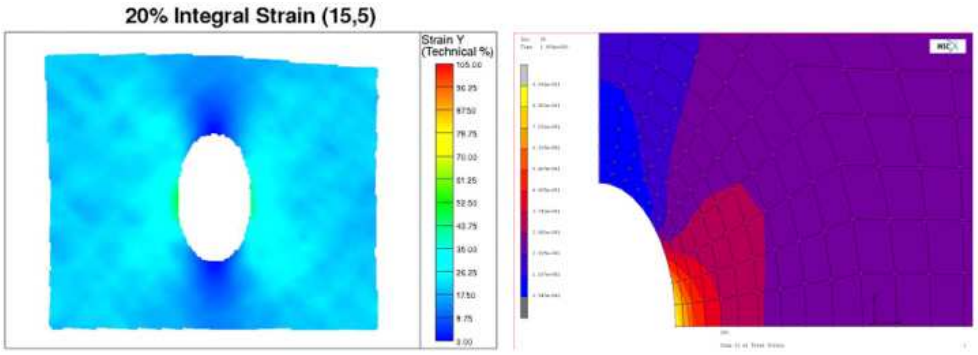

Figure A.4.2: ICP measurement and FEA calculated strains for specimen at 20% integral strain

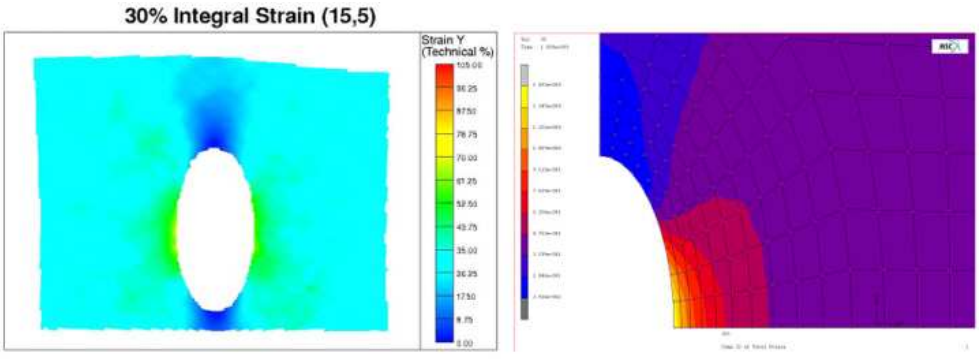

Figure A.4.3: ICP measurement and FEA calculated strains for specimen at 30% integral strain

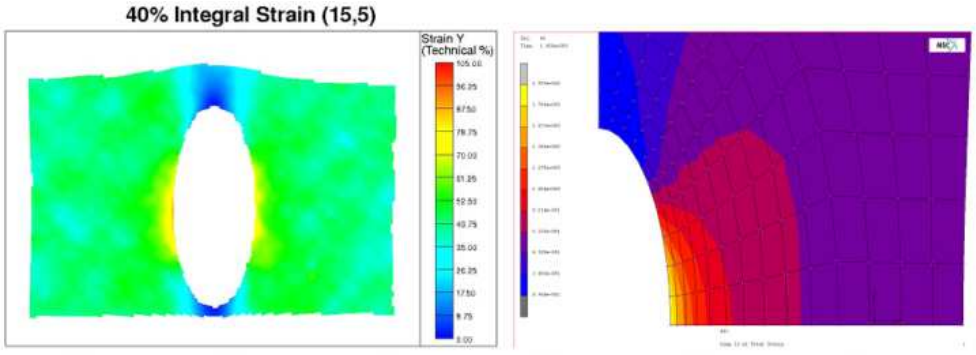

Figure A.4. 4: ICP measurement and FEA calculated strains for specimen at 40% integral strain

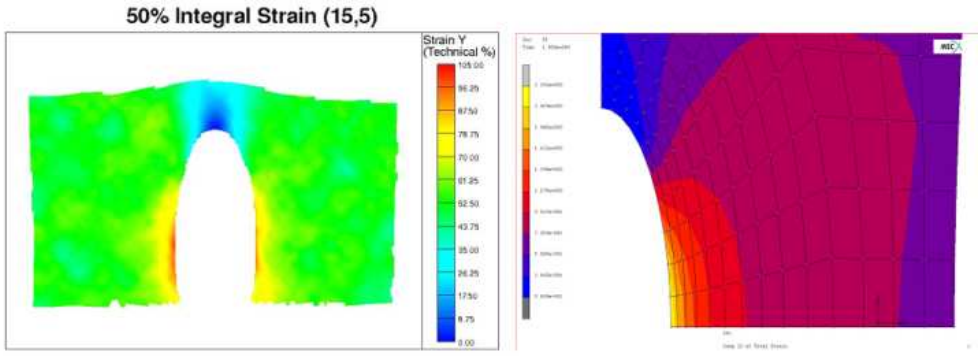

Figure A.4. 5: ICP measurement and FEA calculated strains for specimen at 50% integral strain

Integral Strain	ICP	FEA
10%	30%	31%
20%	55%	66%
30%	75%	94%
40%	98%	119%
50%	105%	132%

Table A.4-1: Correlation between ICP and FEA for the hole in planar specimen

Appendix 5 – Modified SEN with 90°Vee notch

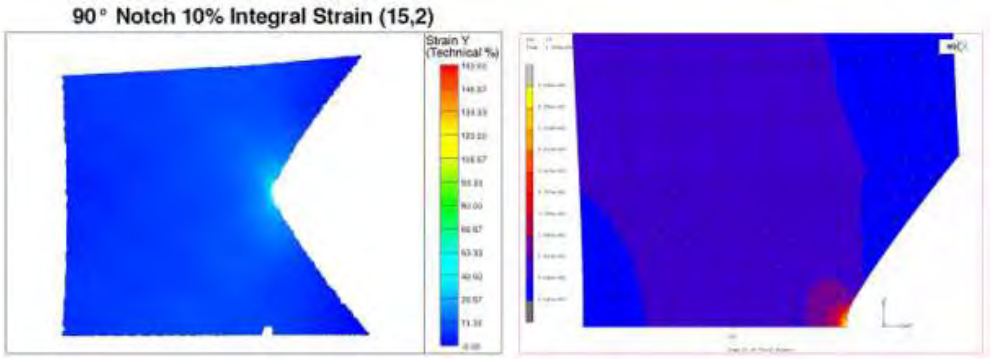

Figure A.5.1: ICP measurement and FEA calculated strains for Vee notched specimen (10% integral strain. ICP max value 58%, MARC max value 67%)

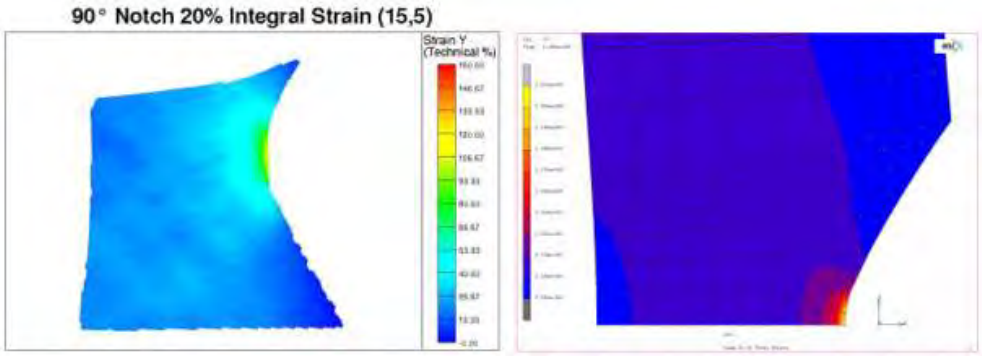

Figure A.5.2: ICP measurement and FEA calculated strains for V notched specimen (20% integral strain. ICP max value 115%, MARC max value 123%)

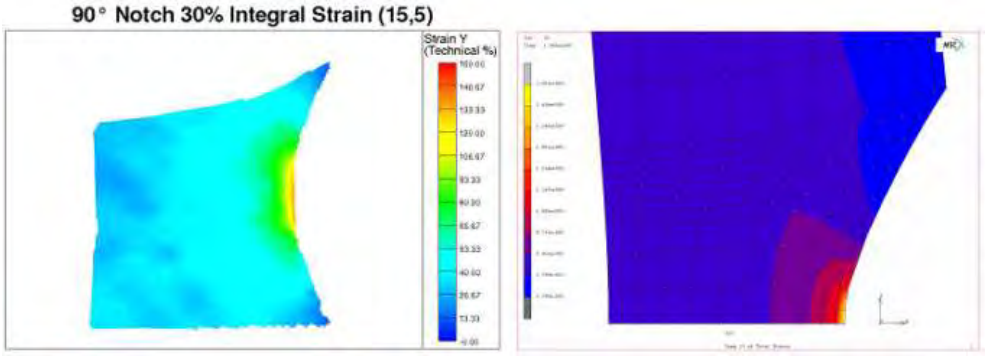

Figure A.5.3: ICP measurement and FEA calculated strains for V notched specimen (30% integral strain. ICP max value 140%, MARC max value 148%)

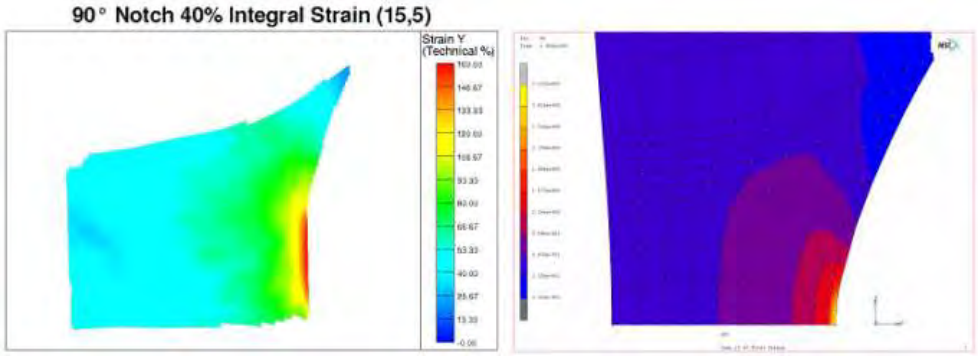

Figure A.5.4: ICP measurement and FEA calculated strains for V notched specimen (40% integral strain. ICP max value 160%, MARC max value 169%)

Integral Strain	ICP	FEA
10%	58%	67%
20%	115%	123%
30%	140%	148%
40%	160%	169%

Table A.5-1: 90° V notch specimen ICP compared to FEA (all values in engineering strain)

Appendix 6 – Dynamic mechanical thermal analysis (DMTA)

The dynamic thermal analysis is a very useful test as it gives an insight into the behaviour of the material at different temperatures and can be adapted to carry out frequency as well as temperature sweeps which can be used to extrapolate the high frequency behaviour of the material. These results are useful for friction applications.

The experiments are carried out on an ARES Fa. Rheometric Scientific. A flat 2mm strip of material measuring 40x20mm is held between the clamps in a termperature chamber while subjected to torsional deformation of 0.5% at a frequency of 1Hz. The temperature is then varied incrementally from -80°C to 120°C at a rate of 1°C/minute.

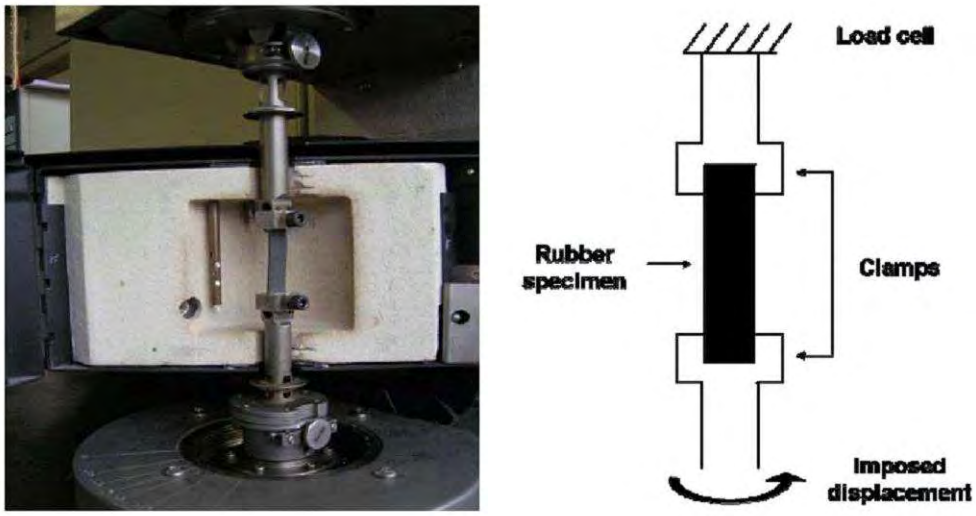

Figure A.6.1: Experimental setup of the ARES DTMA

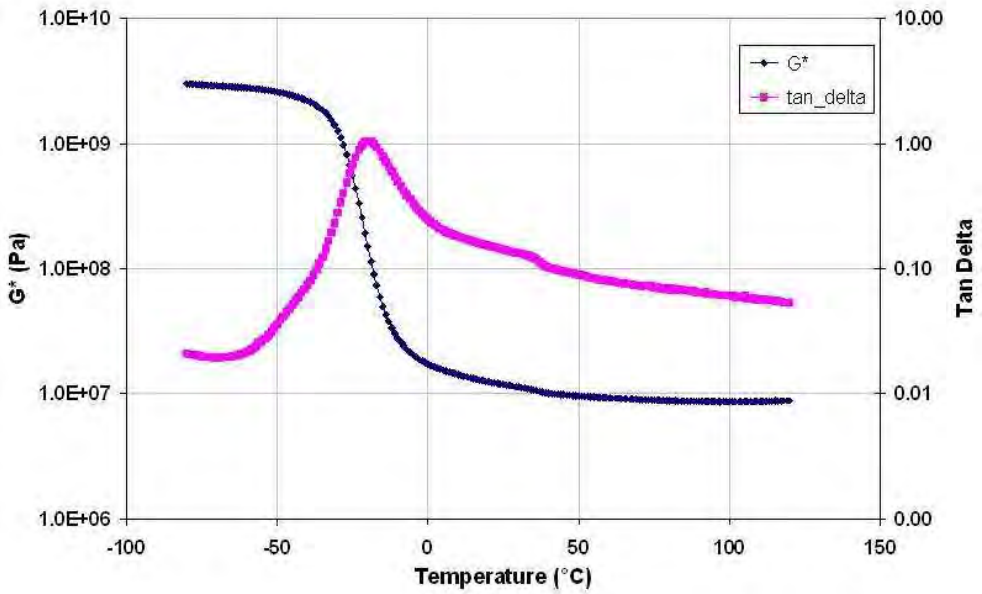

Figure A.6.2: NB P DTMA from -80 to 120°C at 1Hz using a load of 2N 0.5%

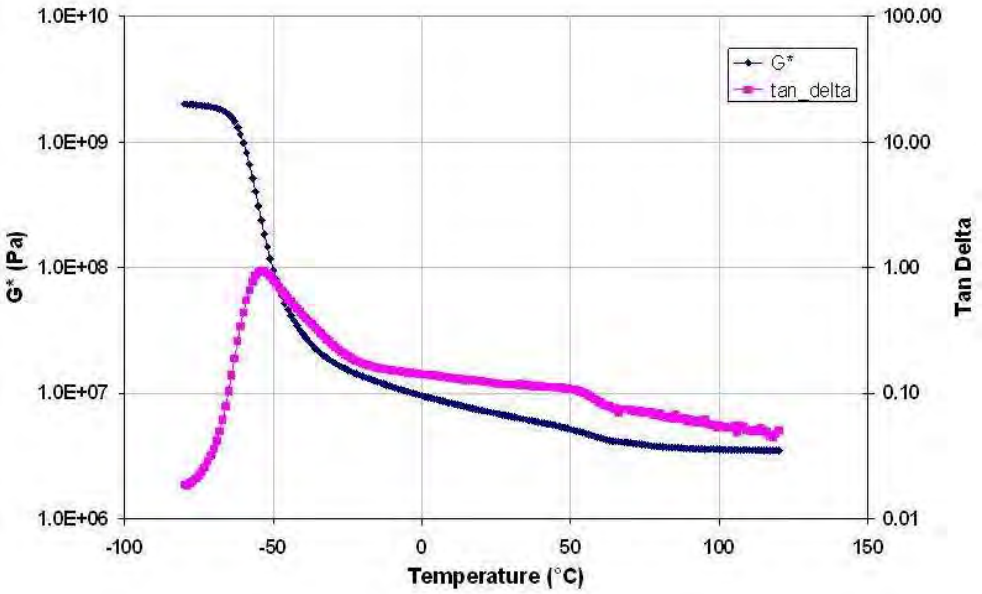

Figure A.6.3: N2 P

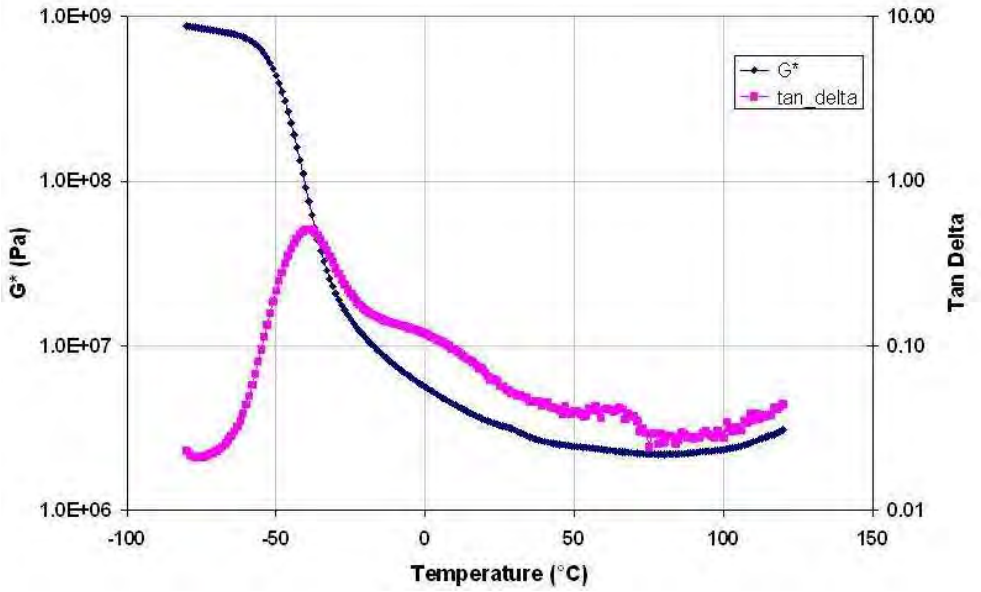

Figure A.6.4: E1 M

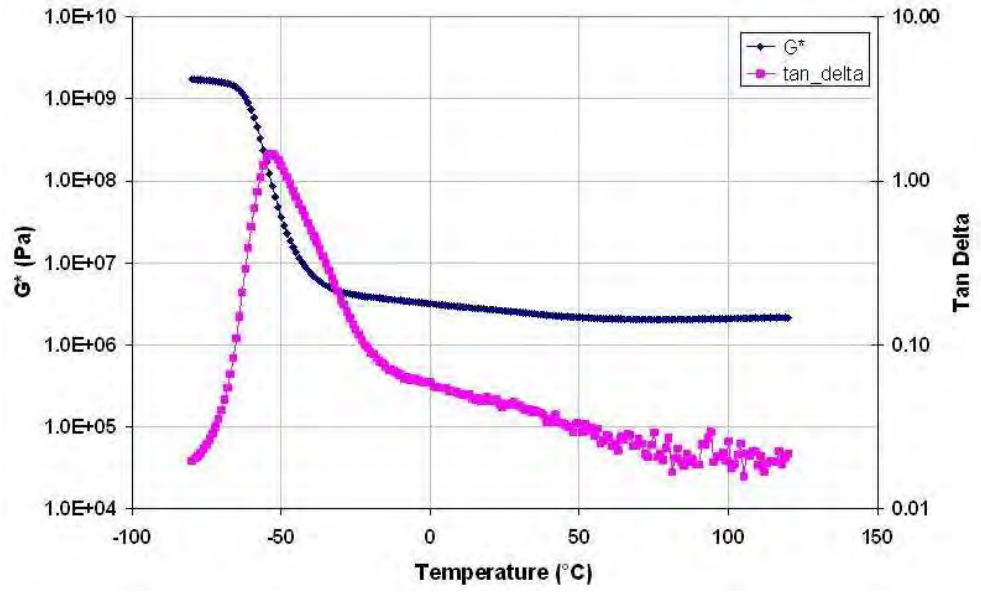

Figure A.6.5: N1 M

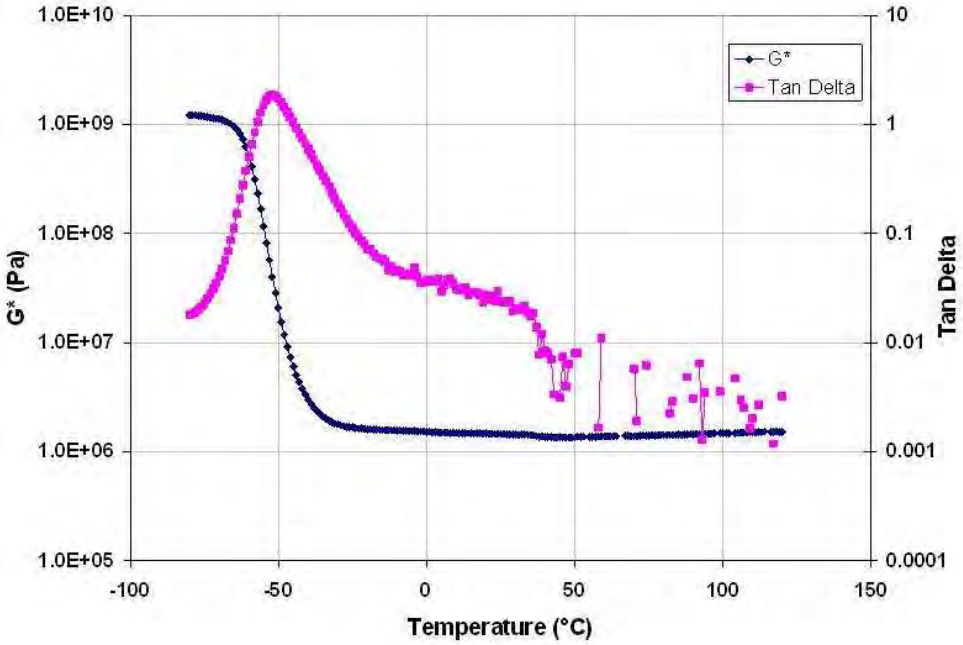

Figure A.6.6 N3 P

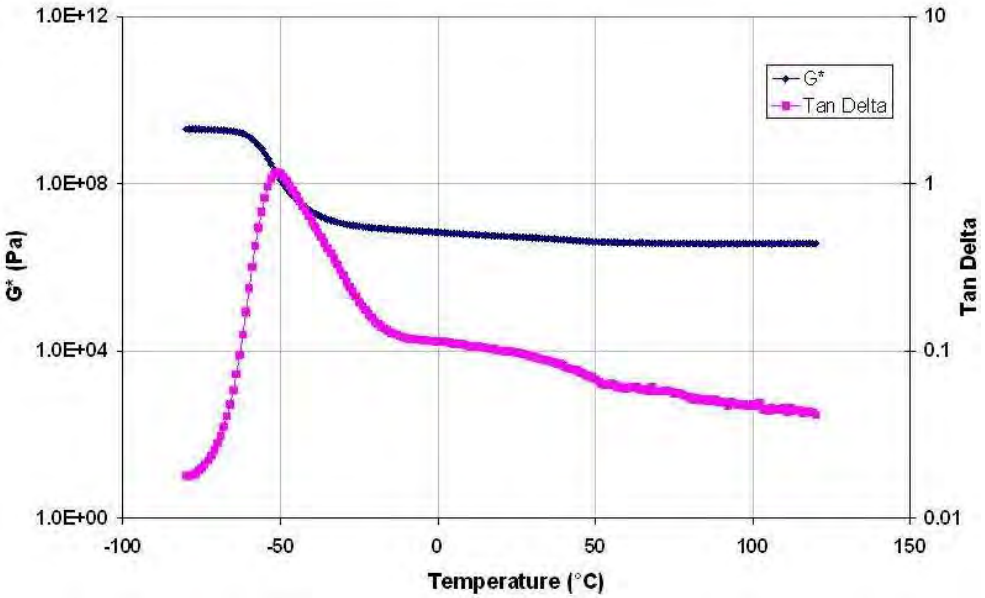

Figure A.6.7: N1 P

Appendix 7 – Double shear sandwich tests (DSST)

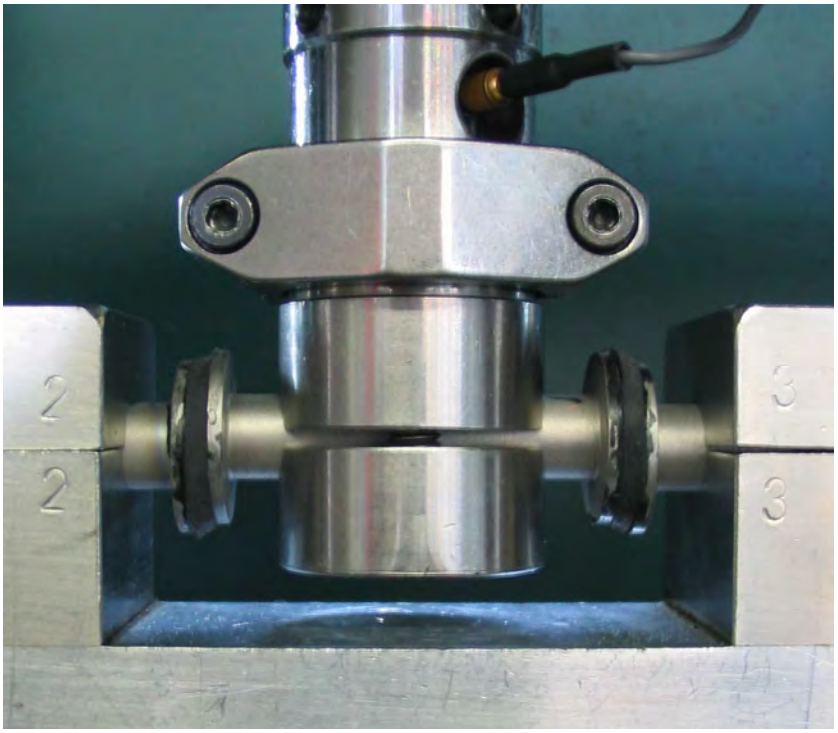

Figure A.7.1: Double shear sandwich experimental arrangement

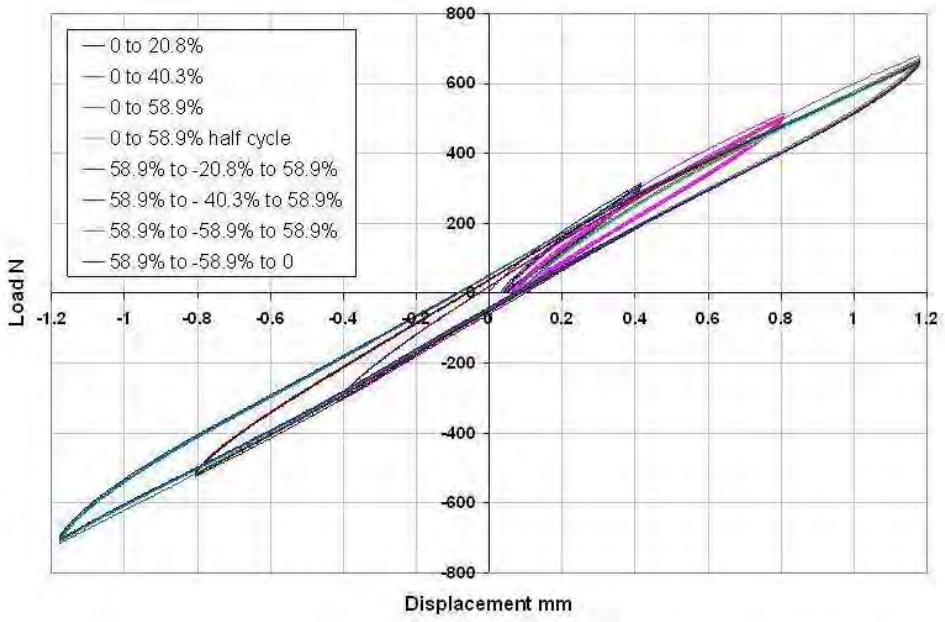

Figure A.7.2: NBP double shear sandwich

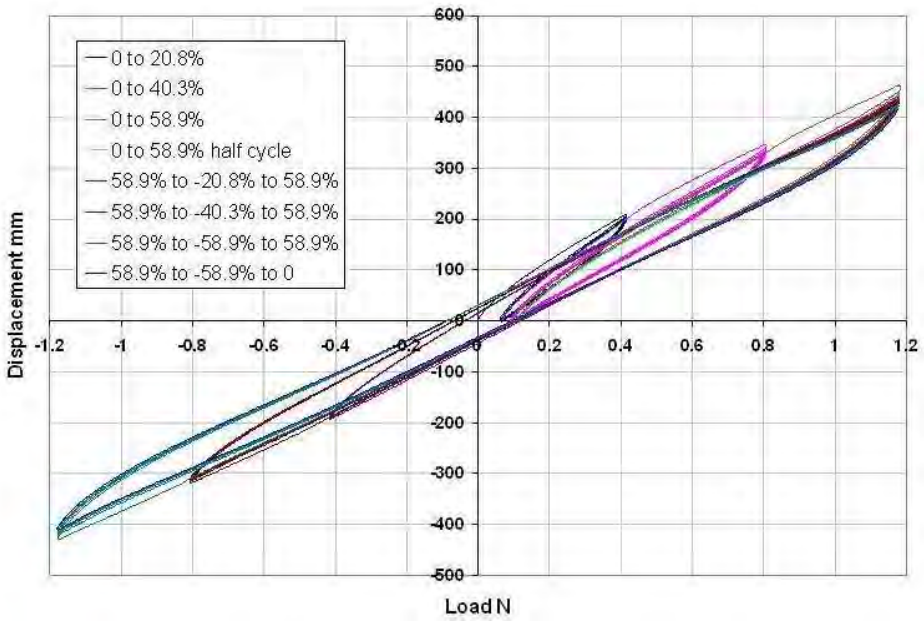

Figure A.7.3: N2 P Double shear sandwich

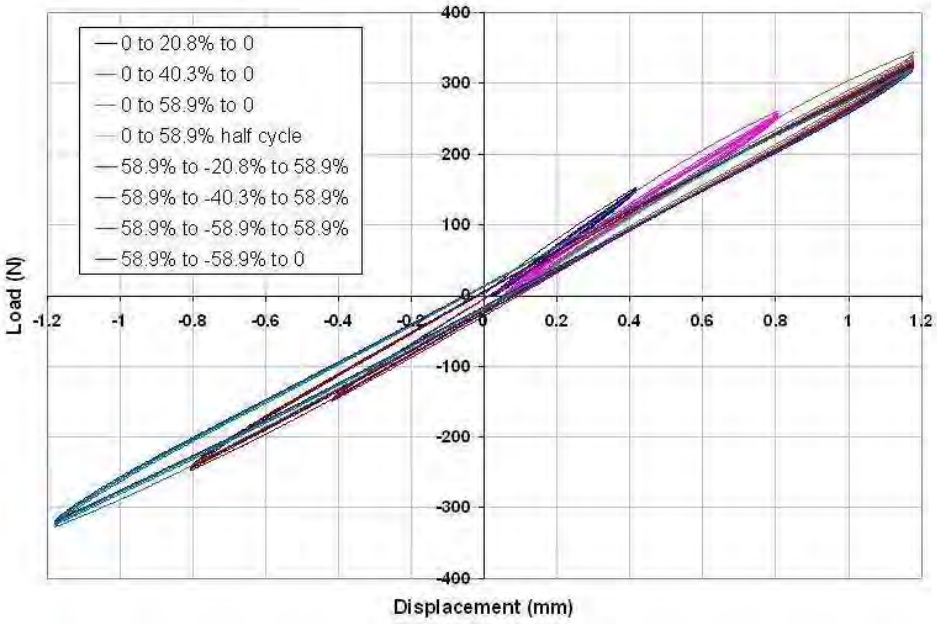

Figure A.7.4: E1 M Double shear sandwich

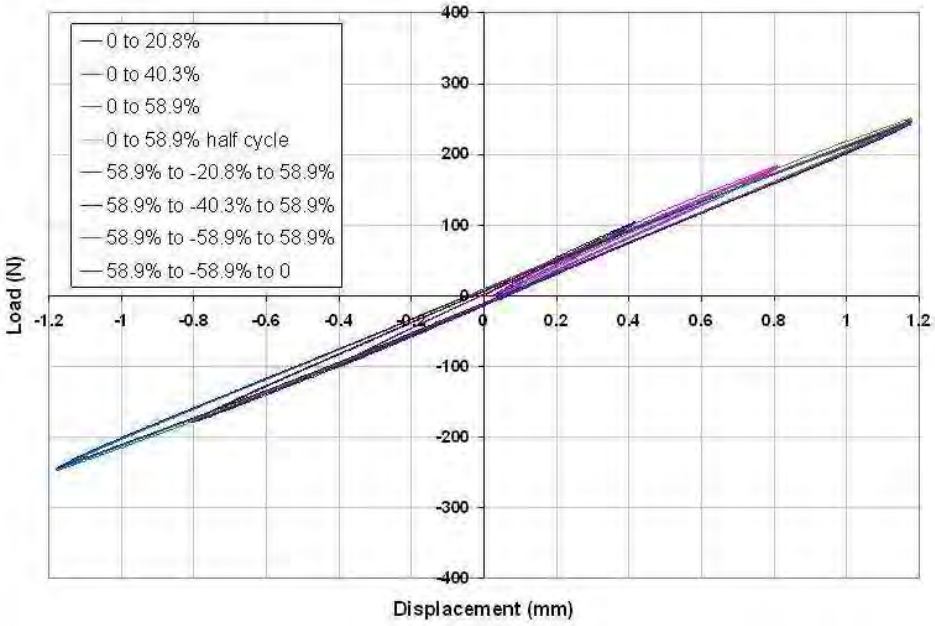

Figure A.7.5: N1 M double shear sandwich

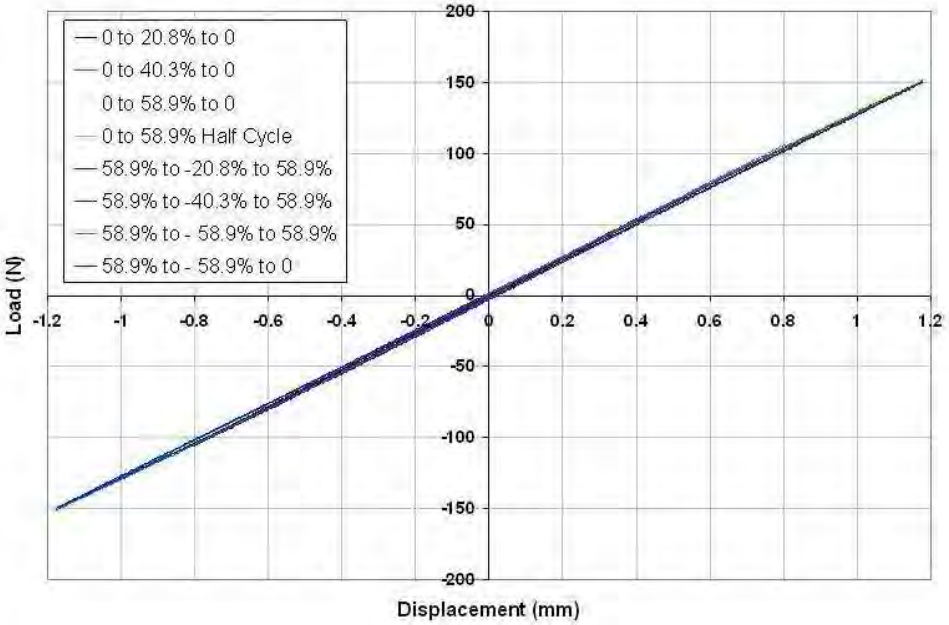

Figure A.7.6: N3 P

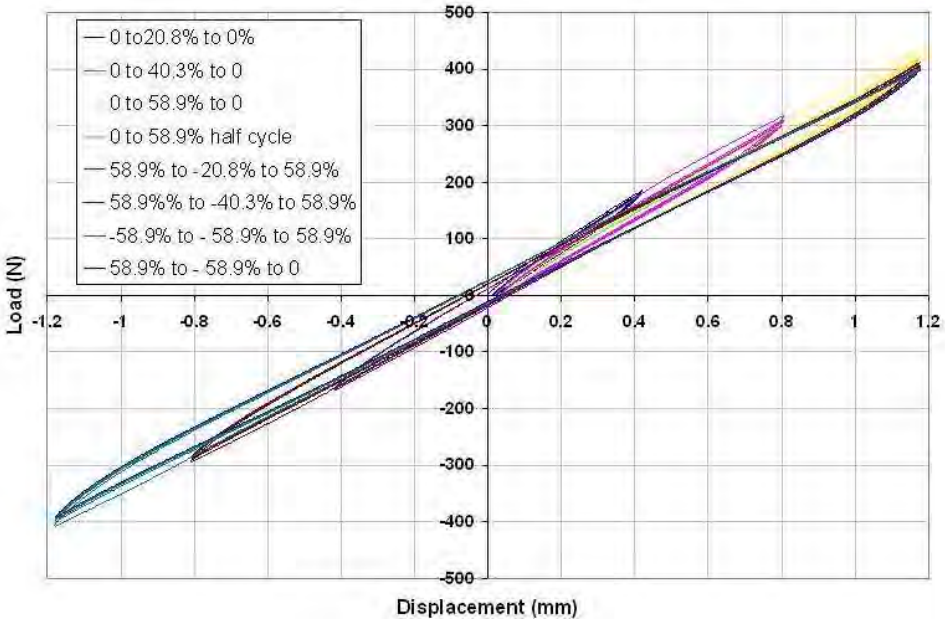

Figure A.7.7: N1 P Double shear sandwich

Appendix 8 – Fitting material models to experimental data in MSC MARC

Material models were fitted to uniaxial and equi-biaxial experimental stress strain data using FEA code MSC MARC. The experimental data was obtained as described in Chapter 3 where sets of data to equivalent values of I_1 were used. Figures A.8.1 to A.8.3 show examples of the different material models used in the research as well as an example of an unstable fitting shown in Figure A.8.4. This is an example of a worst case scenario when fitting in any FEA software package and shows that it is necessary to extrapolate for the C_{ij} coefficients obtained to make sure that they are valid. It is also prudent to to apply the Plausibility Theory developed by Johannknecht et al **[49] [50]** as described in Section 3.91.

Figure A.8.1: Neo Hookean material model

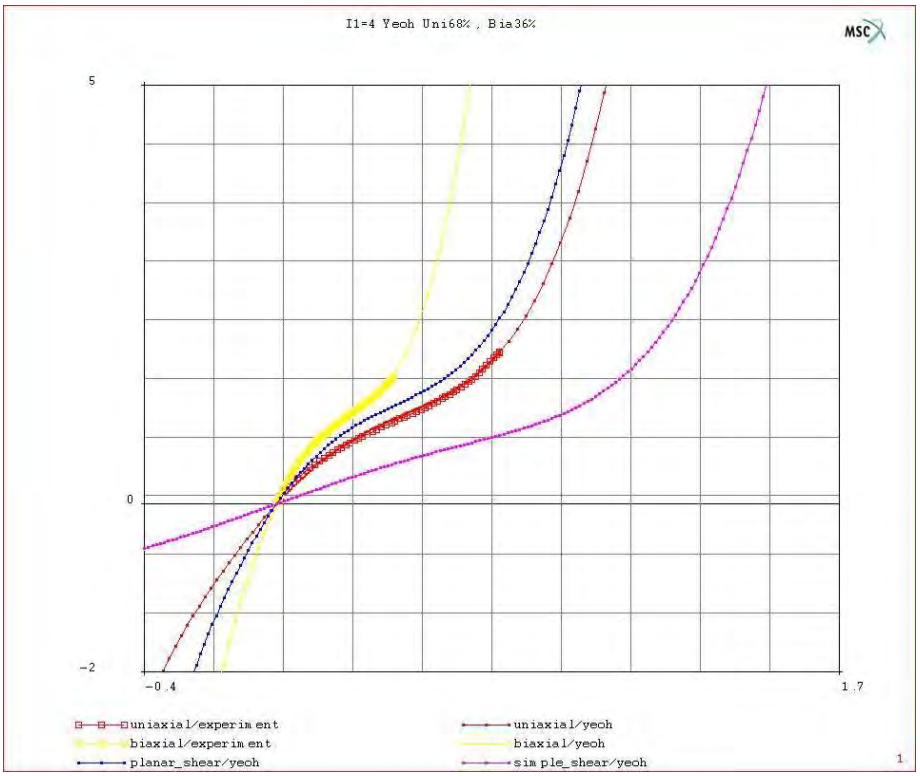

Figure A.8.2: Fitting using Yeoh material model

Figure A.8.3: Fitting using third order deformation model

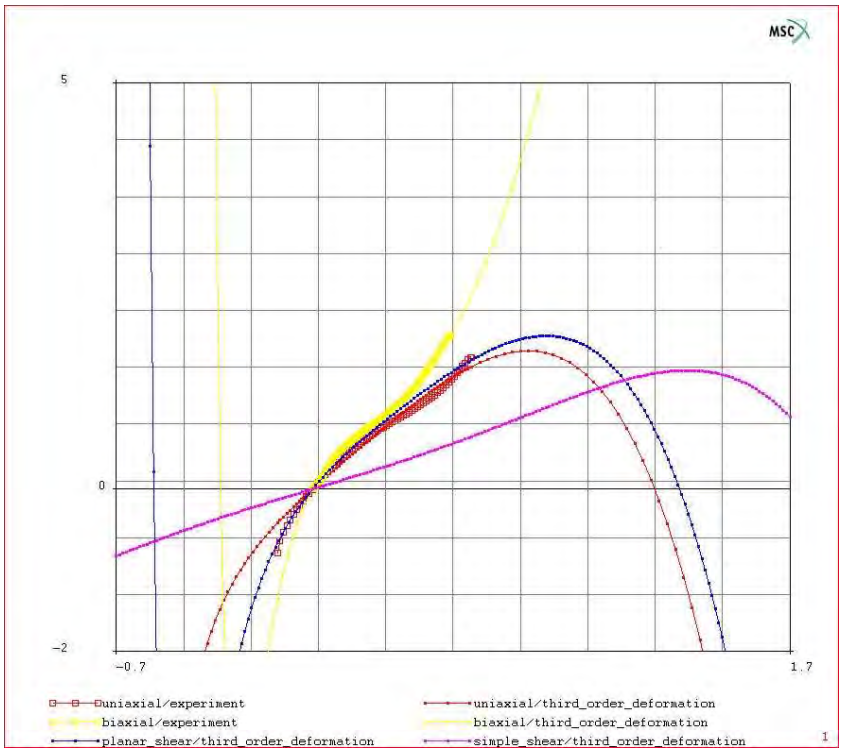

Figure A.8.4: Unstable coefficients using the third order deformation model